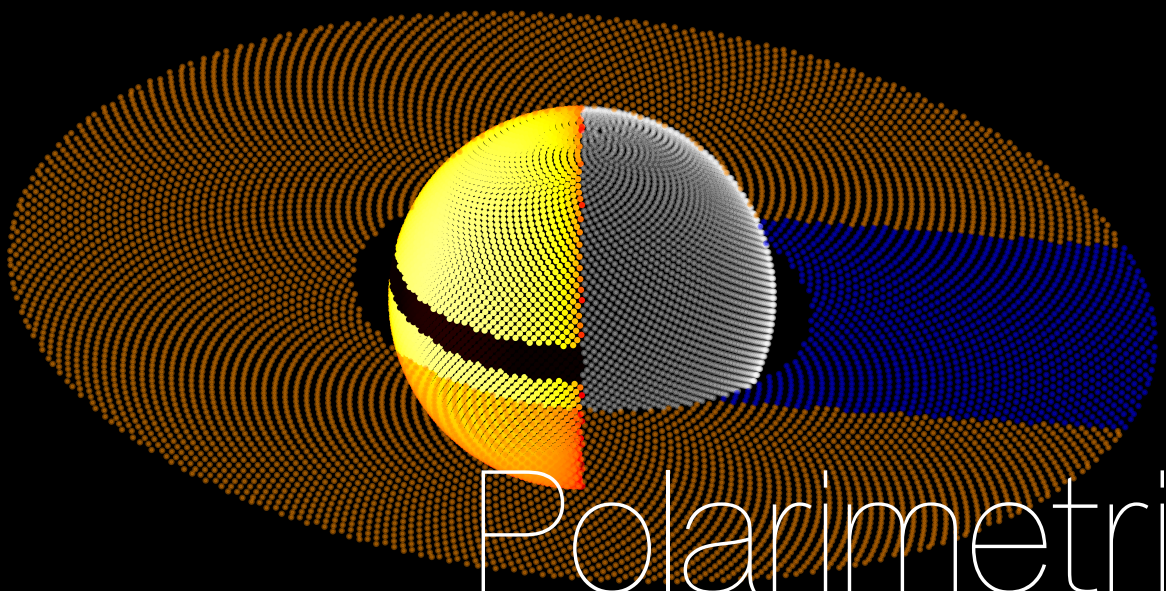

Polarimetric modeling of non-transiting and transiting exorings

A. K. Veenstra

Technische Universiteit Delft

TU Delft

Polarimetric modeling of non-transiting and transiting exorings

MSc Thesis Report

by

Allard Veenstra

to obtain the degree of Master of Science,
at the Delft University of Technology,
to be defended publicly on Thursday, April 20, 2023 at 14:15

Student number: 5405629

Printed: April 11, 2023

Thesis committee:

Dr. W. Wal	TU Delft, Committee Chair
Dr. D. M. Stam	TU Delft, Daily supervisor
Dr. M. A. Kenworthy	TU Delft, committee
Dr. P. Visser	TU Delft, committee

TU Delft Delft University of Technology

Preface and Acknowledgements

Three years ago, I decided to stop with my Applied Physics master at the TU Eindhoven and instead enrolled at the TU Delft to pursue a master's in Aerospace engineering. I made the switch to pursue my research interests which included the field of exoplanets. During these past years I have learned a lot and due to my internship and my thesis work I know for certain that I made the right decision to switch masters. As a fitting conclusion to my master I am happy to present a novel study on ringed exoplanets.

I want to express my gratitude to Daphne Stam for giving me the opportunity to work on such a cutting-edge research topic, and for her supervision and feedback during this past year. I would also like to thank Matthew Kenworthy for his guidance and for sharing unpublished observational data with me; Jorge Zuluaga for allowing me to work on the development of the Pryngles package. Finally, I am especially grateful to my girlfriend and family, who have supported me during the difficult parts of my master's.

A. K. Veenstra
Delft, April 2023

Contents

Abstract

Planetary rings seem to be a common appearance around large planets because every large planet in the solar system has them. They have, however, not yet definitively been detected around exoplanets. Because the formation of rings might be closely related to planetary formation, as well as the formation of moons, much could be learned from discovering rings around exoplanets. To aid in this search, we developed a radiative transfer model that includes all orders of scattering and polarization and can calculate the reflected and transmitted light for any planetary orbit and ring geometry. Previous studies have analyzed the effect that rings have on a transit as well as on the reflected light but those studies have not included the polarization of light. Using the developed model, the effect that rings have on the reflected flux, polarized flux, and the degree of polarization was characterized by varying the orbit orientation, ring orientation, ring size, the optical thickness of a ring, and the ring particle properties. Our study showed that rings introduce unique features in both the flux and degree of polarization curves. Especially the existence of ring-plane crossings, when the ring is illuminated from the side, causes distinct features in the light curves. Adding polarimetric capabilities to the next generation of telescopes could help with determining the presence of rings due to the different scattering behavior of the ring and planet.

The developed model allows for a fast and easy generation of accurate light curves which allowed for two additional studies to be done. These were a bit smaller in scope and the first involved fitting the transit of a planet with a potential ring. The result of the fit and subsequent analysis is that there is likely no ring. However, because the model was not initially designed to deal with the close proximity of the planet to its star no definitive conclusion can be drawn. In the second study, the reflected flux and polarization of the transiting planet J1407b, which is suspected to have a large circumplanetary disk, were computed to assess the detectability. These generated light curves and values were then compared to unpublished observations made with the SPHERE/ZIMPOL instrument that detected no signal. The computed flux and degree of polarization lie well below the detection limit and are thus in agreement with the SPHERE/ZIMPOL observations.

1 Introduction

The formation and evolution of planetary systems is an important topic in astronomy but for a long time there was only one system that could be observed and studied: our own. Having only one data point was not a problem for a long time since little was still known about the planets in the solar system. It became a problem when advancements in computing power, paired with better observations, have allowed for simulations that attempt to accurately model the formation of the planets in the solar system. These models are often plagued by uncertainty in the starting values and the stochastic nature of planet accretion [1]. Currently, there are multiple possible theories on the formation of planets making it an active field of study [2]. Discovering other planetary systems could give clues on the most likely theories. This has been happening ever since the first detection of another planetary system by Wolszczan and Frail [3] in 1992. The system they found contained at least three exoplanets around a pulsar, thus very different from our own solar system. Not long after however, the discovery of the first exoplanet around a solar-type star by Mayor and Queloz [4] in 1995 truly led the way to exoplanet research. Since then, the number of discovered exoplanets has increased rapidly. As of March 2023, there are 5336 confirmed exoplanets and another 2717 candidate planets [a].

The increase is partly due to space telescopes such as NASA's TESS (Transiting Exoplanet Survey Satellite) and the Kepler space telescope. These missions were, and TESS still is, dedicated to finding exoplanets around nearby stars and future space telescopes like ESA's PLATO (PLAnetary Transits and Oscillations of stars) will continue the search. Ground-based telescopes have also improved considerably since those initial exoplanet discoveries. They were initially only used to detect exoplanets using the radial velocity technique, which is the technique used in the detection made by Mayor and Queloz [4], but new instruments like ZIMPOL (Zurich Imaging POLarimeter) that is part of the SPHERE (Spectro-Polarimetric High-contrast Exoplanet Research) system on the VLT (Very Large Telescope) [5] and GPI (Gemini Planet Finder) on the Gemini South telescope [6] represent a new generation of instruments aimed at directly detecting exoplanets. They incorporate technologies like adaptive optics and coronographs making it possible to directly observe large gaseous planets in the near-infrared, as long as they are sufficiently separated from their host star. Direct detection is hard because of the large difference in brightness, where the signal of the planet is easily lost in the glare of the star [7]. The first direct detection of a system containing large planets happened in 2008. Using the Keck and Gemini telescopes Marois et al. [8] discovered a system containing three hot and very large planets ($5 - 13\ M_{\mathrm{Jup}}$), so massive that some of them are on the edge of what is still called a planet. The first direct detections of Jovian-type planets using GPI and SPHERE were reported by Macintosh et al. [9] and Wagner et al. [10] respectively, again finding hot giant planets. The high sensitivity that these new instruments have might also allow for the detection of rings around exoplanets.

To aid in discerning the reflected light from the stellar glare, GPI and SPHERE have polarimetric capabilities. Polarimetry can help because reflected light is polarised while direct starlight is not [11]. Due to this, polarimetry has become more popular, with the proposed thirty-meter telescope (TMT) featuring an instrument called PSI (Planetary Systems Imager) which will also be capable of doing polarimetry [12].

This work will be about analyzing how the presence of rings around an exoplanet influences the flux and degree of polarization of the reflected and transmitted starlight. Both rings like those around Saturn as well as circumplanetary disks, very large rings that are created during planet formation, will be investigated. For clarity, since both structures are technically rings, when rings are mentioned this means Saturn-like rings. Circumplanetary disks will be called as such.

The next sections in this introduction will now be laid out. First, some background information on rings is given followed by explaining why they should be studied in Sect. 1.1. Then in Sect. 1.2, the same

[a] http://exoplanet.eu/catalog/

is done for circumplanetary disks. In Sect. 1.3, there is a short overview of the history and methods to discover extra-solar rings and disks. Followed by a summary of what has been discovered and potential candidates. Section 1.4 is about the importance of polarimetry which is followed by the current body of work in Sect. 1.5. The problem statement and research questions are posed in Sect. 1.6, and in Sect. 1.7, finally, the outline of this thesis is presented.

1.1. Why study extra-solar rings?

Rings, as found around the giant planets in the solar system, are annular features usually composed of a mixture of a large number of small bodies and smaller particles, unable to aggregate because of their proximity to the planet or to moons. Their maximum stable radial extent is governed by the Roche limit, which depends on the density of the planet, the density of the orbiting body/particle, and the radius of said body/particle [2]. For a fully deformable body/particle, the Roche limit is defined as [13]

$$R_{\text{roche}} = 2.45 R_p \left(\frac{\rho_p}{\rho_b} \right)^{1/3}, \tag{1.1}$$

where R_p is the radius of the planet, ρ_p the density of the planet and ρ_b the density of the orbiting body.

All gas giants in the solar system have rings. Those of Saturn are the most recognizable and visible and were observed by Galileo around 1620 but first described by Christiaan Huygens in 1659. The rings around the other three large planets in the solar system (Jupiter, Uranus, and Neptune) were discovered much later as they are much narrower and fainter. The remarkable thing is that the rings around the four planets are different. They vary wildly in composition, particle size, radial extent, optical depth, and albedo [2, 14]. So while every large planet in the solar system has rings, suggesting they are almost guaranteed to form around giant planets and thus possibly by a process tied to planetary formation, every ring is different, suggesting different, stochastic formation processes that are not necessarily tied to the planet's formation. Observing rings around exoplanets could indicate the most likely formation processes using statistics. Saturn-like rings will be used in this work since they are the brightest and largest. Even though they have not yet been discovered around exoplanets such rings would be the easiest to actually observe around exoplanets [15]. Some of the fields of research that could advance by discovering extra-solar rings are given below.

1.1.1. Formation of rings

The formation of rings is still shrouded in uncertainty. As mentioned before, all the giant planets in the solar system have rings yet they are all different. The three main theories on the formation of rings are that rings are either remnants of the circumplanetary disk, remnants of moons that ventured into the Roche-limit, or remnants of captured comets [2]. If the first theory is correct, rings only have one chance of forming rings while the latter two theories suggest it can happen multiple times and long after the planet's formation. It is of course also possible that all three theories are correct. Discovering more rings, especially around younger planets could say something about the formation process. For example, finding young planets with rings as well as moons would be a strong proponent for the theory that rings can be remnants of the circumplanetary disk [14].

1.1.2. Lifetime of rings

The lifetime of rings, especially those of Saturn, is a debated topic. Simulations of the development of moons around giant planets are inconclusive in showing the age of the rings [16]. While data from the Cassini mission and some simulations are leaning toward the rings around Saturn [17] being relatively young, the data is far from conclusive and there are enough studies that argue that the rings are older [18, 19]. Especially the link between the current composition, an ice fraction of roughly 90% [20], of the rings and the potential sources and sinks of material, the ice fraction of the nearby moons is around 60% [21], is problematic for the determination of the age of the rings [19].

Coupling the formation and the lifetime of rings to observations, a few things could be said. If rings are remnants of circumplanetary disks, this would suggest they can be stable over very long time-scales, which could explain the rings around Saturn [16, 18, 19, 22]. Finding that rings are common could support this theory but could also mean that the formation of rings happens frequently while rings

still decay relatively rapidly. Finding very few rings would in turn most likely mean that rings are not stable over longer time periods and/or their formation does not happen frequently.

When observing rings, their age could be inferred from the age of the system, if the system is young enough, but also from the composition of the rings. Micrometer-sized dust, for example, is removed quite quickly from rings that are not optically thick enough [2]. Rings containing a lot of dust are thus either young or have a mechanism for replenishing that dust, something that is observed for some parts of the rings around Saturn. Because particle size is one of the parameters that influence the polarization of reflected light, polarimetry could potentially infer the particle size remotely.

1.1.3. Extracting planetary features

An interesting remark is made by Schlichting and Chang [23] on ringed planets that orbit close to their star. The obliqueness of rings around a planet depends on competing effects of the planet's oblateness, characterized by the quadrupole moment J_2 and the tidal effects of the star [24]. If J_2 is not strong enough to ”win” from the tidal effects, the ring will be warped and forced to be parallel to the orbital plane of the planet instead of in the planet's equatorial plane. The orientation of the ring can thus put an upper bound on the value of J_2 which can say things about the planet's interior. Discovering rings could thus also, incidentally improve the knowledge of the planet that harbors them.

1.2. Why study circumplanetary disks?

A circumplanetary disk is fundamentally different from rings found in the solar system since it is a temporary structure, formed during the formation of planets [2]. To put the formation in context, a quick and very abbreviated rundown on how a star system and gas giants form now follows. After a molecular cloud, a cold and relatively dense region in the interstellar medium, collapses due to some destabilizing event, a star can form at the center. Not all the material will fall into the star and the material that orbits the newly formed star forms a circumstellar disk, also called a protoplanetary disk. The leading theory on planet formation, called core accretion theory, then predicts that the dust and gas contained in the disk will slowly aggregate to eventually form planetesimals. Planetesimals that are heavy enough will also accumulate gas, causing a runaway gas accretion which will lead to the formation of large planets like Saturn. During the formation of the planet, a disk of material surrounds it, which is called the circumplanetary disk [2, 25, 26].

The material in a circumplanetary disk is not static and will either aggregate to form moons, get thrown back into the circumstellar disk, or fall into the young planet. The exact process by which either of these happens is not clear and there are multiple theories. Two popular ones are the minimum mass model, first proposed by Lunine and Stevenson [27], and the gas-starved model, first proposed by Canup and Ward [28, 29]. In the minimum mass model, all the mass that was present in the circumplanetary disk ends up in the formed satellite system, requiring heavy disks. Moon formation thus only starts after there is no more inflow of gas and dust from the protoplanetary disk. Miguel and Ida [30] applied the minimum mass model to try to explain the formation of the Galilean moons around Jupiter. They showed that in this model the system was unlikely to form because of fast accretion and migration of solids preventing the formation of large satellites. This of course does not necessarily discredit this theory for all planetary systems.

In the gas-starved model the circumplanetary disk is continuously fed gas and dust through a meridional circulation [31] from just above the mid-plane of the protoplanetary disk [16]. Due to this slow trickle of material, there is a continual generation of satellites at the outer edge of the circumplanetary disk that then migrate inward due to satellite-disk interactions [28]. This quasi-steady state, where satellites are formed semi-regularly while previously formed satellites fall into the planet allows for a lower mass disk. Both Batygin and Morbidelli [16] and Cilibrasi et al. [32] show that the Galilean system is a likely outcome in this model.

A less popular model by Crida and Charnoz [33, 34] is mentioned here because of the implications to observations and an interesting link between circumplanetary disks and ordinary rings. The model could be seen as an extension of the minimum mass model and suggests that regular satellites around giant planets, especially Saturn, formed from the material coming from massive rings. The big difference with the minimum mass model is that the initial ring lies within the Roche limit and then migrates outward to

form the satellites. If this were to be the case, these rings would again have to be as massive as the formed satellites combined. For comparison, Saturn's rings, which are the heaviest in the solar system, have an estimated mass of only 1.7% the mass of Rhea, the largest satellite of Saturn proposed to be formed in this way [2, 33]. These initial rings would thus have to be much more optically thick than Saturn's. Discovering very heavy, and thus likely very opaque rings extending only out to the Roche limit around relatively young planets could thus lend credibility to this theory.

Detecting rings can also lead to the indirect detection of extra-solar moons. Gaps in the rings can be explained by the presence of shepherd moons, as suggested by Kenworthy and Mamajek [35].

1.2.1. Potential properties

Since circumplanetary disks have already been observed both directly [36] and indirectly [37], it is a good check if the ring formation theories mentioned above can be put into context. Before these and other discoveries are tested to the theory in Sect. 1.3, it is good to first see what the theories on their own would say about a circumplanetary disk and what the differences are between the models.

Starting with the gas density inside the disk, there is an immediate difference between the minimum mass model and the gas-starved model. As the name suggests the gas-starved model assumes a much lower gas density compared to the minimum mass model [30, 32].

The differences in disk lifetime are less obvious since the lifetime varies wildly for the minimum mass model, between 10^4 and 10^7 years according to [30], where the disk lifetime is counted from the moment moon formation "begins", which is when gas infall from the protoplanetary disk stops. Whether this is also when the circumstellar disk dissipates is not mentioned by Miguel and Ida [30] so coupling this to the lifetime of the system is difficult. The lifetime of the disk in the gas-starved model is tied to the lifetime of the circumstellar disk which follows an exponential decay with a characteristic time of 2.5×10^6 yr [38]. This allows it to couple the age of the system, which is measured from the age of the star, to the age of the disk and its remaining lifetime. The formation of moons is assumed to continue until there is no more mass inside the circumplanetary disk, so it continues after the dissipation of the circumstellar disk [28]. A period should thus exist where there is still a circumplanetary disk but no more circumstellar disk. This would improve the odds of discovering the circumplanetary disk in transit or with direct detection methods due to a larger contrast with its surroundings. For planets orbiting at large distances from the star, at 25 AU for example, the lifetime of a circumplanetary disk, after the dissipation of the circumstellar disk, is estimated by Mamajek et al. [37] to be on the order of 10^7 yr.

Particle sizes inside the circumplanetary disk vary from model to model. Due to their fast accretion in the minimum mass model, the smaller particles quickly disappear, often within 100 yr [30]. In the gas-starvation model, there is a constant influx of gas and dust so besides the satellites, the particle size and amount of dust remain constant [39]. Particle sizes of 0.1 mm are often assumed with surface densities of 100 g/cm^2 [16, 39].

In both models, the circumplanetary disk extends up to a significant portion of the Hill radius $0.1 - 0.3\ R_{\mathrm{hill}}$. In the gas-starved model, it is hypothesized that there is a sharp boundary of particles after $85\ R_p$, with R_p the radius of the planet, due to streaming instability causing the rapid formation of satellite seeds at that point in the disk [32, 39]. Streaming instability is a proposed mechanism of rapid dust density increase due to drag, however, a full explanation is beyond the scope of this introduction. Regardless of the model, a circumplanetary disk is expected to be significantly larger than the rings found in the solar system.

1.3. Discovering rings around exoplanets

Compared to their host stars, exoplanets are extremely faint. Their close proximity to their star, on the order of astronomical units (AU), paired with their large distance to us, on the order of light-years, also means a very high angular resolution is needed to observe them directly. Direct detection, where the reflected light or thermally emitted radiation of an exoplanet is observed directly has only relatively recently been possible, see Fig. 1.1, but is slowly becoming a more used method for discovering exoplanets now that is clear that most stars have planets.

Other methods of detecting exoplanets have been much more prominent and over the years multiple

methods have been developed. These methods do not attempt to directly observe the planet but instead look at the effect an exoplanet has on the observed starlight. In Fig. 1.1 the different techniques and the number of exoplanets discovered with them are shown. Of the four most popular methods displayed in the plot, only transits, and imaging will allow for the detection of rings. In this section, some campaigns to discover rings around exoplanets using the transit method will first be laid out. This is followed by a few words on direct detection. Finally, the last two sections will be about the circumplanetary disks and rings that have been found or are candidates.

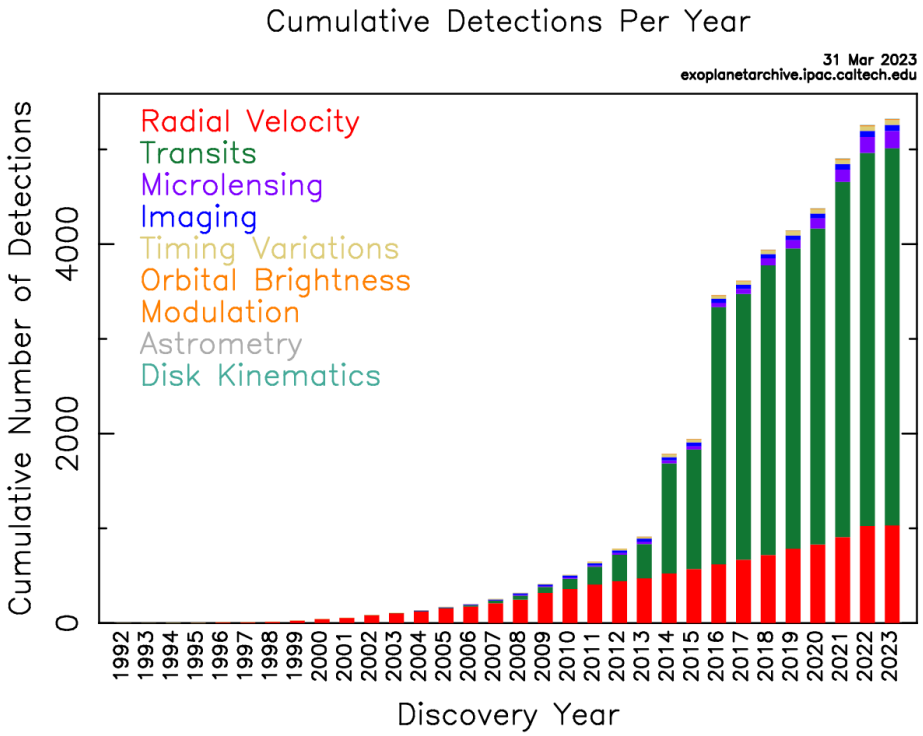

Figure 1.1: The cumulative number of discovered exoplanets grouped by their method of detection, it should be noted that not all listed methods are visible. https://exoplanetarchive.ipac.caltech.edu/

1.3.1. Transit

The transit method is a well-known method of discovering exoplanets. It is based on the (partial) eclipse that happens when a planet orbits in front of the star with respect to us. The method limits detection to planets with an approximately edge-on orbit but can inform us about some properties of the planet [2]. There have been multiple efforts to find extra-solar rings from transit data. Heising et al. [40] looked at 21 exoplanets discovered by Kepler but found no convincing evidence of rings. A similar study was done by Aizawa et al. [41], who developed a methodology and applied it to 163 planets discovered by Kepler [42]. Again no convincing evidence of rings was found.

1.3.2. Direct detection

Direct detection of exoplanets is difficult due to the large difference in intensity between the light emitted by the star and the reflected or emitted light from the planet. In order for the planet to be spatially resolved its distance to the star also needs to be sufficiently large, even with a high angular resolution. A few techniques have been developed that aid in the direct detection of planets: a coronograph is used to block the light from the star but allows surrounding light to pass [43], extreme adaptive optics corrects the wave-front errors due to Earth's atmosphere [44] and helps the coronograph perform better, angular differential imaging [45] which reduces stochastic noise and polarimetric differential imaging [46]. Despite the difficulties, direct imaging of exoplanets can provide several benefits compared to the other methods. For example, using the combination of spectrometry and polarimetry, it is possible to characterize the composition of atmospheres, the temperature of the planet, and/or the size of dust grains surrounding the planet.

Even though it is expected that almost every star has planets [2], most direct detections of planets

were done for stars where it was already known that there were planets since searching for exoplanets by directly observing is a time-intensive method of finding exoplanets. This is reflected in Fig. 1.1.

1.3.3. Found circumplanetary disks

Candidate circumplanetary disks have been either discovered from transit light curves or direct detection. Below we provide a short overview of the current knowledge. The candidate circumplanetary disks discovered in transit light curves are often characterized by unusual behavior (more on that next), while the ones that are discovered by direct detection fall neatly into the theory of circumplanetary disk formation and are confirmed observations of circumplanetary disks.

Examples of unusual transit light curves attributed to a planet surrounded by a circumplanetary disk are: J1407b [35, 37], EPIC 204376071 [47] and V928 Tau [48]. Of these three examples, J1407b is the most well-known. The culprit behind the unusual eclipse of the star is attributed to a young planet with a circumplanetary disk. The transit that led to its discovery lasted for roughly 54 days and has only been observed once. The photometry for the discovery comes from the SuperWASP (Super Wide Angle Search for Planets) database [49] [50]. Later studies constrained the likely mass and eccentricity of the planetary ring system to be between $20 - 100$ $\mathrm{M_{Jup}}$ [51] and $e > 0.7$ [52], respectively. Direct observations with ALMA (Atacama Large Millimeter/submillimeter Array) did not detect anything at the place where the ring system was expected to be but did observe something at a location that could be consistent with an unbound object that moved in front of the star at the time of the stellar eclipse [53]. Based on these observations there are two principle options: The source they found is not the ring system but rather some other phenomena, like a background galaxy, which makes the observation an upper bound on the ring system in terms of brightness. Or, the source they found indeed caused the unusual transit light curve, which would most likely make it an unbound object. In Sect. 4.2, I revisit the J1407 system using new simulations and data from an unpublished article that favors the first option.

Due to the indirect nature of inferring what caused a transit light curve, circumplanetary disks discovered from transit have not yet been confirmed. There are however, two confirmed circumplanetary disks. Both of the disks have been detected using direct detection and are found in the same system around a star that was already known to have a protoplanetary disk with gaps. The two objects, named PDS70b [54] and PDS70c [55], show a circumplanetary disk in an earlier stage than J1407b does. In a follow-up study by Benisty et al. [56] it was also shown that PDS70c nicely follows the gas-starved model of circumplanetary disk development. This is another contrast with J1407, which falls a bit outside the theory's predictions due to its age and lack of circumstellar disk.

1.3.4. Potential rings or disks

While there are currently no confirmed observations of exoplanets with rings there are some candidate planets. These candidates mostly fall into a group of planets called "super-puffs" [57]. This group of planets appears to have a very low density, $\rho_p \leq 0.3$ g cm^{-3} ([57] and references therein). These planets often orbit close to their star which can lead to expanded(puffed up) atmospheres and therefore lower densities[58]. However, another possible explanation is that the radius of the planet is overestimated, driving the density down. The radius of the planet is estimated using the depth of the transit [2]. The existence of a sufficiently opaque ring would drop the depth of the transit light curve which in turn would increase the inferred area. Since the radius of the planet is estimated using the area, this would overestimate the radius

$$R_{\mathrm{inf.}} = (A_{\mathrm{inf.}}/\pi)^{1/2} \geq R_p \ , \tag{1.2}$$

with $R_{\mathrm{inf.}}$ the inferred radius of the planet and $A_{\mathrm{inf.}}$ the inferred area of the planet. A recent analysis by Piro and Vissapragada [57] found that rings are a plausible explanation for at least three of the ten super-puffs used in the study and with small adjustments to their assumptions for another three. However, to properly confirm the presence of rings, the sensitivity of the observations would need to increase to roughly $10 - 50$ ppm. According to the study, the most interesting ringed planet candidate is the recently discovered HIP 41378f [59]. This planet differs from the other super-puffs by orbiting further out, at 1.37 AU compared to 0.1-0.7 AU. The plausibility of rings explaining the low density was confirmed in studies by Akinsanmi et al. [60] and Alam et al. [61]. The study by Akinsanmi et al. [60] showed that a planet with a ring was as probable in explaining the transit light curve as a planet with

no ring when only considering the fit of the light curve. Other characteristics of the planet, however, such as the absence of a clear, low-metallicity atmosphere, make an expanded atmosphere less likely. That the atmosphere could not be a clear, low-metallicity atmosphere was shown by Alam et al. [61], who used transmission observations made in the near infrared (NIR).

The proximity of these super-puffs to their star places constraints on the properties that such rings could have. The particle composition cannot be icy due to the higher temperatures closer to the star. The particles around those super-puffs can therefore only be made of more refractory materials [2]. The composition determines the particle's albedo which in turn is one of the determining factors of the visibility. Rings around super-puffs are therefore expected to be less visible than the ones around Saturn for example. Their proximity to their star also affects the stability of any potential ring as was already touched upon in Sect. 1.1.3.

Candidates outside of the super-puff group often have features in their transit light curve that could be caused by the presence of a ring. As was shown by Barnes and Fortney [14], the presence of a ring can make the ingress and egress of a transit curve consist of multiple steps as more of the ring is eclipsing the star. It can also cause increases in flux just before and after the ingress and egress respectively, due to forward scattering. An example of a candidate system, which will be expanded upon in Sect. A.1, is AU Microscopii b. The ingress and egress of its transit light curve have unusual features but according to the analysis in Sect. A.1, this is most likely caused by stellar activity.

1.4. The importance of polarimetry

Polarimetry as a tool to detect exoplanets has become available with the development of the aforementioned instruments for VLT and Gemini but has already a long history in planetary science. A famous example is the characterization of the cloud particles in Venus' atmosphere by Hansen and Hovenier [62]. Using the disk-integrated light from Venus, so no spatial resolution across the planetary disk, they were able to characterize the shape, size, and size distribution of the particles in the cloud or haze layer around Venus, and the altitude of said layer. Using this information on the particles, they were able to confirm their composition to be mostly sulfuric acid. Due to the difficulties in direct imaging, exoplanets will consist of single pixel signals, thus also disk integrated, for the foreseeable future.

Using polarimetry has some key advantages when discerning light reflected off a planet from the light of the star. Light from a solar-type star can be assumed to be unpolarized [11], while light that has been scattered by the atmosphere of a planet and/or the particles in the ring is often linearly polarized. The degree of polarization varies with the phase angle of the planet but also the particles and/or molecules in the atmosphere of said planet. Depending on the composition of the planet/atmosphere, at the phase angles where the planet is most easily discerned from the star (around 90°) the polarization is high enough to be detectable [7]. Because the scattered light of dust in a circumstellar disk can dominate the signal from a circumplanetary disk or planet, polarimetry is best suited for use on older systems where stellar companions orbit in a largely dust-free environment.

The use of polarimetry is not limited to cases where the light reflected by the planet is spatially resolved from the star. Since the starlight is unpolarized, any degree of polarization can be attributed to come from reflected light. Due to the intensity difference, however, the degree of polarization is expected to be very small (10^{-5}) [63].

Even though using the polarization of reflected light is a well-known technique it is a relatively new method of detecting and characterizing exoplanets. There has been a body of work investigating the polarization signal exoplanets. Modeling the polarized light reflected by Earth-like exoplanets has been done by Stam [64]. This work has been expanded multiple times by adding more planetary features. Some examples of this are: Zugger et al. [65] showed the effect oceans have on the signal, Karalidi et al. [66] demonstrated the effect of clouds and Berdyugina et al. [67] suggested using polarization to detect biomarkers. Reflected light signatures of giant extrasolar planets, like Jupiter, have also been studied extensively. Seager et al. [63] showed the signal of close-in giant planets and showed that the signal was highly dependent on condensates in the atmosphere. Stam et al. [7] and Buenzli and Schmid [68] characterized the effect of different atmospheres for Jupiter-like exoplanets as a function of the phase angle. An analytical framework is presented by Madhusudhan and Burrows [69]. Inhomogeneous atmospheres on Jupiter-sized exoplanets are presented in Karalidi et al. [70]. A more recent study

computes the needed accuracy of future instruments to be able to assess the sulfuric acid concentration in cloudy exoplanetary atmospheres [71]. Their study focussed on planets thought to be in the habitable zone of their star and they show that polarimetric capabilities are essential in the determination of the acid concentration. Polarization signals during transit have also been investigated [72] [73]. The above articles are examples of what has been done in this field so far.

1.5. Current body of work

There is already a body of work done on ringed exoplanets despite the fact that a ringed exoplanet is yet to be found. There have been multiple studies on what the signal from a ringed exoplanet would look like. Barnes and Fortney [14] modeled the transit of ring systems of giant extrasolar planets. They found that the transit of a ringed planet would only be discerned from a larger, non-ringed planet during the ingress and egress of the transit, limiting the detection to high-resolution instruments, both photometric as well as temporal. Work done on the reflected light from planets with rings of different sizes, assuming planets on circular orbits with isotropically scattering (Lambertian) surfaces and rings with isotropically scattering particles by Arnold and Schneider [74]. Improved upon by Dyudina et al. [15] by implementing the anisotropic scattering of Jupiter, Saturn, and Saturn's rings, which is a more realistic behavior. They also modeled the effect of eccentric orbits. Another study showed that the variability in the flux of light perceived to be coming from a stable star due to the reflected light coming from the planet and ring might be large enough to be detectable [75], removing the need to directly image and spatially resolve the planet. A recent paper by Zuluaga et al. [76] describes a Python package they developed called `Pryngles` with which the total flux curve of ringed planets can easily be computed for any desired system geometry. In their paper, they only model a Lambertian reflecting planet and ring but this could be expanded upon with more sophisticated methods of scattering light which has been done in this study. Work has also been done on the transmission of light through circumplanetary disks, see for example Ohno and Fortney [77].

An important thing to note about the studies above is that they do not include the polarization of light. As shown in Sect. 1.4, polarimetry can provide unique information on the planet and its rings. The usefulness of polarimetry has also been demonstrated in an article by Stolker et al. [54] where the effect of rings around a self-luminous giant planet is modeled. They showed that a planet with cold Saturn-like rings around it produces a significant and detectable amount of linear polarization, $1 \pm 0.05\%$ depending on the orientation and oblateness of the planet. However, the properties of the rings or the system geometry were not varied much. A very recent paper, not yet published as of writing, by Lietzow and Wolf [78] does vary the properties of the rings and also includes the polarized flux signal. Using a Monte Carlo simulation to model the reflected light they vary the ring's size and orientation, the ring particle's size and composition, and lastly the wavelength at which the behavior is simulated. They do, however, use Mie-theory to describe the scattering of the ring particles which has some inaccuracies because the particles are assumed to be perfect spheres and only use an edge-on orbit. Despite the similarity between this thesis work and the paper by Lietzow and Wolf [78] the work presented here is still unique. Modeling the reflected light coming from a planet with a ring including polarization effects for various: orbital geometries, ring sizes, ring optical thicknesses, ring particle properties (using realistic scattering matrices), and ring orientations has not been done before.

1.6. Research framework

The aim of this study is two-fold. First, to investigate the flux and polarization curves of light reflected off an exoplanet with a dusty ring imaged as an unresolved source of light as a function of the properties and orientations of the ring and orbit geometry by modeling the transmission and reflection of light. Second, to find the flux and degree of polarization curves of an exoplanet with a dusty, cold circumplanetary disk imaged as an unresolved source of light, that has properties obtained from fitting to an observed transit light curve.

1.6.1. Research questions

To help answer the research goal three research questions are introduced, each with sub-questions. The first research question pertains to the general work that needs to be done for both research goals. Both goals are described in the subsequent research questions.

RQ1 – What determines the flux and degree of polarization curves of an exoplanet with an unresolved dusty ring for various orbit and ring orientations as well as ring sizes and dust properties?

- **RQ1.1 –** How does the reflection of light, including the physics behind polarization, work?
- **RQ1.2 –** What are good algorithms to model the scattering of light with?
- **RQ1.3 –** What are the scattering properties of a ringed planet?
- **RQ1.4 –** How to model all the possible orbit and ring orientations?

RQ2 – What do the flux and degree of polarization curves look like as a function of the true anomaly?

- **RQ2.1 –** What is the effect of different orbit and ring orientations on the flux and degree of polarization curves?
- **RQ2.2 –** What is the effect of different ring properties on the flux and degree of polarization curves?
- **RQ2.3 –** What are the characteristics of the flux and degree of polarization curves obtained that could lead to the detection of dusty rings?

RQ3 – Can a transit fit predict the flux and degree of polarization curves along the rest of the orbit?

- **RQ3.1 –** Which discovered ring or circumplanetary disk has a transit curve that is well suited to be fit using the developed model?
- **RQ3.2 –** What is the effect of forward scattering on the generated transit curve?
- **RQ3.3 –** How many parameters of the circumplanetary disk are constrained by the fit?
- **RQ3.4 –** Are the possible degree of polarization curves constrained enough to converge to a most likely curve?

Research Objectives

The main objective, as stated previously, can be divided into sub-objectives that define the path the research takes to answer the research questions.

OB1 – Model the light reflected by a planet with a simple atmosphere.

OB2 – Model the particulate reflection and transmission of dusty rings.

OB3 – Generate flux and degree of polarization curves of a planet with a ring orbiting a star for different ring orientations and properties.

OB4 – Analyse the flux and polarization curves for a planet with a ring orbiting a star and assess the dependency of the curves on the properties of the ring and the orientation of the orbit.

OB5 – Model the transit of a planet, with a simple atmosphere and a ring or circumplanetary disk.

OB6 – Analyse the transit curve and assess the dependency of the transit curve on the properties of the ring or disk.

OB7 – Use the developed code to fit available transit data, or use the properties obtained from a previous fit, to generate possible flux and degree of polarization curves for future observations.

1.7. Outline of this thesis report

This thesis is split into three parts. The first part (Sect. 2) is a paper that contains most of the work and the theory necessary for a correct interpretation of the data, this paper will be submitted to Astronomy & Astrophysics. It is a collaboration with the research group based in Colombia that developed the geometric base of the radiative transfer model that was developed, called `Pryngles`. The radiative transfer part of the model is based on the adding-doubling algorithm. In the paper, the model will be described and its capabilities are explored by doing a characterization of the flux and degree of polarization curves produced by ringed exoplanets. As such it will answer the first and second research questions.

Sect. 3, will be an expansion upon the theory presented in the paper. It will go more in-depth on the fundamentals of light scattering and introduce some new definitions. Some of the terms and theories that were mentioned in the paper, like Rayleigh-scattering or Mie-scattering will be briefly explained.

In the third part, Sect. 4, some of the results that are outside the paper's scope are presented and discussed. The section starts with some validation tests of the planetary atmosphere that were performed for the paper. This is then followed by a study that was born from the flexibility that `Pryngles` poses, allowing for the simulation of many interesting systems with relative ease. To still have a decent analysis of the results, only two planetary systems were checked: the J1407 system and the AU Microscopii system. Only the results of the study of J1407 are presented in Sect. 4, the results of the other study can be found in the Appendix. The planets in both systems orbit such that they transit in front of their star and J1407b, the potential planet around J1407, is also suspected to have a circumplanetary disk. Together these two systems can be considered as an attempt to answer RQ3. The results of these studies are presented as case studies, with their own discussion and conclusion.

2
Paper

Astronomy & Astrophysics manuscript no. output
April 11, 2023

A polarimetric model for transiting and non-transiting exoplanets with rings

Allard. K. Veenstra[1], Jorge I. Zuluaga[2], Jaime A. Alvarado-Montes[3,4], Mario Sucerquia[5,6], and Daphne M. Stam[1]

[1] Faculty of Aerospace Engineering, Technical University Delft, Kluyverweg 2, 2629 HS Delft, The Netherlands
e-mail: a.k.veenstra@student.tudelft.nl

[2] SEAP/FACom, Instituto de Física - FCEN, Universidad de Antioquia, Calle 70 No. 52-21, Medellín, Colombia
e-mail: jorge.zuluaga@udea.edu.co

[3] School of Mathematical and Physical Sciences, Macquarie University, Balaclava Road, North Ryde, NSW 2109, Australia

[4] Research Centre for Astronomy, Astrophysics and Astrophotonics, Macquarie University, Balaclava Road, North Ryde, NSW 2109, Australia
e-mail: jaime-andres.alvarado-montes@hdr.mq.edu.au

[5] Instituto de Física y Astronomía, Facultad de Ciencias, Universidad de Valparaíso, Av. Gran Bretana 1111, 5030 Casilla, Valparaíso, Chile

[6] Núcleo Milenio Formación Planetaria - NPF, Universidad de Valparaíso, Av. Gran Bretaña 1111, Valparaíso, Chile
e-mail: mario.sucerquia@uv.cl

Received 2023; accepted ??

ABSTRACT

Aims. We aim to develop a more robust model to study the complete phase curve of exoplanets as they move along their orbit. In particular, we focus on gas giants that have a ring and investigate the effect that their rings have on the reflected flux and polarization curves as a function of their true anomaly.

Methods. We improve the general photometric model `Pryngles` by basing the radiative transfer calculations on an adding-doubling algorithm that includes all orders of scattering and polarization. Using this improved model, we compute the reflected flux, linearly polarized flux, and degree of polarization curves of a gas giant with a ring as a function of its true anomaly and vary its properties such as the orbit inclination, ring orientation, ring size, the ring particle albedo, and the optical thickness of the ring. The ring will be populated with irregularly shaped particles that

have their optical properties based on measurements. We also demonstrate the usefulness of the model by predicting the reflected flux and polarized flux of the "puffed-up" planet HIP 41378f.

Results. Spatially unresolved dusty rings can increase and decrease the total flux of reflected starlight compared to that of a ring-less planet, depending on the ring properties and the geometries along the planet's orbit. They generally decrease the degree of polarization along the entire orbit. During ring-plane crossings, when the ring is illuminated edge-on, the flux and degree of polarization return close to the value of a ring-less planet which causes sharp changes in the respective curves. In general, ringed planets that orbit edge-on are more difficult to distinguish from ring-less planets based only on their reflected light and degree of polarization. Rings with higher optical thicknesses, brighter particles, and that are larger produce more distinct features and are more easily observable. We also show that if HIP 41378f is indeed surrounded by a ring, its reflected flux compared to the star is on the order of 10^{-9}, and its ring will decrease the degree of polarization in a detectable way.

Conclusions. Using the presented improvements to `Pryngles` we have shown that dusty rings produce distinct features in the flux, polarized flux, and degree of polarization curves, with the most convincing of these features caused by the ring-plane crossings that can produce sharp discontinuities in the degree of polarization curves. The short case study shows, that while HIP 41378f can not yet be directly imaged, the addition of polarimetry to future observations would aid in the characterization of the system.

Key words. Planetary Systems - Planets and satellites: rings - Methods: Numerical - Radiative Transfer - Polarization

1. Introduction

Transit photometry has proven to be a quite successful technique to detect and follow up on exoplanets (see, e.g. Perryman 2018; Deeg & Alonso 2018). Studying the light curve of a star, such as a TESS/Kepler Interest Object (TOI or KOI), can help determine if the star is capable of hosting exoplanets. Additionally, this approach provides valuable insights into the properties of the planets themselves. Transits mostly yield information about planetary architectures, allowing us to constrain the orbits of exoplanets and at least one of their bulk parameters, that is, their size or physical radius (Seager & Mallén-Ornelas 2003). However, to take the biggest advantage of planetary transits, a given observer needs some 'special' types of orbits (i.e. orbits near to edge-on orientations) which allow detecting the drop in stellar flux produced by the combination of observed star, extrasolar planet, and Earth.

Following the success of the transit technique in finding exoplanets, attention began to focus on the geometric aspects of the signal that could reveal additional characteristics of exoplanets. These features include, among others, deviations from the spherical shape of planets (Barnes & Fortney 2003; Akinsanmi et al. 2020a), exomoons (Cabrera & Schneider 2007; Simon et al. 2007; Kipping 2009; Heller et al. 2016), and planetary rings (Barnes & Fortney 2004; Zuluaga et al. 2015).

Among all the discovered exoplanets thus far, and despite that most of such planets are gas giants, the discovery of planetary rings remains elusive (e.g. Piro & Vissapragada 2020). Although the absence of rings around extrasolar planets might seem like an unsolved mystery, it could be due to the limitations of the methods and techniques we use to detect them. For instance, the rings around the giant planets of our Solar System were discovered through *in situ* observations by spacecraft, such as Voyager I and II for Jupiter and Neptune, and through the detection of anomalies in the light curve of precise stellar occultations for Uranus (Charnoz et al. 2018). However, current techniques to detect rings around exoplanets, similar to the latter method, have been unsuccessful thus far. Moreover, it is worth noting that a ringed exoplanet should project a larger area on the stellar disk than an exoplanet without rings, and so this type of exoplanet should have a larger apparent size when observed indirectly through planetary transits (Zuluaga et al. 2015, 2022; Ohno & Fortney 2022). However, during the rest of their orbital phase, and depending on the geometry of the system, planetary rings can contribute to a noticeable increase in stellar flux (Arnold & Schneider 2004; Dyudina et al. 2005; Sucerquia et al. 2020), increasing the chances of detection by an alternative route.

In light of the above, scattered/polarized light measurements have recently emerged as a crucial tool in the study of exoplanets, revealing valuable information about their properties that cannot be obtained using traditional techniques. For instance, instruments such as SPHERE/ZIMPOL intend to use light polarized from planetary surfaces to characterize cold planets (Knutson et al. 2007; Schmid et al. 2018), and other studies have proposed similar methods for the detection and characterization of directly imaged exoplanets using scattered light (see, e.g. Stam et al. 2004; Karalidi et al. 2012, 2013; Stolker et al. 2017). All of these techniques, along with the appropriate instruments, might help us understand the nature of many extrasolar systems that have behaviors still awaiting an explanation, such as the case of 55 Cancri e's phase curves with a time-varying occultation depth (Tamburo et al. 2018; Morris et al. 2021) that defy current models of light reflection and emission (Demory et al. 2022). Or the discoveries of "puffed-up" planets that appear to have extraordinarily low densities (Piro & Vissapragada 2020).

Moreover, polarimetry is also a valuable method for detecting and characterizing the magnetic fields of exoplanets, particularly those with a system of rings around them. As in the case of the giant planets in the Solar System (and in the debris disks around young stars), the effect of the planet's magnetic field on its rings can modify the optical properties of the particles that make up these structures by means of grain orientations (Dollfus 1984; Lazarian 2007), thus providing valuable information about the composition, structure, and dynamics of the planet's interior, which in turn could provide clues about the habitability of these worlds and their possible satellites (see, e.g. Heller & Zuluaga 2013, and references therein).

Regarding the above, this paper presents a novel addition to the `Pryngles` python package (see, Zuluaga et al. 2022) that enables the computation of flux, degree of polarization, and linearly polarized flux for ringed exoplanets. This upgrade to `Pryngles` uses data generated by the adding-

doubling algorithm, which includes the treatment of polarization and all orders of light scattering (de Haan et al. 1987), to compute the reflected light curves of ringed exoplanets.

Ideally, the ringed planet that we use in our simulations would resemble Saturn such that the computed flux and polarization phase curves could be verified with observations. This is, however, not possible due to the fact that ground-based telescopes (or space telescopes in the vicinity of Earth), can only see the giant planets at small phase angles. Therefore, the degree of polarization of the reflected light is very small because of the symmetric geometry. Observing these planets as if they were exoplanets is only possible with orbiters, such as the Cassini spacecraft. Cassini's Imaging Science Subsystem (ISS) instrument had polarimetric capabilities (Porco et al. 2004), but we have not found published polarimetric observations of Saturn and its ring system (West 2022).

It is important to note that previous work, such as that of Lietzow & Wolf (2023), has made considerable efforts to estimate the properties of the light scattered by planetary rings, as well as its degree of polarisation. However, the model presented in this paper does not use the assumption that the dust particles are spherical as a working hypothesis, but instead uses observations of actual particles which allows a more accurate calculation of the properties of the light emanating from these structures. In addition, the inclusion of our results in a freely available package such as `Pryngles` allows a quick implementation for the analysis of any candidate system with ringed planets. This also allows us to explore a much wider parameter space in terms of illumination and viewing geometries and ring orientations.

These new features of the `Pryngles` package allow for a more comprehensive and accurate simulation of the reflected light curves of ringed exoplanets. In fact, Sect. 2 gives a brief overview of the `Pryngles` package and the other numerical methods that we used for our simulations of the total and polarized fluxes and the degree of polarization of light that is reflected by ringed exoplanets. In Sect. 3, we describe the physical properties of the model planet and its ring that we used in this study. In Sect. 4, we present and discuss computed fluxes and polarization of our standard model planet-ring system and variations thereon. In Sect. 5, finally, we summarize and discuss the main implications of our results for the search and characterization of rings around exoplanets.

2. Numerical method

Figure 1 illustrates a ringed planet that is orbiting its parent star. The Saturn-like ring is inclined with respect to the observer and with respect to the planet's orbital plane (see also Fig. 2). Along the orbit, the illumination and viewing geometries of the planet-ring system change: it can be seen how the ring casts its shadow on different regions on the planet and/or how it sometimes occults different regions on the planet, and how the planet's shadow moves across the ring along the orbit. Also, for half of the orbit the ring is seen in reflected starlight (the bottom part of the figure), while for the other half (the upper part of the figure) it is seen in diffusely transmitted starlight.

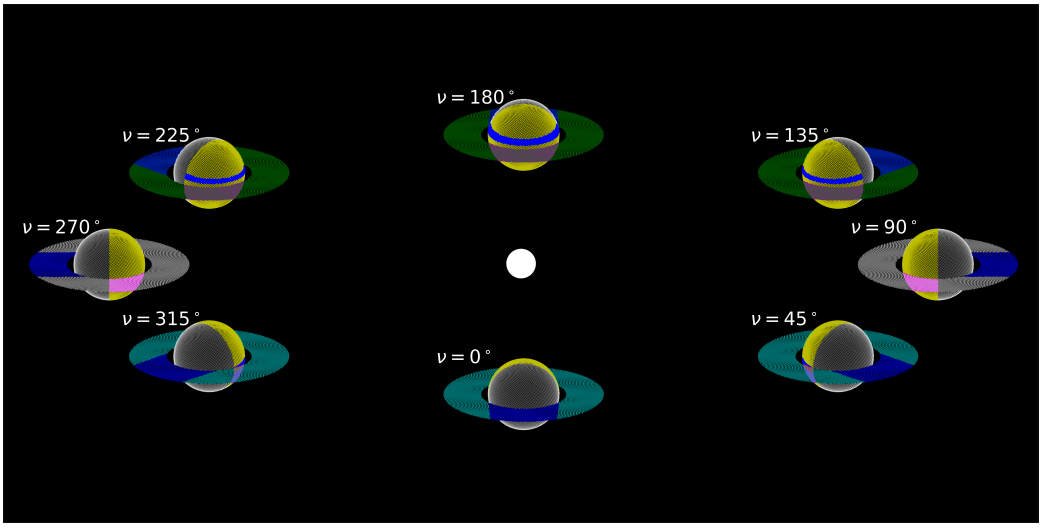

Fig. 1: An illustration of the various illumination and viewing geometries that can occur in a planet-ring system. The star (white dot) and the planetary orbit are not to scale. The circular planetary orbit has an inclination angle i of 60°. The ring has an inclination angle γ of 70° and an inclination longitude angle λ_r of 0° (this system is thus mirror–symmetric from left to right). The planet's true anomaly ν at each point is shown next to the planet and increases rotating anti-clockwise from 0° at the bottom-center. For this system, the ring-plane crossings occur at ν = 90° and 270°. Along the part of the orbit in the upper half of the figure, the ring is seen in diffusely transmitted starlight, while in the lower half of the figure, it is seen in reflected starlight (see also Fig. 2). Spangles that are dark-blue colored indicate shadows on the planet and/or the ring. The dark-gray, small patterns on the planet and the ring are a moiré pattern that is caused by the spangles used in `pryngles`.

Section 2.1 describes how we use the `Pryngles` package (see Zuluaga et al. 2022) to compute the illumination and viewing geometries of the planet and its ring along the orbit, which includes determining which regions on the planet and/or the ring are occulted and/or shadowed[1]. Section 2.2 provides our definitions of fluxes and polarization. Section 2.3 describes how we use that geometrical information to compute the starlight that is locally reflected by the planet or the ring, and the starlight that is transmitted through the ring. Section 2.4, finally, describes how we calculate the total flux and polarization signals of the planet-ring system along the planetary orbit.

2.1. The illumination and viewing geometries of the planet and its ring

To be able to compute the total flux and polarization of the starlight that is reflected by a planet and that is reflected or transmitted by the ring, we have to know the illumination and viewing geometries across the planet and the ring along the planetary orbit. `Pryngles` (Zuluaga et al. 2022) discretizes the surface (or upper atmosphere) of a planet and the surface of a ring with plane, circular area elements called 'spangles' (see Fig. 1), which resemble sequins or spangles found on elegant clothing. The spangles are uniformly distributed over a surface using Fibonacci spiral sampling, which prevents, for instance, oversampling. In particular, `Pryngles` incorporates the `fibpy` algorithm based on the work of Vogel (1979)[2]. The position and orientation of a given spangle are

[1] The region on the planetary disk that is occulted by the ring remains the same along the orbit as is the region of the ring that is occulted by the planet

[2] `fibpy` is available at `https://github.com/matt77hias/fibpy` (last accessed on April 6th, 2023.).

described by its spherical coordinates and its normal vector. Note that `Pryngles` assumes a flat, infinitely thin ring (see Sect. 3) and a given part of the ring is thus covered by a single spangle.

For each spangle, we have to know the local stellar zenith angle θ_0, which is the angle between the local zenith direction and the direction towards the star, the local viewing zenith angle θ, which is the angle between the local zenith direction and the direction towards the observer, and the local azimuthal difference angle $\phi - \phi_0$, which is the angle between the plane that contains the direction towards the local zenith and the direction towards the observer, and the plane that contains the direction towards the local zenith and the direction of propagation of the incident starlight. Angle $\phi - \phi_0$ is measured rotating in the clockwise direction when looking towards the local zenith. For a more detailed description of $\phi - \phi_0$ and how we calculate it, see the App. A. We assume uni-directional incident starlight, which precludes computations for planets that are in very close orbits around their stars.

As can be seen in Figs. 1 and 2, the illumination and viewing geometries in a planet-ring system generally depend not only on the location of the planet along its orbit, but also on the orbital inclination angle i, the ring inclination angle γ, and the azimuthal rotation angle λ_r of the ring if it is inclined with respect to the observer.

To compute all angles, `Pryngles` (Zuluaga et al. 2022) uses a Cartesian coordinate system centred on the planet with the ^+z-axis pointing towards the observer and the ^+x-axis in the plane of the ecliptic. The inclination of the planet's orbit, i, is defined as the angle between the xz-plane and the normal vector on the orbital plane (see Fig. 2). For $i = 0°$, the orbit is seen face-on, while for $i = 90°$, the orbit is seen edge-on. The position of the planet along its orbit, and thus its position with respect to the star, is given by the planet's true anomaly ν. At $\nu = 0°$, the planet is between the observer and the star (if $i \approx 90°$, it would be transiting its star), and at $\nu = 180°$, the star is between the observer and the planet. If $i = 0$, ν is defined to be such that $\nu = 0°$ when the planet is directly below the star, as viewed from the observer (see Fig. 2), and $\nu = 180°$ when the planet is directly above the star.

Except when $i = 0°$ (a face-on orbit), the planet's phase angle α changes with ν along the orbit. Angle α is defined as the angle between the directions to the star and the observer as measured from the center of the planet: if $\alpha = 0°$, the planet is fully illuminated (ignoring the possible influence of a ring), and if $\alpha = 180°$, the full nightside of the planet is in view. The range of values that α of a planet can attain along a given orbit, depends on inclination angle i (see also Fig. 2): $90° - i \leq \alpha \leq 90° + i$.

The orientation of the ring is described by its inclination angle, γ, and its inclination longitude angle, λ_r (see Figs. 1 and 2). Inclination angle γ is measured between the normal vector on the ring and the xz-plane: if $\gamma = 0°$ or $90°$, the ring is seen face-on or edge-on, respectively. The inclination longitude angle λ_r indicates how an inclined ring is rotated with respect to the observer (if $\gamma = 90°$, λ_r is undefined): it is the angle between the projection of the normal vector on the ring on the xz-plane and the ^+z-axis, measured anti-clockwise when looking towards the ^-y-axis.

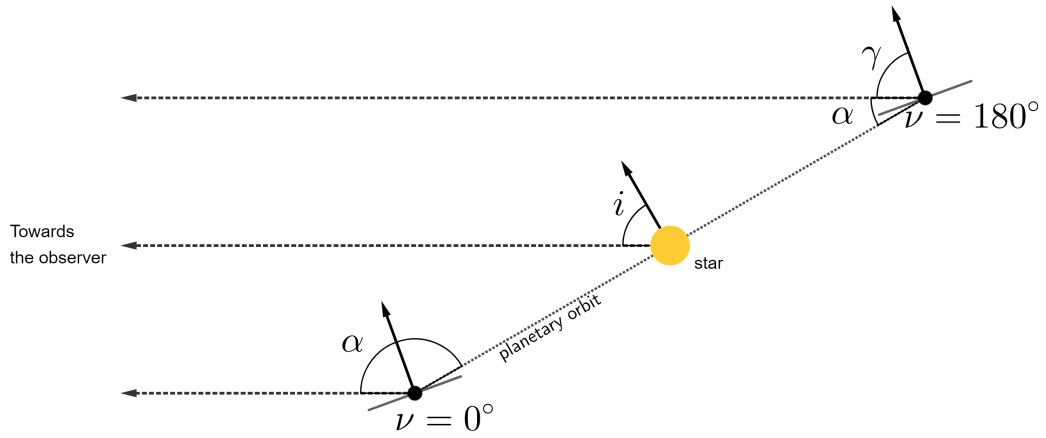

Fig. 2: Side-view of the planet-ring system that was also shown in Fig. 1 at the orbital locations where the planet's true anomaly ν is 0° and 180°. Indicated are: the orbital inclination angle i and the ring inclination angle γ, which equal, respectively, 60° and 70° for this system. Also shown is the planetary phase angle α, which equals $90° + i = 150°$ at $\nu = 0°$, and $90° - i = 30°$ at $\nu = 180°$.

Summarizing, given angles i, γ, and λ_r, `Pryngles` computes for each given true anomaly ν along the planetary orbit, phase angle α, and for each spangle on the planet and the ring, angles θ_0, θ, and $\phi - \phi_0$ (note that unlike the planet spangles, all ring spangles have the same illumination and viewing geometries). Then, taking into account the radius of the planet, and the inner and outer radii of the ring, `Pryngles` computes for each spangle that is both (in principle) illuminated by the star and visible for the observer, whether it is in the shadow of the ring (for planet-spangles) or the planet (for ring-spangles), and/or whether it is occulted by the ring (for planet-spangles) or the planet (for ring-spangles).

Note that because the ring will not be completely opaque, it will transmit direct and diffusely scattered starlight from the star onto the planet (spangles in the ring-shadow will thus not be completely dark) and it will transmit light from the planet towards the observer (the observer can 'see' the planet through the ring). With increasing ring optical thickness the contribution of this transmitted light will usually decrease (see Sect. 4.2).

`Pryngles` identifies so-called 'active spangles': these are illuminated, visible, and not obscured or shadowed by an opaque body. There can be up to six types of active spangles in our planet-ring system. Four types are active planet spangles:

Table 1: Conditions for the different planetary spangle types.

Spangle type	Shadowed	Occulted
1	no	no
2	no	yes
3	yes	no
4	yes	yes

In Fig. 1, type 1 spangles are yellow, type 2 spangles are purple, type 3 spangles are blue, and type 4 spangles are red. There are only a few type 4 spangles (that are thus both in the ring shadow and occulted by the ring) in Fig. 1: only at $\nu = 45°$ and 315°. And there are two types of active

ring spangles based on their interaction with the incident starlight (note that ring spangles in the shadow of the planet are inactive):

Table 2: Conditions for the different ring spangle types.

Spangle type	Reflecting	Transmitting
5	yes	no
6	no	yes

In Fig. 1, type 5 spangles are cyan, while type 6 spangles are green,

Because `Pryngles` assumes a flat, infinitely thin ring (see Sect. 3), the ring will be dark during the so-called ring-plane crossings, i.e. the locations where the parent star is in the ring-plane and thus illuminates the thin edge of the ring, which then cast an infinitely narrow shadow on the planet. At the ring-plane crossings, the ring spangles are thus effectively not illuminated and inactive. Due to our coordinate system, the true anomaly ν at which the ring-plane crossings take place depends not only on the ring inclination longitude λ_r but also the ring inclination γ and the orbital inclination i [3]. In Fig. 1, $\lambda_r = 0°$ and the crossings occur at $\nu = 90°$ and $270°$ (they are always $180°$ apart): in the figure the rings are colored white, just like the night-side of the planet, at the crossings. The location of the ring-plane crossings can be calculated by solving

$$\mathbf{n}_r \cdot \mathbf{n}_{star} = 0\,, \tag{1}$$

with $\mathbf{n}_r$ the normal vector of the ring in the observer reference frame and $\mathbf{n}_{star}$ the normal vector pointing from the planet to the star. By writing out this equation we get

$$\sin(\lambda_r)\cos(\gamma)\sin(\nu_{rp}) + (\cos(\lambda_r)\cos(\gamma)\sin(i) - \sin(\gamma)\cos(i))\cos(\nu_{rp}) = 0, \tag{2}$$

with ν_{rp} the true anomaly of the ring-plane crossings. While at the ring-plane crossings, the rings are not illuminated and cast only an infinitely narrow shadow on the planet, they can still occult part of the planet for the observer and thus still influence the total signal of the system.

In our simulations of the total flux and polarisation signals of the planet-ring system, we ignore light that is scattered by the ring and that is subsequently reflected by the planet towards the observer (ring-shine) and light that is reflected by the planet towards the ring and that is subsequently reflected or transmitted towards the observer (planet-shine). These contributions will in most cases be negligible (see Porco et al. 2008) and would unnecessarily complicate our numerical model.

[3] If the ring is in the orbital plane, there is a perpetual ring-plane crossing geometry.

2.2. Our definitions of light and polarization

We describe uni-directional beams of light using Stokes vectors (Hansen & Travis 1974; Hovenier et al. 2004)

$$\boldsymbol{F} = \begin{bmatrix} F \\ Q \\ U \\ V \end{bmatrix}, \tag{3}$$

with F the total flux, Q and U the linearly polarized fluxes, and V the circularly polarized flux, all measured in W m^{-2} or W m^{-3} if the wavelength is included. The circularly polarized flux V is usually very small compared to F, Q and U, so we will neglect it in our computations (Rossi & Stam 2018). This does not yield significant errors in the computed F, Q, and U (Stam & Hovenier 2005).

Linearly polarized fluxes Q and U are defined with respect to a reference plane. We will use different reference planes for the locally reflected and transmitted light (see Sect. 2.3) and for the light that has been reflected by the planet-ring system as a whole (see Sect. 2.4). Stokes vectors can be rotated from one reference plane to another using a so-called rotation matrix (see e.g. Hovenier et al. 2004). Neglecting circular polarization, a rotation matrix $\mathbf{L}$ is described by

$$\boldsymbol{L}(\beta_n) = \begin{bmatrix} 1 & 0 & 0 \\ 0 & \cos 2\beta_n & \sin 2\beta_n \\ 0 & -\sin 2\beta_n & \cos 2\beta_n \end{bmatrix}, \tag{4}$$

with β_n the angle between the old and the new reference planes, measured rotating in the anti-clockwise direction when looking towards the observer ($\beta_n \geq 0°$). For a description of how we calculate β_n, see App. A.

The choice of reference plane does not affect the polarized flux $F_{\rm pol}$ which is defined as

$$F_{\rm pol} = \sqrt{Q^2 + U^2}, \tag{5}$$

nor does it affect the degree of polarization P which is defined as

$$P = \frac{F_{\rm pol}}{F}. \tag{6}$$

2.3. The locally reflected and transmitted starlight

We can compute the Stokes vector of light that is either reflected by a spangle or transmitted by a (ring) spangle that arrives at the observer (see Sects. 2 and 3 in Zuluaga et al. 2022) once we have the illumination and viewing geometries for all the active spangles covering the planet and the ring.

To obtain the Stokes vector of light that is reflected by the planet-ring system as a whole, we will add the contributions of the individual spangles (see Sect. 2.4).

For the locally reflected or transmitted light, the reference plane for Stokes parameters Q and U is assumed to be the local meridian plane which contains the local zenith direction (of the spangle) and the direction towards the observer. Note that spangles covering the planet generally have different local meridian planes, whereas the ring spangles all have the same local meridian plane.

The Stokes vector that is locally reflected by a planet or ring spangle n ($n \leq N^{\mathrm{x}}$, the number of active spangles) at a given wavelength is calculated according to Hansen & Travis (1974):

$$\boldsymbol{F}_n^{\mathrm{x}}(\mu_{0n}, \mu_n, \phi_n - \phi_{0n}) = \mu_n \, \boldsymbol{R}_{1n}^{\mathrm{x}}(\mu_{0n}, \mu_n, \phi_n - \phi_{0n}) \, \mu_{0n} F_0, \tag{7}$$

where x is either 'p' or 'r' in case of a planet or a ring spangle, respectively. Furthermore, $\boldsymbol{R}_{1n}^{\mathrm{x}}$ is the first column of the local reflection matrix, $\mu_n = \cos\theta_n$ with θ_n the local viewing angle, $\mu_{0n} = \cos\theta_{0n}$ with θ_{0n} the local illumination angle, $\phi_n - \phi_{0n}$ is the local azimuthal difference angle, and F_0 the flux of the incident starlight measured perpendicularly to the propagation direction. We assume that this starlight is uni-directional and unpolarized when integrated over the stellar disk. This assumption is based on the very small disk-integrated polarized fluxes of active and inactive FGK-stars (Cotton et al. 2017) and on measurements of the Sun (Kemp et al. 1987). Indeed, because of this assumption, the full reflection matrix is not needed in Eq. 7 but only its first column.

The Stokes vector for light that is diffusely transmitted through the ring is calculated using:

$$\boldsymbol{F}_n^{\mathrm{x}}(\mu_{0n}, \mu_n, \phi_n - \phi_{0n}) = \mu_n \, \boldsymbol{T}_{1n}^{\mathrm{x}}(\mu_{0n}, \mu_n, \phi_n - \phi_{0n}) \, \mu_{0n} F_0, \tag{8}$$

with $\boldsymbol{T}_{1n}^{\mathrm{r}}$ the local transmission of the ring spangle. While transits are not the focus of this study it is good to mention that when modeling a transit the light that goes directly through the ring is diminished by a factor $\exp -b/\cos\theta_0$, where b is the optical thickness of the ring.

The local reflection and transmission matrices $\boldsymbol{R}_{1n}^{\mathrm{p}}$, $\boldsymbol{R}_{1n}^{\mathrm{r}}$, and $\boldsymbol{T}_{1n}^{\mathrm{r}}$ depend on the physical properties of the local spangle, such as the composition, size and shape of the scattering particles in the local planetary atmosphere or in the ring. `Pryngles` allows giving each spangle different properties, but to not complicate our numerical simulations too much, we use a single set of properties for the planet spangles and a single set of properties for the ring spangles, as described in more detail in Sect. 3, and compute the local reflection and transmission matrices for those properties.

We do not calculate the reflection and transmission matrices for each spangle and local illumination and viewing angles separately but instead use coefficients of the Fourier expansion of $\boldsymbol{R}_1^{\mathrm{p}}$, $\boldsymbol{R}_1^{\mathrm{r}}$, and $\boldsymbol{T}_1^{\mathrm{r}}$. These Fourier coefficients have been pre-calculated for various combinations of μ_0 and μ using an adding–doubling algorithm that fully includes polarization for all orders of scattering (see de Haan et al. 1987, for a detailed description of the adding-doubling algorithm and the Fourier series expansion). Using pre-calculated coefficients saves a lot of time when having to compute the reflection and transmission matrices for the many different geometries that we encounter across the

planet and the ring along the orbit. For spangle combinations of μ_0 and/or μ that have not been pre-calculated, $\boldsymbol{R}^{\rm p}_{1n}$, $\boldsymbol{R}^{\rm r}_{1n}$, and $\boldsymbol{T}_{1n}$ are calculated using bi-cubic spline interpolation. This use of Fourier coefficients is also described by Rossi et al. (2018).

2.4. The reflected starlight of the planet-ring system

The Stokes vector of the starlight that is reflected by the spatially unresolved planet-ring system can be written as

$$\boldsymbol{F} = \boldsymbol{F}^{\rm p} + \boldsymbol{F}^{\rm r} \tag{9}$$

where $\boldsymbol{F}^{\rm p}$ and $\boldsymbol{F}^{\rm r}$ are the Stokes vectors of the planet and the ring, respectively.

The Stokes vector $\boldsymbol{F}^{\rm p}$ of the light that is reflected by the planet can be written as the sum of the local Stokes vectors over the $N^{\rm p}$ active spangles on the planet, as follows

$$\boldsymbol{F}^{\rm p}(\nu) = \frac{F_0}{d^2} \sum_{n=1}^{N^{\rm p}} e^{-ba_n}\, \mu_n\, \mu_{0n}\, \boldsymbol{L}(\beta_n)\, \boldsymbol{R}^{\rm p}_{1n}(\mu_n, \mu_{0n}, \phi_n - \phi_{0n})\, {\rm d}O_{n,{\rm p}}, \tag{10}$$

with d the distance between the planet-ring system and the observer, b the optical thickness of the ring (see Sect. 3), ${\rm d}O_n$ the surface area of a spangle, $\mathbf{L}(\beta_n)$ is a rotation matrix (see Sect. 2.2), and a_n a parameter that depends on the type of spangle and that describes the influence of the occultation by the ring and/or the ring shadow. The surface area of every planetary spangle is the same and $4\pi r^2 = \sum_n^{N^{\rm p}} {\rm d}O_{n,{\rm p}}$, with r the radius of the planet.

The value of parameter a_n for each of the four types of active planet spangles (see Sect. 2.1) is as follows:

Table 3: The value of the parameter a_n for every spangle type.

Spangle type	a_n
1	0.0
2	$\cos^{-1}\theta_n$
3	$\cos^{-1}\theta_{0n}$
4	$\cos^{-1}\theta_n + \cos^{-1}\theta_{0n}$

The rotation matrix $\boldsymbol{L}$ in Eq. 10, is used to rotate each local Stokes vector, defined with respect to the local meridian plane, to the reference plane of the planet-star system as a whole before adding it to the total sum. For the system as a whole, we use a reference plane that is fixed with respect to the planet and its ring, equivalent to the xz-plane when viewed from the observer reference frame. We will call our reference plane 'the detector plane', as it is fixed to an observer or telescope on or near the Earth[4].

[4] This detector plane is generally different from the reference plane employed by e.g. Stam et al. (2004); Rossi et al. (2018) as that is the plane through the star, the planet, and the observer. That so-called 'planetary scattering plane' is convenient for planets that are mirror-symmetric with respect to the line through the planet and the star, as then the planet's Stokes parameter U will equal zero. However, for a planet with a ring, U will generally not equal zero with respect to the planetary scattering plane. Without this benefit, the detector plane appears to be more directly connected to observations.

The Stokes vector of the ring, $\boldsymbol{F}^{\mathrm{r}}$ that appears in Eq. 9 can be written as

$$\boldsymbol{F}^{\mathrm{r}}(\alpha) = \frac{F_0}{d^2} \sum_{n=1}^{N^{\mathrm{r}}} \mu\, \mu_0\, \boldsymbol{L}(\beta)\, \boldsymbol{R}^{\mathrm{r}}_{1n}(\mu, \mu_0, \phi - \phi_0)\, \mathrm{d}O_{n,\mathrm{r}}, \tag{11}$$

along the part of the orbit where the ring reflects the incident starlight (in Fig. 1, the part from $\nu = 270°$ till 90°), with N^{r} the number of active ring spangles, or as

$$\boldsymbol{F}^{\mathrm{r}}(\alpha) = \frac{F_0}{d^2} \sum_{n=1}^{N^{\mathrm{r}}} \mu\, \mu_0\, \boldsymbol{L}(\beta)\, \boldsymbol{T}^{\mathrm{r}}_{1}(\mu, \mu_0, \phi - \phi_0)\, \mathrm{d}O_{n,\mathrm{r}}, \tag{12}$$

along the part of the orbit where the ring is seen in transmitted light (in Fig. 1, the part from $\nu = 90°$ till 270°). Note that for the flat ring, μ, μ_0, $\phi - \phi_0$, and β are the same for all spangles at a given location along the orbit. Indeed, μ is the same along the whole orbit. Just as with the planetary spangles, the surface area of all the ring spangles is the same.

Varying the eccentricity of the orbit is possible in `Pryngles`. In this study, however, we assume a circular orbit to reduce the number of free parameters in Sect. 4. Also, it is possible to convert the results as if they were for an eccentric orbit. The total and polarized fluxes would need to be multiplied by a factor that represented the actual incident flux on the planet and its ring. As Kane & Gelino (2010) showed, the observed flux curves can be strongly affected by the eccentricity of the orbit. A potential complexity with simulating a ringed planet that has a large eccentricity is that, depending on the size of the rings and the semi-major axis of the orbit, the illumination angle might no longer be uniform across the ring. We assume uniform illumination angles across the ring for our results but `Pryngles` has the capability to calculate the direction of incoming light for every spangle individually.

For the results presented in Sect. 4, we use

$$F_0\, \frac{r^2}{d^2} = 1, \tag{13}$$

with r the radius of the planet. We further normalize the reflected fluxes such that at $\alpha = 0°$, the flux that is reflected by the planet without the ring equals the planet's geometric albedo. Adapting the results to a specific planetary system will then just involve scaling our computed fluxes with the relevant values of F_0, r, and d. For that reason, the fluxes that we present are unit less.

3. Properties of the model planet and its ring

Our model planet will be kept simple to focus on the effect that a ring has on the reflected flux and polarization curves. The planet will be perfectly spherical with a simple, purely gaseous atmosphere that is bounded below by a Lambertian reflecting surface with an albedo of 0.5, mimicking a deep cloud layer. The gas molecules in the atmosphere are anisotropic Rayleigh scatterers with a depolarization factor of 0.02, a typical value for H_2 (Hansen & Travis 1974). In future studies, clouds and/or absorbing molecules like CH_4 could be added to simulate the more complex plan-

etary atmospheres that are found in our Solar System. Examples of the effects of adding clouds or absorbing methane gas on the total flux and polarization signals of planets can be found in (for example, Stam et al. 2004; Karalidi et al. 2012, 2013; Rossi et al. 2018). The effect that something like planetary oblateness has on the flux and polarization could also be added in future studies. Examples of the effect of planetary oblateness on the flux can be found in Dyudina et al. (2005) and the effect of a combination of clouds and oblateness on the flux and degree of polarization can be found in Stolker et al. (2017).

To focus on the effect of a ring on the reflected flux and polarization signals, we use a simple, spherical model planet. The effects of planetary oblateness on the reflected light signals mostly show a dependency on the amount of visible and illuminated planet area (Dyudina et al. 2005).

The ring we use is flat, circular, horizontally homogeneous, and its inner and outer radii are denoted as $r_{\rm in}$ and $r_{\rm out}$, respectively. We express these radii in fractions of the radius of the planet. While geometrically, the ring is infinitely thin, it is composed of irregularly shaped particles. The total flux and polarization of light that interacts with the ring depends besides on the illumination and viewing geometries, on the ring optical thickness, and the optical properties of the ring particles like their single scattering albedo ϖ and scattering matrix (Mishchenko 2009).

Both the single scattering albedo and scattering matrix depend on the size, shape, and composition of the particles, and, for non-spherical particles, on their orientation. Our model ring particles are irregularly shaped and randomly oriented. Using irregularly shaped particles is important to avoid sharp angular features such as rainbows or glories that are typical features when using spherical particles (Goloub et al. 2000; Nousiainen et al. 2012). The single scattering properties of our ring particles are based on laboratory measurements of light that is singly scattered by olivine particles (Muñoz et al. 2000). The scattering matrix of these particles was calculated by Moreno et al. (2006) using the Discrete Dipole Approximation (DDA) method (Draine & Flatau 1994, 2004) to fit the measurements. The light scattering measurements have been done at both 442 and 633 nm. We use the 633 nm data, keeping in mind the wavelength region and capabilities of JWST (Rieke et al. 2005; Jakobsen et al. 2022).

The flux F and degree of polarization P of the light that is singly scattered by the particles is shown in Fig. 3 together with F and P of the gaseous molecules. Note that in the measurements by Muñoz et al. (2000), the phase functions have not been absolutely calibrated since the number of particles in the aerosol beam in the laboratory experiment is not known. The singly scattered fluxes, which are also called the phase functions, have been normalized such that their average over all directions equal one (Hansen & Travis 1974).

For use in our adding-doubling radiative transfer algorithm, we expand the scattering matrix elements into generalized spherical functions (de Rooij & van der Stap 1984). Specifically, the matrix elements are representative for what Moreno et al. (2006) call the 'shape 5' particles, with an average projected surface area of 4.2 μm^2 and equivalent radii of up to 1 μm. The modeled ring will therefore be more akin to the E-ring of Saturn which has particle sizes between 0.2 and 10 μm

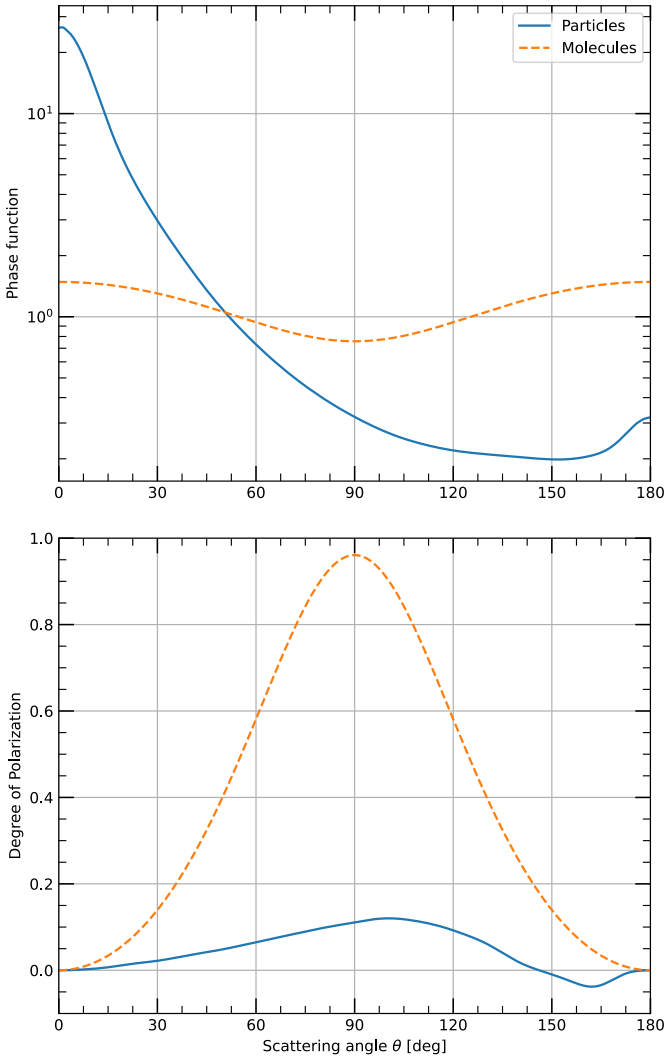

Fig. 3: The phase function or flux (top) and degree of polarization (bottom) of incident unpolarized light that has been singly scattered by gas molecules (orange, dashed) and the irregularly shaped ring particles (Moreno et al. 2006) (blue, solid) as functions of the single scattering angle Θ. The fluxes have been normalised such their average over all scattering directions equals one (Hansen & Travis 1974). Positive (negative) polarization indicates a direction of polarization perpendicular (parallel) to the plane through the incident and scattered light beams.

(Ye et al. 2016). Using larger, macroscopic particles would mean that their mutual shadowing would have to be taken into account. This is not needed to illustrate the basic effects of a ring on the reflected flux and degree of polarization of a planet.

Our model ring is assumed to be horizontally homogeneous with an optical thickness b, the value of which we will vary between 0.01 and 4.0. This is approximately the range of optical thicknesses at visible wavelengths found across Saturn's horizontally inhomogeneous rings (Lissauer & de Pater 2019).

4. Results

Before presenting and discussing the reflected light signals of planets with rings, we first discuss the signals of a planet without a ring. Figure 4 shows the reflected flux F, the polarized flux $F_{\rm pol}$,

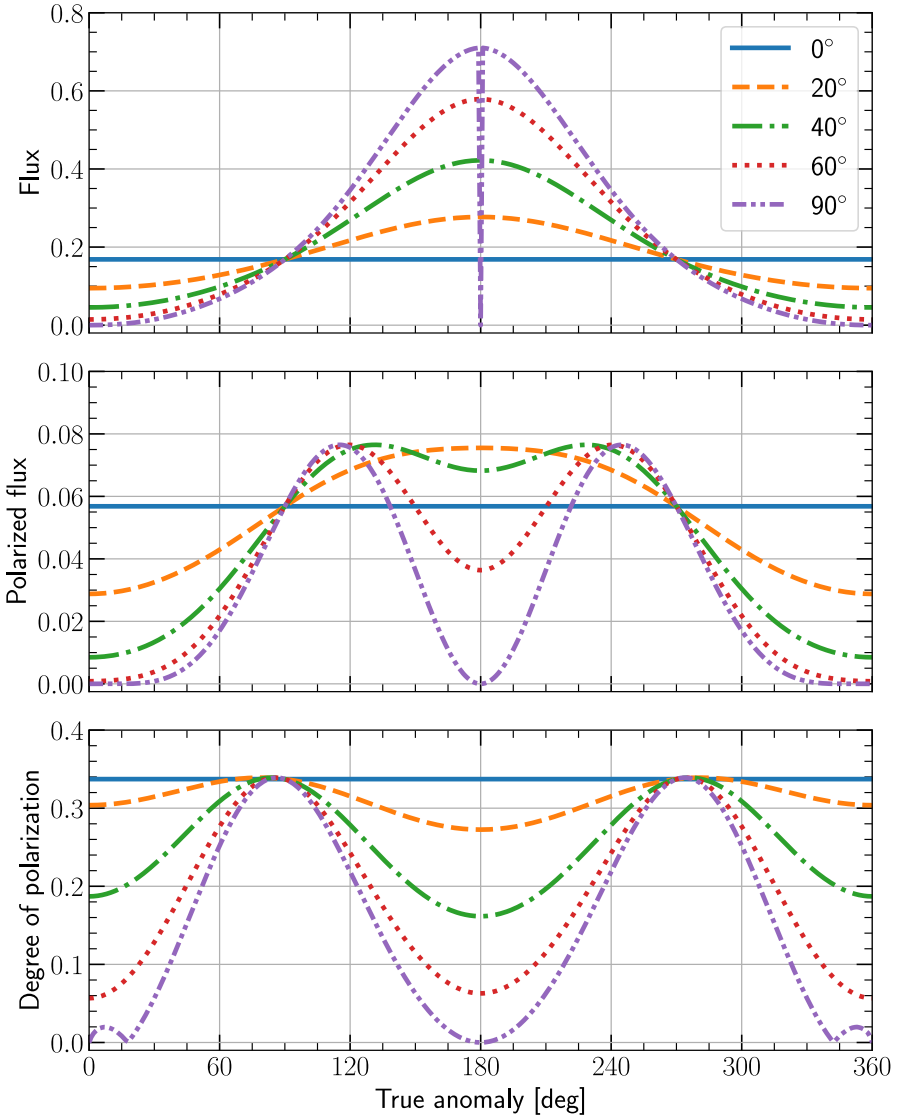

Fig. 4: The influence of the orbital inclination angle i on the reflected light of the ring-less planet as functions of the planet's true anomaly ν. From top to bottom: total flux F, polarized flux $F_{\rm pol}$, and degree of polarization P. For $i = 0°$, phase angle α is 90° everywhere along the orbit. For $i > 0°$, the planet is at its maximum phase angle $\alpha_{\rm max}$ at $\nu = 0°$ and 360°, and at its minimum phase angle $\alpha_{\rm min}$ at $\nu = 180°$ (for $i = 90°$, the planet is then precisely behind its star). The different lines pertain to the following combinations: $i = 0°$ (solid, blue): $\alpha = 90°$; $i = 20°$ (dashed, orange): $\alpha_{\rm min} = 70°$, $\alpha_{\rm max} = 110°$; $i = 40°$ (dot-dashed, green): $\alpha_{\rm min} = 50°$, $\alpha_{\rm max} = 130°$; $i = 60°$ (dotted, pink): $\alpha_{\rm min} = 30°$, $\alpha_{\rm max} = 150°$; $i = 90°$ (dot-dashed, purple): $\alpha_{\rm min} = 0°$, $\alpha_{\rm max} = 180°$.

and the degree of polarization P of our model planet as a function of the planet's true anomaly ν for orbital inclination angles i ranging from 0° (a face-on orbit) to 90° (an edge-on orbit). Similar curves, although not computed using `Pryngles`, have been presented by e.g. Stam et al. (2004); Buenzli & Schmid (2009) and the curves presented here are in agreement with those.

As can be seen in Fig 4, for $i = 0°$, phase angle α is always 90°, and consequently, F, $F_{\rm pol}$, and P are constant along the orbit. For $i > 0°$, the planets are at their largest phase angles at $\nu = 0°$ and 360°, while at $\nu = 180°$, they are at their smallest phase angles. For the edge-on orbit with $i = 90°$, the planet is precisely in front of its star at $\nu = 0°$ and 360°, and thus in transit, and at $\nu = 180°$, the

planet is precisely behind its star. While transit signals can be computed with `Pryngles`, they are not included in our simulations.

As expected, P is largest around $\nu = 90°$ and 270° when $\alpha \approx 90°$ and the single scattering degree of polarization of the gaseous molecules is highest (see Fig. 3). The peak polarized flux shifts towards $\nu = 180°$ with decreasing i because it is modulated with the total amount of reflected light, which increases with decreasing α. The small peaks in P for $i = 90°$ and small and large values of ν are caused by light that has been scattered twice (Stam et al. 2004). The direction of polarization of this light is parallel to the detector plane.

To explore the influence of a ring on the reflected light of a planet-ring system, we define a standard system with a wide ring with $r_{\rm in} = 1.2$ and $r_{\rm out} = 2.25$ planet radii, similar to Saturn's ring (Lissauer & de Pater 2019). The ring optical thickness b is 1.0 and the ring particles have a single scattering albedo ϖ of 0.8. Such a high albedo mimics the bright, icy particles in Saturn's ring. Considering the small probability that a ring has either exactly $\gamma = 0°$ or $\gamma = 90°$ and $\lambda_{\rm r} = 0°$ or $\lambda_{\rm r} = 90°$, we use more arbitrary parameter values. For our standard system, $i = 20°$, $\lambda_{\rm r} = 30°$, and $\gamma = 60°$. Using Eq 1 we can calculate that the ring-plane crossings in this system happen at $\nu = 69.4°$ and $\nu = 249.4°$. Between these true anomalies, the ring is seen in diffusely transmitted light, while at smaller or larger values of ν, the ring is seen in reflected light.

In Sect. 4.1, we vary the ring orientation and orbital inclination. In Sects. 4.2 and 4.3, we show the influence of the optical thickness b of the ring and the ring particle albedo ϖ. And lastly, in Sect. 4.4, we look at the effect of different values of the outer ring radius $r_{\rm out}$ on the light curves.

4.1. The influence of the ring orientation

Here we show the influence of the orientation of the ring for a given planetary orbital inclination angle i. To limit the number of free parameters, we consider only two orbital inclination angles i, namely 20° and 90°, with the first inclination angle representing a planetary system that would have been discovered using direct imaging, and the latter a system typically discovered using the transit method.

Figure 5 shows for $i = 20°$, F, $F_{\rm pol}$, and P for ring inclination angles γ equal to 0° (a face-on ring), 30°, 60°, and 90° (edge-on), and for ring inclination longitudes $\lambda_{\rm r}$ equal to 0°, 30°, 60°, and 90°. Figure 6 is similar to Fig. 5 except for $i = 90°$. For comparison, the figures also include lines representing the planet without a ring for the same i. Most of the curves in Figs. 5 and 6 show angular features that are predominantly due to changing shadows (cf. Fig. 1). We will not discuss all features in detail but rather point out a few characteristic ones.

First, while the phase curves of the planet itself are symmetric around $\nu = 0°$, a non-zero ring inclination longitude $\lambda_{\rm r}$ makes them asymmetric. This has already been noted by Arnold & Schneider (2004); Dyudina et al. (2005). We first discuss the case of $i = 20°$ (Fig. 5). All curves with $\gamma = 90°$ (an edge-on ring) are the same, because the view on the ring is independent of $\lambda_{\rm r}$. In this edge-on orientation, the observer will receive no light that has either been reflected or

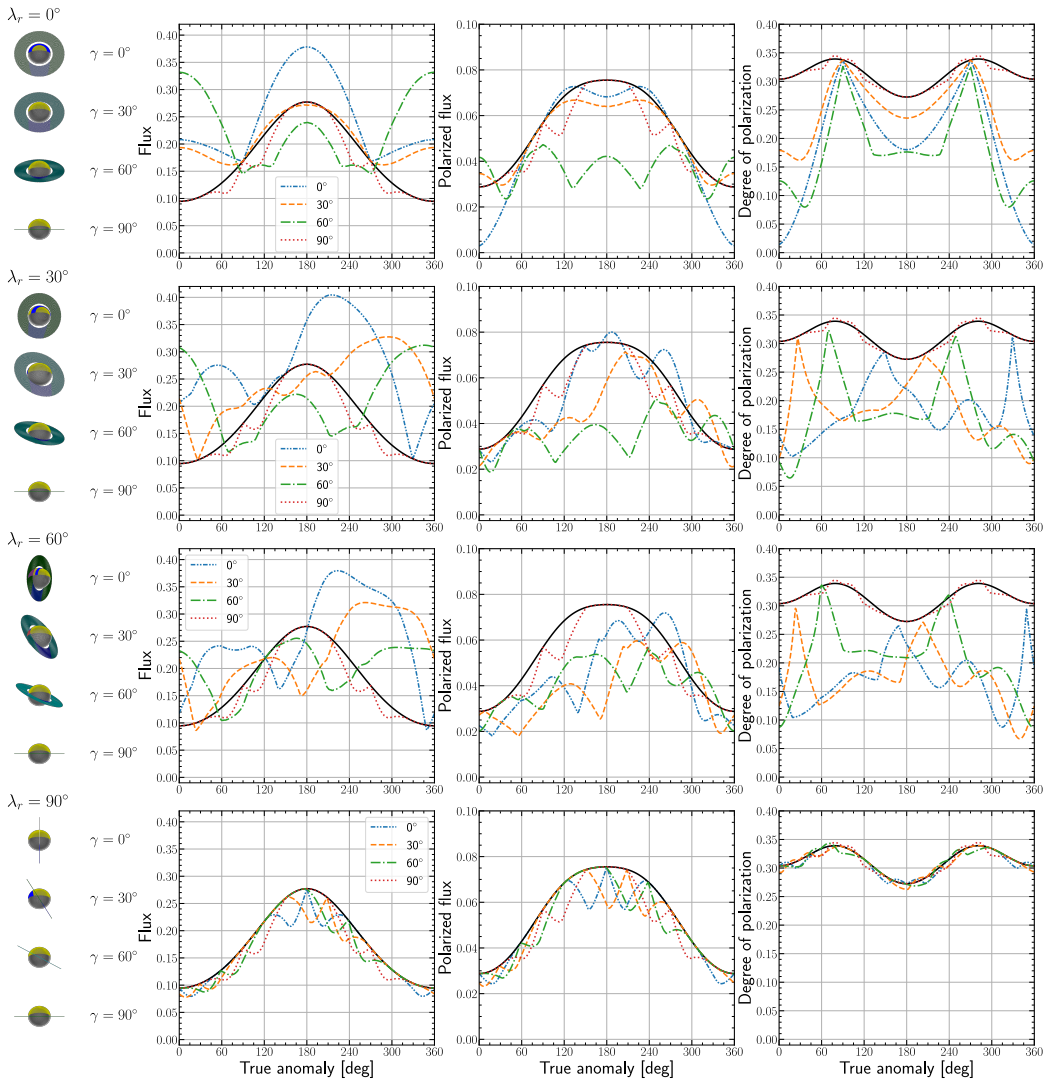

Fig. 5: F (left), $F_{\rm pol}$ (middle), and P (right) of the light that is reflected by the model planet with a Saturn-like ring with $r_{\rm in} = 1.2$ and $r_{\rm out} = 2.25$, $b = 1.0$, and $i = 20°$ ($\alpha_{\rm min} = 70°$ and $\alpha_{\rm max} = 110°$) as functions of the true anomaly ν. The ring inclination longitude $\lambda_{\rm r}$ is 0° (first row), 30° (second row), 60° (third row), and 90° (bottom row). For $\lambda_{\rm r} = 90°$ the ring is edge-on. The ring inclination angle γ is 0° (blue, dash-dot-dot), 30° (green, long-dashed), 60° (red, long-dash-dot), or 90° (purple, dot-dot). For $\gamma = 90°$, there is no dependence on $\lambda_{\rm r}$. The black lines are for the planet without a ring. The images on the left illustrate the planet with its ring at $\nu = 0°$, thus when it is between the star and the observer.

transmitted by the ring. That does, however, not mean that the ring leaves no trace in the light curves: the shadow the ring casts on the planet reduces F and $F_{\rm pol}$ mostly between approximately $\nu = 50°$ and 130°, and 230° and 310°. For $\lambda_{\rm r} = 90°$, the ring is seen edge-on independent of γ and all differences with the ring-less planet curves are thus due to ring shadows on the planet.

For all geometries, the curves approach the curves of the ring-less planet at the ring-plane crossings, where the ring is illuminated on its edge and the shadow is infinitely narrow. Depending on its orientation, the ring can, however, still occult part of the planetary disk at the ring-plane crossings, thus preventing the curves to be equal. An example of this is the curve for $\lambda_{\rm r} = 0°$ and $\gamma = 60°$, where F of the ringed planet is slightly lower than that of the ring-less planet at the ring-plane crossing. For $\lambda_{\rm r} = 0°$, the ring-plane crossings occur at $\nu = 90°$ and 270° but for other values

of λ_r and/or γ (the latter only when $\lambda_r \neq 0$), the location of the ring-plane crossings are different and can be calculated using Eq. 1.

The ring-plane crossings usually manifest themselves in the light curves as sharp discontinuities. A prime example of this discontinuity in Fig. 5 is the $\gamma = 60°$ curve at $\lambda_r = 0°$. Between $\nu = 0°$ and $\nu = 90°$, the ring reflects light, strongly increasing F of the planet-ring system compared to that of a ring-less planet. After the ring-plane crossing, the ring instead transmits light and casts a shadow on the planet, decreasing F. The $\gamma = 0°$ curve in the same plot shows similar behavior but here the ring transmits and reflects along different parts of the orbit. The ring-plane crossings appear to be even more pronounced in P than in the F and $F_{\rm pol}$ curves.

Looking at plots for $F_{\rm pol}$, it is clear that the light that is reflected or transmitted by the ring is usually less polarized than the light that is reflected by the planet and this suppresses P of the system as a whole. This is straightforward to understand by looking at Fig. 3: on top of having a lower P, at large scattering angles (small phase angles) the particles in the ring also scatter the light with an opposite direction of polarization compared to the light that is scattered by the gas in the planetary atmosphere, which further decreases P.

The ring shadow on the planet can increase P as it can break the symmetry of the illuminated and visible part of the planet. Clear examples of this are all the curves with $\gamma = 90°$. The edge-on orientation of the ring prevents it from adding any reflected flux but there is still a slight increase in P just before and after the ring-plane crossings. Another example is the initial dip in the curves that $\gamma = 60°$ has for both $\lambda_r = 0°$ and 30°. For these geometries, the ring will cast a shadow on the planet just before the ring-plane crossing, further increasing the sharpness of the discontinuity.

The changes to the polarized flux curves due to the ring are less straightforward to understand because it is not consistently lower than a ring-less planet. For example, for $\lambda_r = 30°$ or $\lambda_r = 60°$ the amount of polarized light is often higher in the second part of the orbit. This is a combination of no, or less, shadowing of the planet by the ring and a high ring flux which, even though it has a lower P, still has some P. The latter point is also clearly visible in polarized flux curves in Fig. 6 for $\lambda_r < 90°$ that show bumps in the polarized flux curves at the beginning and end of their orbit.

It is interesting to note that although the ring does not reflect any light when $\lambda_r = 90°$, the presence of the ring, while faint, is still visible. In fact, very few geometries allow the ring to be completely undetected. One such geometry is shown in Fig. 6. When $\gamma = 90°$ the thin ring does not cast a shadow nor does it reflect light. In fact, with the current model, any configuration where the orbital inclination is the same as the ring inclination the ring is undetectable. If planet-shine was to be added, the cases where the ring would be completely undetectable decrease to only one: $\gamma = 90°$ and $i = 90°$.

Looking at an i of 90° in Fig. 6, the first thing to note is that the ring is much brighter when transmitting light compared to when it's reflecting light, the opposite of the behavior that was seen in Fig. 5. To increase the clarity of the figure the peaks around 0° and 360° are cut off at 1, the value of the peaks are mentioned in the figure subtext. The peaks can again be explained by looking at

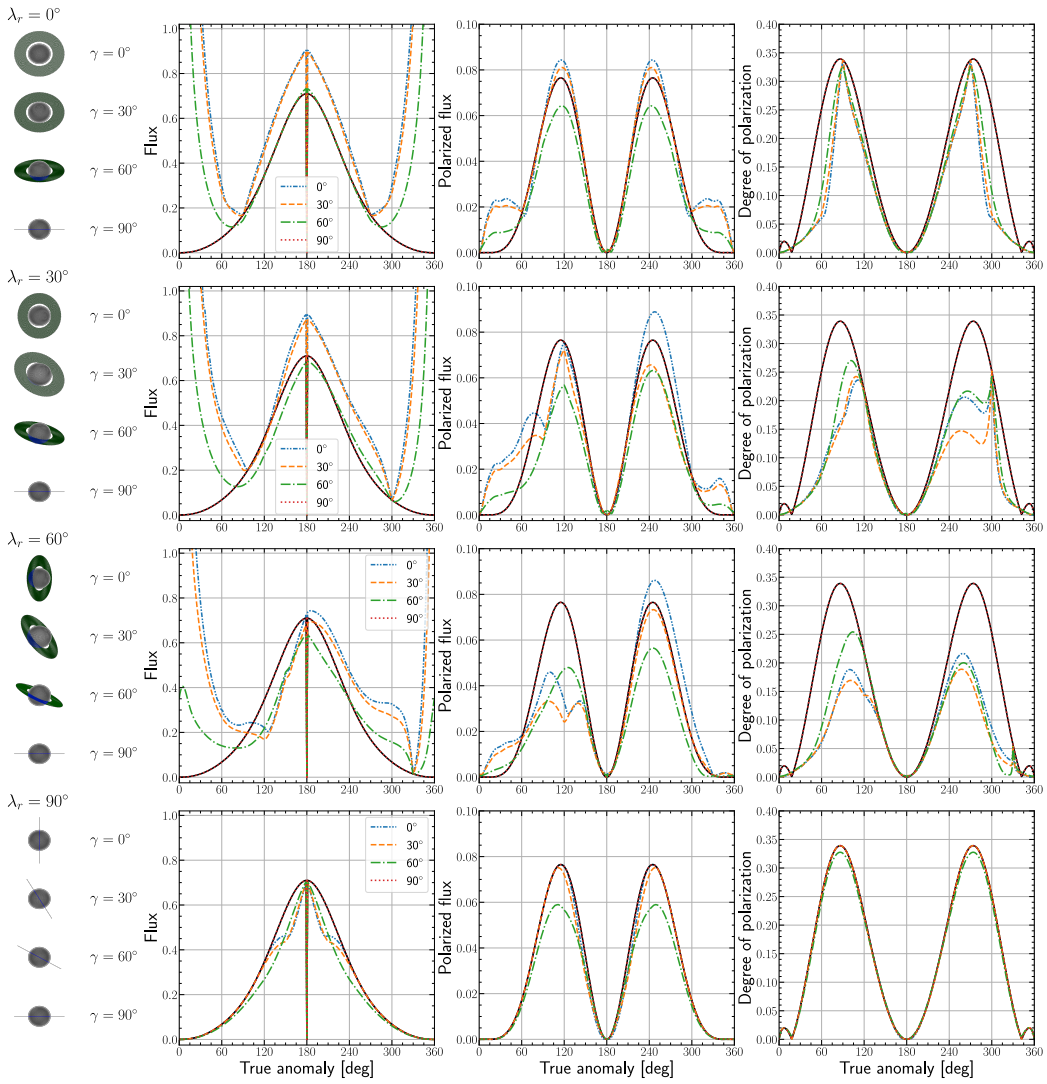

Fig. 6: Similar to Fig. 5, except for $i = 90°$. The images on the left illustrate the system at $\nu = 0°$, which, for $i = 90°$, is precisely in front of the star, thus the nightside of the planet is turned towards the observer. To keep the structures in the curves visible, we have limited the vertical axis in the graphs for F, thus in some cases cutting off the forward scattering peaks. The missing peak values are the following: for $\lambda_r = 0°$ the lines reach 6.13, 5.37, and 2.25 for $\gamma = 0°$, 30°, and 60°, respectively. For $\lambda_r = 30°$, they reach 5.36, 4.61, and 1.55, and for $\lambda_r = 30°$ 2.38 and 1.65 for $\gamma = 0°$ and $\gamma = 30°$, respectively.

Fig. 3 and the large peak at a scattering angle of 0°. The forward scattering flux of the ring particles can be almost a factor of 10 brighter than the maximum planetary flux. This peak also happens at a moment in the planet's orbit when the planet itself is very faint. Only considering the curves as shown in Figs. 5 and 6 it might seem that a system with $i = 90°$, $\lambda_r = 0°$, and $\gamma = 0°$ would be more easily observed than any situation in Fig. 5. Practically, however, the large peak would be hard to observe using direct imaging due to the small angular separation of the planet from the star at that moment in its orbit. Depending on the distance to the star and the size of the planet and ring these peaks could however be observable as stellar fluctuations. This has already been demonstrated (Placek et al. 2014) in the infrared where a hot giant planet is comparatively much brighter (Stam et al. 2004) but could in theory also be done in the visible part of the spectrum (Sucerquia et al. 2020).

Rotating the ring inclination longitude moves the ring-plane crossing but does not move the location of the peak as it did in Fig. 5. This is to be expected as a scattering angle of 0° can only happen when the ring is in between the observer and the star. The dramatic drops in P that were present in Fig. 5 are still present in Fig. 6 but no longer completely change the shape of the curve. Instead, the peak P is often only lowered, making it difficult to distinguish the curves from a ring-less planet. A ring-less planet with clouds or an atmosphere that has a different molecular make-up, for example, can already change the P significantly (see Stam et al. 2004; Karalidi et al. 2012). Possible exceptions to the decreased distinguishability are the curves with $\lambda_r = 30°$ as they show unsymmetrical behavior. Observations during the two points in the orbit with the largest angular separation, $\nu = 90°$ and $\nu = 270°$, would measure different valeus for F as well as for P. Such unsymmetrical behavior is also possible due to seasonal effects for a horizontally inhomogeneous ring-less planet as was already remarked by Dyudina et al. (2005). Seasonal effects can however not explain the sharp changes at, for example, $\nu = 300°$ in F and P that occur at the ring–plane crossings. These occurrences would therefore be something to search for.

4.2. The influence of the ring optical thickness

Figure 7 shows the influence of the ring optical thickness b on F, F_{pol}, and P of the light that is reflected by the standard planet-ring system. First, we'll discuss the influence of b on the light of the system along the part of the orbit where the ring reflects, then the more complicated influence along the part of the orbit where the ring diffusely transmits the incident light.

Where the ring reflects incident light ($\nu < 69.4°$ and $\nu > 249.4°$ in Fig. 7), the ring generally increases the F of the system as whole, and this increase in F increases with b. The reflected F does, however, not increase linearly with b: Fig. 7 shows that with increasing b, the increase in F vanishes because the reflection by the ring reaches its asymptotic value. Note that along this part of the orbit, the planet casts its shadow on a large part of the ring, which decreases the contribution of F of the ring, although part of this shadow is also on the night-side of the planet, while the ring hardly casts a shadow on the planet.

In reflected light, the polarized flux F_{pol} of the system is smaller than that of the ring-less planet at the small values of ν, while it is larger at the large values of ν, and the difference increases with increasing b but converges for the larger values of b. The reason for the lower and higher values of P when the ring is added are due to the P of the light that is singly scattered by the ring particles, which has an opposite direction of the P of the planet at the small values of ν, where the single scattering angle is larger than 150°, and the same direction at the largest values of ν, where the single scattering angle is smaller than 150° (see Fig. 3).

What happens along the orbit where the ring diffusely transmits light ($69.4° < \nu < 249.4°$) is more complicated: light that is transmitted through the ring adds to the flux of the system, and at the same time shadows cast by the ring on the planet and the occultation by the ring of otherwise illuminated parts of the planet play an important role by suppressing the flux of the planet (see

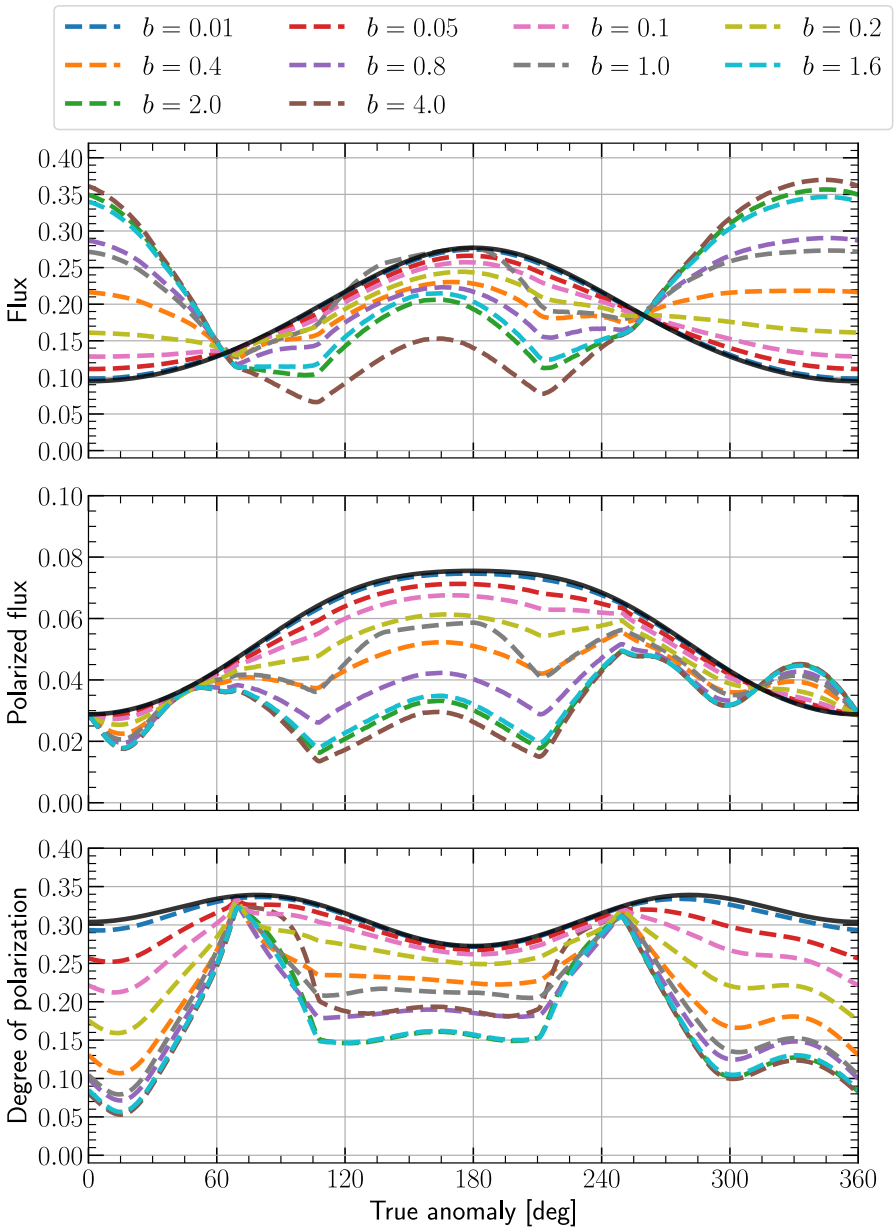

Fig. 7: F (top), $F_{\rm pol}$ (middle), and P (bottom) as functions of ν for different values of the ring optical thickness b. For this planet-ring system, $i = 20°$, $\lambda_{\rm r} = 30°$, $\gamma = 60°$, $r_{\rm in} = 1.20$, $r_{\rm out} = 2.25$, and $\varpi = 0.8$. Optical thickness b ranges from 0.01 (dark blue) to 4.0 (brown). The solid black line represents the planet without a ring.

Fig. 1). Figure 8 shows F, $F_{\rm pol}$, and P of the diffusely transmitted light for a viewing angle of 0°, different angles of incidence and as functions of b. The curves for F increase with b due to increased scattering of light by the ring particles, until about $b = 1$ to 3 (depending on θ_0 and θ as that affects the effective optical thickness). For $b = 1$, F increases to higher than the flux of the planet without ring. Increasing b further leads to a decrease of F as less and less photons manage to get through the ring. The large drop in F when $b = 4$ can be explained as a combination of a decreased planetary flux due to the shadowing and occultation and a strong drop-off in the transmitted light by the ring.

The relative larger values of F between about $\nu = 100°$ and $210°$, with the peak around $\nu = 160°$ are due to the changing size of the shadow of the planet on the ring. A similar behavior can be seen for $F_{\rm pol}$. Degree of polarization P decreases with increasing b as the amount of multiple scattered, generally low polarized, light, also increases with b.

This is also a good time to mention when the assumption of rings with homogeneous optical thicknesses breaks down. As long as the entire ring is illuminated and visible the assumption is valid, regardless of the orientation of the ring. The problem lies with the occultations and shadowing of both the ring onto the planet and vice versa. In the case of an inhomogeneous ring, the reflected or transmitted flux by the ring becomes dependent on the radius and an occultation of, or shadow cast on, part of the ring would therefore have more or less effect. The error the assumption introduces, considering two similar-sized rings, should be largest if the inner part of the ring is much thinner. In a follow-up study, these effects could be explored.

Looking at the curves for P, it is clear that the weakly polarized ring-light dilutes $F_{\rm pol}$ of the planet and thus decreases P of the planet-ring system. Between $\nu = 69.4°$ and $\nu = 249.4°$ when the ring-flux is small, this depolarizing effect is less prominent, especially for $b = 4.0$: the very small ring-flux hardly contributes to F while at the same time, the ring strongly shadows and occults the planet.

4.3. The influence of the single scattering albedo

Next, we vary the single scattering albedo ϖ of the ring particles to mimic different compositions. The icy particles surrounding Saturn would, for example, not survive at the distance between the Earth and the Sun. Considering the recent discoveries of puffed-up planets, of which the transit depth combined with their mass would indicate very small densities, that could possibly be explained by the presence of a ring (Piro & Vissapragada 2020) (as that could increase the transit depth), it is important to also look at refractory materials (which have a lower albedo in the visible) (Piironen et al. 1998; Ostrowski & Bryson 2019). Figure 9 shows F, $F_{\rm pol}$, and P for the standard planet-ring system and for ϖ ranging from 0.05 to 0.8.

Not surprisingly, increasing ϖ increases F, regardless of whether the ring is seen in reflected or transmitted light. Because for a given value of b, ϖ has no effect on the shadowing or occultation by the ring, and because the single scattering polarization of the particles is independent of ϖ, $F_{\rm pol}$ shows little dependence on ϖ, indirectly showing how small the contribution of the ring is to $F_{\rm pol}$. The variation in P is thus mostly due to the variation of F.

From comparing Figs. 7 and 9, we can conclude that for this planet-ring system, it appears to be difficult to distinguish whether a curve is due to a larger ring optical thickness or a higher albedo. Increases in either parameter lead to higher fluxes when the ring is reflecting light and a larger b can also increase the transmitted flux: a fit of a measured light curve could be made with some uncertainties in the optical thickness b and/or particle albedo ϖ. For a different orientation

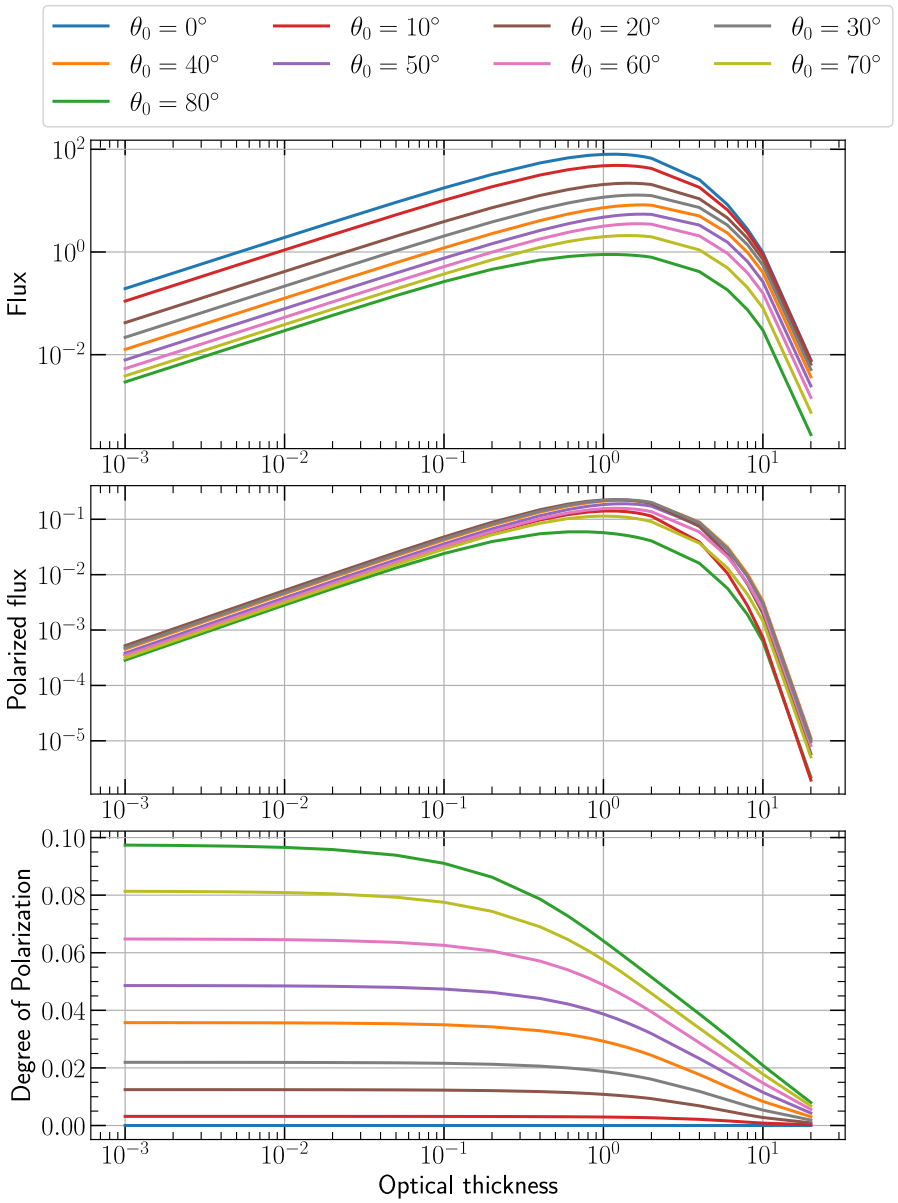

Fig. 8: The diffusely transmitted F (top), $F_{\rm pol}$ (middle), and P (bottom) as functions of the ring optical thickness b for illumination angles θ_0 ranging from 0° (blue) to 80° (green). The viewing angle θ is 0°.

of the ring and/or planetary orbit, this might be different, however, and that is something that a full retrieval algorithm could find out.

4.4. The influence of the ring radius

The influence of the outer ring radius $r_{\rm out}$ is shown in Fig. 10. The curves are very similar to the curves obtained by varying the optical thickness b (Fig. 7) since increasing $r_{\rm out}$ increases the reflected fluxes and, depending on the geometry, also the shadows in a similar way as increasing b. There are some key differences, however. For example, along parts of the orbit where the ring is transmitting light, the ring flux increases with increasing $r_{\rm out}$ while it would decrease with increasing b beyond a value of about 1.0 (see Fig. 11).

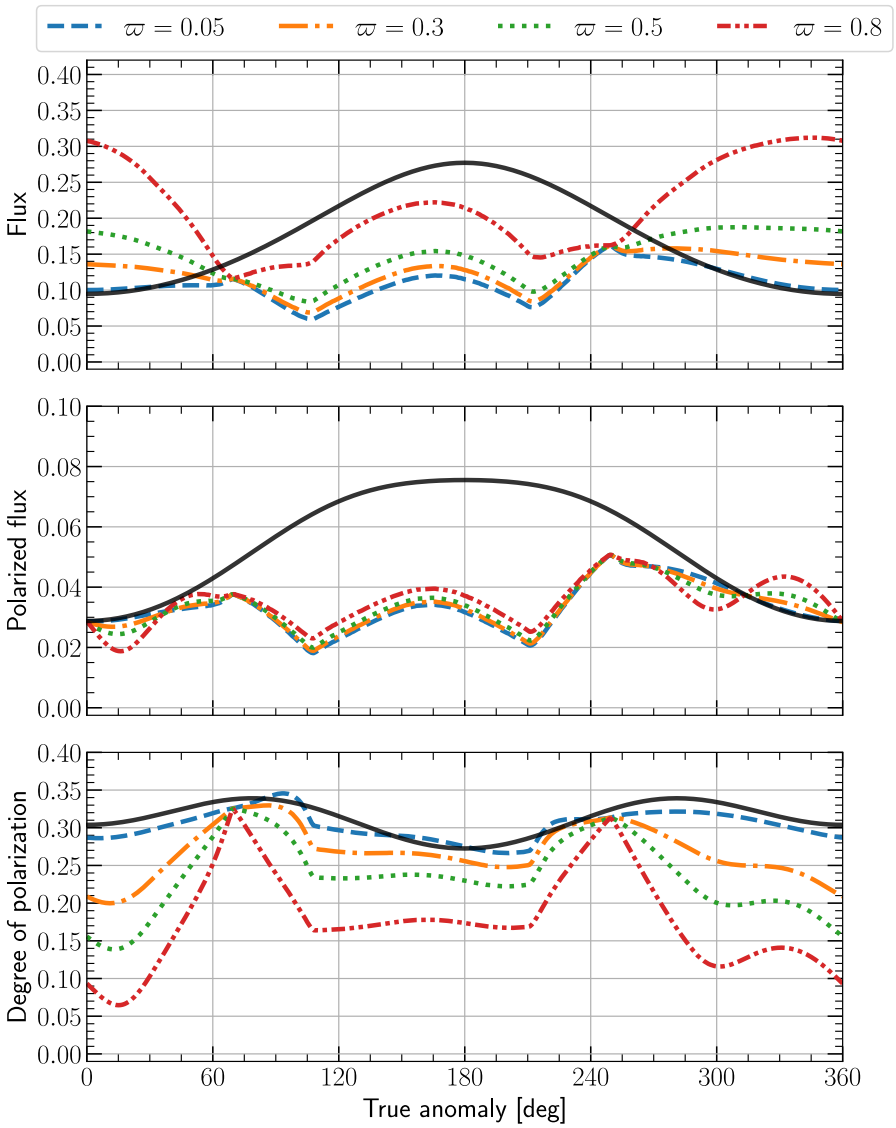

Fig. 9: F, $F_{\rm pol}$, and P as functions of ν for different single scattering albedos ϖ of the ring particles: 0.05 (blue, dashed), 0.3 (orange, dashed-dot-dot), 0.5 (green, dotted), and 0.8 (red, short-dashed-dotted). The system-parameters are $i = 20°$, $\lambda_{\rm r} = 30°$, $\gamma = 60°$, $r_{\rm in} = 1.2$, $r_{\rm out} = 2.25$, and $b = 1.0$. The black line represents the planet without a ring.

Another difference compared to changing b is found in the polarized flux curves. Whereas increasing b decreases $F_{\rm pol}$ because light that has been scattered multiple times is less polarized, there is no such relation with the ring size: the larger the ring, the larger the amount of $F_{\rm pol}$ that is added to the signal of the planet-ring system. With increasing $r_{\rm out}$, the curves for P converge as the polarization signal of the rings starts to dominate that of the planet, except close to the ring-plane crossing locations. This trend is helped by the fact that eventually, increasing $r_{\rm out}$ no longer increases the extent of the shadows on the planet.

The dips around $\nu = 15°$ and $\nu = 290°$ are interesting because they become more pronounced when the ring becomes brighter as is evident from Figs. 7, 9, and 10. What is happening here is that at these locations in the orbit, the scattering angle of the light that interacts with the ring is opposite to the angle of the light that interacts with the planet. They thus cancel out and decrease

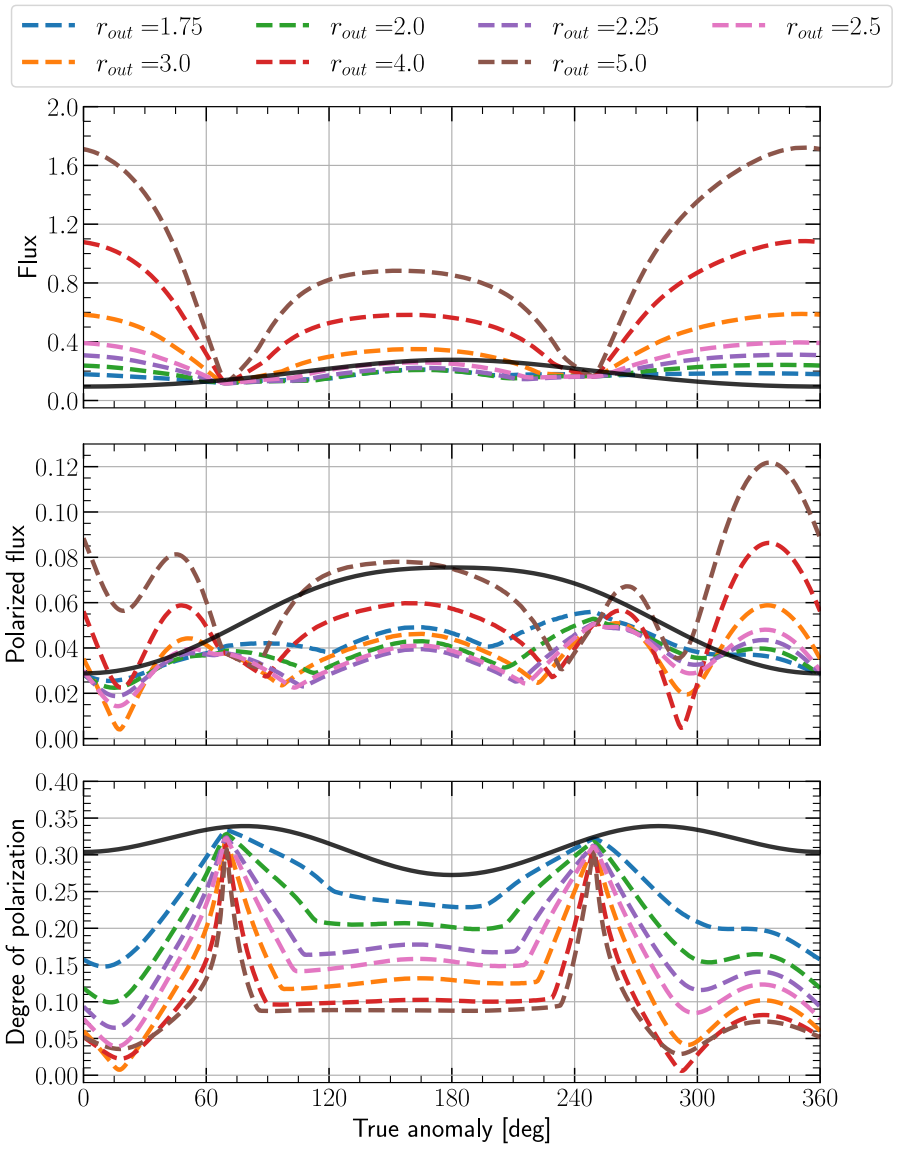

Fig. 10: F, $F_{\rm pol}$, and P as functions of ν for different values of the outer ring radius $r_{\rm out}$: 1.75 (blue, dashed), 2.0 (green, dashed), 2.25 (purple, dashed), 2.5 (pink, dashed), 3.0 (orange, dashed), 4.0 (red,dashed), and 5.0 (brown, dashed). The system-parameters are $i = 20°$, $\lambda_{\rm r} = 30°$, $\gamma = 60°$, $r_{\rm in} = 1.2$, $\varpi = 0.8$, and $b = 1.0$. The black line represents the planet without a ring.

P, which becomes more prominent when the ring flux is larger. For a ring size of $r_{\rm out} = 5.0$, the ring flux dominates the planetary flux and P no longer approaches zero.

4.5. A Case Study

As a case study, we simulate the signals of "puffed-up" planet HIP 41378 f (Akinsanmi et al. 2020b; Alam et al. 2022), assuming that instead of a single planet, this is actually a planet with a ring. It is suspected to have a ring because of the abnormally low planetary density of $\rho_{\rm p} = 0.09 \pm 0.02$ g cm^{-3} that a normal transit fit predicts. By including an opaque ring in the transit fit Akinsanmi et al. (2020b) finds an average density of $\rho_{\rm p} = 1.2 \pm 0.4$ g cm^{-3} instead. Other properties of this exoplanet that make it interesting to look at in this study are the following. The

Table 4: System parameters determined by Akinsanmi et al. (2020b), presented here without their uncertainty. The orientation of the ring is defined differently by Akinsanmi et al. (2020b) so our values for γ and λ_r are different than theirs but represent the same ring orientation.

Parameter	Value
R_p [$R_\oplus$]	3.7
a/R_*	231.0
i_p [°]	89.97
r_{in} [R_p]	1.05
r_{out} [R_p]	2.6
γ [°]	-2.11
λ_r [°]	-24.92

planet has a relatively large semi-major axis of roughly 1.4 AU that, at 103 pc, translates to a sky-projected angular separation of ∼13 mas (Santerne et al. 2019). This is large enough that the planet could be resolved by proposed direct imaging telescopes like the Large UV/Optical/Infrared Surveyor (LUVOIR) (The LUVOIR Team 2019). The planet is also cool (T_{eq} = 294 K), so there is no significant thermal emission that decreases the relevancy of the reflected light or the perceived P. And lastly, the transit has been observed as part of the K2 mission (Howell et al. 2014) which observed in similar wavelengths as the 633 nm that was used for the other results of this study.

A detailed fit of the transit using `Pryngles` is outside of the scope of this study so the results of this simulation should be seen as a demonstration of the capabilities of `Pryngles` and a rough indication of the detectability of the reflected light of this system. The system properties for a ringed planet that were determined by (Akinsanmi et al. 2020b) are repeated in Table 4 and will also be used here. In order to show the detectability of the reflected light, the two outermost values of the optical thickness and the single scattering albedo of the ring particles that are possible within the constraints of the values in Table 4, will be used to show four "extreme" situations. Especially the particle albedo is hardly constrained by the transit fit but, as was shown in Fig. 9, can have a big impact on the reflected flux. The two outer values of ϖ that were used to generate Fig. 9, 0.05 and 0.8, will also be used here, where it should be noted that a ϖ of 0.8 is high for particles that are presumed to be made of rocky materials considering the proximity of the planet to the star. Both papers, however, predict that the average density ρ of the ring particles is 1.08 ± 0.3 g cm^{-3} which is low compared to most rocky materials. This can be explained by porous materials (Carry 2012) but perhaps also due to the presence of ice that is continuously deposited by some unknown source. Regardless of the likeliness of icy particles, it is instructive to look at an upper limit which a ϖ of 0.8 represents.

Both studies assumed that the ring was completely opaque (Akinsanmi et al. 2020b; Alam et al. 2022) but this is not very realistic nor is it necessary for a similar transit depth. Above an optical thickness of 4, modeled transits (not shown here) show that the transit depth is fairly close to the one observed. Therefore, the lower bound is set at 4 and the upper bound is set at 20, which is high enough to be a completely opaque ring for all intents and purposes. Since the orientation and size of the ring are a much more direct result of the transit fit these things will not be varied. Again the olivine particles are used which are comparable in size to the particles that were used in the follow-

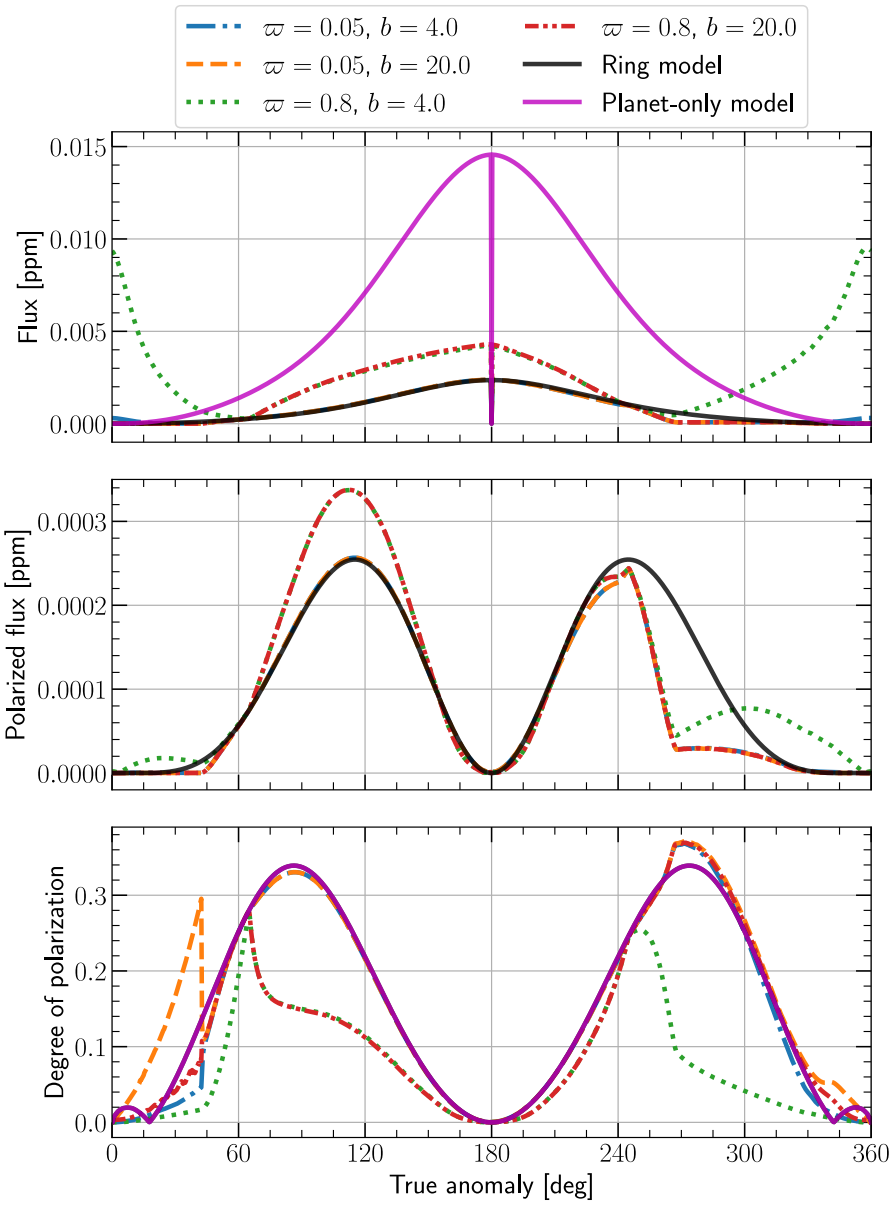

Fig. 11: F, $F_{\rm pol}$, and P of HIP 41378f for different values of b and ϖ as functions of ν. The magenta curves pertain to the planet when assuming it is "puffed up", and the black curves to the planet when assuming it has a ring, both based on values from Akinsanmi et al. (2020b). The magenta curve has been omitted from the $F_{\rm pol}$ plot for clarity: it has the same shape as the black curve, but with maximum values up to 0.0015 ppm. In the P-plot, the black and magenta curves overlap.

up study by (Alam et al. 2022). For simplicity, the same planetary atmosphere as in the previous results has been used. For the planet-ring model this should be fine but considering the low density that the planet in the planet-only model has, a simple, one-gas-type atmosphere is likely not the right approximation.

The results of the simulation are shown in Fig. 11. It shows that even in the most favorable case the contrast required to reliably observe the planet, in case it has rings, needs to be on the order of 10^{-9}. Such a contrast is currently not attainable with SPHERE/ZIMPOL (Thalmann et al. 2008) or JWST (Carter et al. 2022), especially at the small angular separation of 13 mas. If we assume that in the future the contrast and resolution that is needed can be achieved, we can start to say

something about the differences between the planet-only model and the planet-ring model. Note that the large spike in the curve of P before $\nu = 60°$ would not be observable due to the low flux at that point in the orbit.

If we take the curve for the planet-only model as unknown in exact brightness but having the presented shape, then it becomes clear that at least two measurements are necessary to reliably differentiate between the two models. Considering the angular separation is largest around $\nu = 90°$ and $\nu = 270°$ the focus should be on differences in that region. Luckily, this is also where the biggest differences are in both F and P. If there is a ring, a flux difference would be found when measuring at $\nu = 90°$ and $\nu = 270°$ which would not be the case for the presented planet-only model. This flux difference is there regardless of the optical thickness or single scattering albedo of the ring but could be absent or changed if the ring has a different orientation. If the polarization of the light is also measured, something could be said about the composition of the ring. For example, assuming that the ring is truly opaque, so $b = 20$, P at $\nu = 90°$ would be a function of ϖ and so could potentially be extracted. A thorough analysis of observations could extract both the optical thickness and albedo based on the difference in P at $\nu = 90°$ and $\nu = 270°$.

Based on these results it should be possible to distinguish between a planet with a simple atmosphere and a planet with a ring if they could be directly observed. If P is also measured it should even be possible to extract some of the properties of the ring. As was mentioned in Sect. 4.1 and by Dyudina et al. (2005), a planet that shows seasonal activities might also produce asymmetrical light curves. A follow-up study could investigate this possibility based on the proposed atmospheres by Alam et al. (2022). A third possible explanation comes from a recent study that shows that the observed transit can be explained by the presence of an exomoon (Harada et al. 2023). The reflected light of a planet with an exomoon could in theory also lead to a measured flux difference because the moon may move in front of the planet, or vice versa. The chance of this happening during an observation depends on the size and period of the moon as well as the observation frequency but should be small, as was shown by Berzosa Molina et al. (2018). Berzosa Molina et al. (2018) also showed that such transits (of the moon in front of the planet or vice versa) only result in shallow, brief dips in the light curve. The dips were especially small in the curves for P (around 2%) and so should be distinguishable from the effects of a ring.

5. Summary and Conclusions

We have looked at what effect a ring around an extrasolar planet has on the total reflected and polarized flux. To compute the light curves we improved the python package `Pryngles` by basing the radiative transfer calculations on an adding-doubling algorithm that includes all orders of scattering and polarization (de Haan et al. 1987). In most of our results we used dusty rings that are comprised of irregularly shaped particles with an effective radius of 1 μm. By varying different system parameters their effect on the light curves has been characterized. The system parameters that were varied are the ring orientation (see Sect. 4.1), the optical thickness of the ring (see Sect. 4.2),

the single scattering albedo of the ring particles (see Sect. 4.3), and the ring size (see Sect. 4.4. To put the work into context we finished by performing a simple case study of the HIP 41378 f planet in Sect. 4.5.

Based on the characterization we can identify a number of general signatures indicative of the presence of a ring. In general, the presence of a ring, that is not seen edge-on, causes the flux curve to display two peaks due to the difference in reflected and transmitted flux. This behavior was also reported in previous articles (Arnold & Schneider 2004; Dyudina et al. 2005). The inclusion of polarization in this study, however, allows us to expand upon this and show that the increase in flux due to the ring that caused the second peak has a substantially lower degree of polarization. The lower degree of polarization of the light reflected or transmitted by the ring comes from the difference between molecules and particles and is therefore almost always present. This dichotomy between higher flux but a lower degree of polarization is therefore a key signature of a ring and was also reported in a recent study by Lietzow & Wolf (2023). A notable exception to this would be a planet that shows large, seasonal activity, as was also reported by Dyudina et al. (2005). What sets the effect of rings apart from such a planet are the large changes in flux and degree of polarization around the ring-plane crossings, when the ring is illuminated edge-on. Therefore these sharp discontinuities would be something to look for in future observations. Lastly, due to the occultation of the ring in front of the planet or the shadow cast onto the planet, the received flux can be lower than expected, even when the ring is seen edge-on.

While each of the system parameters that were varied has distinct effects on the light curve we demonstrated that there is also a big overlap between them. Especially when it comes to the properties of the ring such as optical thickness, particle albedo, and size. Some of these properties, like the size of the ring and its optical thickness, also have an effect on the stability of the ring. So in order to draw a good conclusion, future observations should perform thorough fits of the parameter space to extract as much information as possible. Such a fit should include eccentric orbits, which is possible using `Pryngles`, and different planetary atmospheres as was done by Lietzow & Wolf (2023). The variation of the latter is interesting to combine with observations in different wavelength bands, in particular at wavelengths where gases in the planetary atmosphere absorb, and where the planet is thus dark, which could highlight the presence of rings and help to characterize them.

The case study showed that while it is currently not yet possible to directly observe such a system, it might be with the next generation of telescopes like LUVOIR (The LUVOIR Team 2019). We show that it would be beneficial for those instruments to use polarimetry as it allows for the identification of properties like the optical thickness and particle albedo of the ring, something not possible using only flux measurements.

We find that the presence of a ring introduces unique features in the reflected and polarized flux of a planet-ring system that depend on various ring properties. In order to identify rings, observations along the planetary orbit would be needed, in particular covering the ring-plane crossings,

where discontinuities in the signals could be detected. Combining total and polarized flux observations could help to characterize the physical properties of rings, which would allow us to better understand planet formation and the formation and evolution of the rings around the planets in our Solar System.

References

Akinsanmi, B., Barros, S. C. C., Santos, N. C., Oshagh, M., & Serrano, L. M. 2020a, MNRAS, 497, 3484

Akinsanmi, B., Santos, N. C., Faria, J. P., et al. 2020b, A&A, 635, L8

Alam, M. K., Kirk, J., Dressing, C. D., et al. 2022, ApJ, 927, L5

Arnold, L. & Schneider, J. 2004, A&A, 420, 1153

Barnes, J. W. & Fortney, J. J. 2003, ApJ, 588, 545

Barnes, J. W. & Fortney, J. J. 2004, ApJ, 616, 1193

Berzosa Molina, J., Rossi, L., & Stam, D. M. 2018, A&A, 618, A162

Buenzli, E. & Schmid, H. M. 2009, A&A, 504, 259

Cabrera, J. & Schneider, J. 2007, A&A, 464, 1133

Carry, B. 2012, Planet. Space Sci., 73, 98

Carter, A. L., Hinkley, S., Kammerer, J., et al. 2022, arXiv e-prints, arXiv:2208.14990

Charnoz, S., Canup, R. M., Crida, A., & Dones, L. 2018, in Planetary Ring Systems. Properties, Structure, and Evolution, ed. M. S. Tiscareno & C. D. Murray, 517–538

Cotton, D. V., Marshall, J. P., Bailey, J., et al. 2017, Monthly Notices of the Royal Astronomical Society, 467, 873

de Haan, J. F., Bosma, P. B., & Hovenier, J. W. 1987, A&A, 183, 371

de Rooij, W. A. & van der Stap, C. C. A. H. 1984, A&A, 131, 237

Deeg, H. J. & Alonso, R. 2018, in Handbook of Exoplanets, ed. H. J. Deeg & J. A. Belmonte, 117

Demory, B. O., Sulis, S., Meier Valdes, E., et al. 2022, arXiv e-prints, arXiv:2211.03582

Dollfus, A. 1984, in Planetary Rings, ed. A. Brahic, 121

Draine, B. T. & Flatau, P. J. 1994, Journal of the Optical Society of America A, 11, 1491

Draine, B. T. & Flatau, P. J. 2004, arXiv e-prints, astro

Dyudina, U. A., Sackett, P. D., Bayliss, D. D. R., et al. 2005, ApJ, 618, 973

Goloub, P., Herman, M., Chepfer, H., et al. 2000, J. Geophys. Res., 105, 14,747

Hansen, J. E. & Travis, L. D. 1974, Space Sci. Rev., 16, 527

Harada, C. K., Dressing, C. D., Alam, M. K., et al. 2023, arXiv e-prints, arXiv:2303.14294

Heller, R., Hippke, M., Placek, B., Angerhausen, D., & Agol, E. 2016, A&A, 591, A67

Heller, R. & Zuluaga, J. I. 2013, ApJ, 776, L33

Hovenier, J. W., Van Der Mee, C., & Domke, H. 2004, Transfer of polarized light in planetary atmospheres : basic concepts and practical methods, Vol. 318 (Springer Science & Business Media)

Howell, S. B., Sobeck, C., Haas, M., et al. 2014, PASP, 126, 398

Jakobsen, P., Ferruit, P., Alves de Oliveira, C., et al. 2022, A&A, 661, A80

Kane, S. R. & Gelino, D. M. 2010, ApJ, 724, 818

Karalidi, T., Stam, D. M., & Guirado, D. 2013, A&A, 555, A127

Karalidi, T., Stam, D. M., & Hovenier, J. W. 2012, A&A, 548, A90

Kemp, J. C., Henson, G. D., Steiner, C. T., & Powell, E. R. 1987, Nature, 326, 270

Kipping, D. M. 2009, MNRAS, 392, 181

Knutson, H. A., Charbonneau, D., Allen, L. E., et al. 2007, Nature, 447, 183

Lazarian, A. 2007, J. Quant. Spectr. Rad. Transf., 106, 225

Lietzow, M. & Wolf, S. 2023, arXiv e-prints, arXiv:2302.06508

Lissauer, J. J. & de Pater, I. 2019, Fundamental Planetary Science (updated edition) (Cambridge University Press)

Mishchenko, M. I. 2009, J. Quant. Spectr. Rad. Transf., 110, 808

Moreno, F., Vilaplana, R., Muñoz, O., Molina, A., & Guirado, D. 2006, J. Quant. Spectr. Rad. Transf., 100, 277

Morris, B. M., Delrez, L., Brandeker, A., et al. 2021, A&A, 653, A173

Muñoz, O., Volten, H., de Haan, J. F., Vassen, W., & Hovenier, J. W. 2000, A&A, 360, 777

Nousiainen, T., Zubko, E., Lindqvist, H., Kahnert, M., & Tyynelä, J. 2012, J. Quant. Spectr. Rad. Transf., 113, 2391

Ohno, K. & Fortney, J. J. 2022, ApJ, 930, 50

Ostrowski, D. & Bryson, K. 2019, Planet. Space Sci., 165, 148

Perryman, M. 2018, The Exoplanet Handbook

Piironen, J., Muinonen, K., Nousiainen, T., et al. 1998, Planet. Space Sci., 46, 937

Piro, A. L. & Vissapragada, S. 2020, AJ, 159, 131

Placek, B., Knuth, K. H., & Angerhausen, D. 2014, ApJ, 795, 112

Porco, C. C., Weiss, J. W., Richardson, D. C., et al. 2008, AJ, 136, 2172

Porco, C. C., West, R. A., Squyres, S., et al. 2004, Space Sci. Rev., 115, 363

Rieke, M. J., Kelly, D., & Horner, S. 2005, in Society of Photo-Optical Instrumentation Engineers (SPIE) Conference Series, Vol. 5904, Cryogenic Optical Systems and Instruments XI, ed. J. B. Heaney & L. G. Burriesci, 1–8

Rossi, L., Berzosa-Molina, J., & Stam, D. M. 2018, A&A, 616, A147

Rossi, L. & Stam, D. M. 2018, A&A, 616, A117

Santerne, A., Malavolta, L., Kosiarek, M. R., et al. 2019, arXiv e-prints, arXiv:1911.07355

Schmid, H. M., Bazzon, A., Roelfsema, R., et al. 2018, A&A, 619, A9

Seager, S. & Mallén-Ornelas, G. 2003, ApJ, 585, 1038

Simon, A., Szatmáry, K., & Szabó, G. M. 2007, A&A, 470, 727

Stam, D. M. & Hovenier, J. W. 2005, A&A, 444, 275

Stam, D. M., Hovenier, J. W., & Waters, L. B. F. M. 2004, A&A, 428, 663

Stolker, T., Min, M., Stam, D. M., et al. 2017, A&A, 607, A42

Sucerquia, M., Alvarado-Montes, J. A., Zuluaga, J. I., Montesinos, M., & Bayo, A. 2020, MNRAS, 496, L85

Tamburo, P., Mandell, A., Deming, D., & Garhart, E. 2018, AJ, 155, 221

Thalmann, C., Schmid, H. M., Boccaletti, A., et al. 2008, in Society of Photo-Optical Instrumentation Engineers (SPIE) Conference Series, Vol. 7014, Ground-based and Airborne Instrumentation for Astronomy II, ed. I. S. McLean & M. M. Casali, 70143F

The LUVOIR Team. 2019, arXiv e-prints, arXiv:1912.06219

Vogel, H. 1979, Mathematical Biosciences, 44, 179

West, R. 2022, *Personal communication*

Ye, S. Y., Gurnett, D. A., & Kurth, W. S. 2016, Icarus, 279, 51

Zuluaga, J. I., Kipping, D. M., Sucerquia, M., & Alvarado, J. A. 2015, ApJ, 803, L14

Zuluaga, J. I., Sucerquia, M., & Alvarado-Montes, J. A. 2022, Astronomy and Computing, 40, 100623

Appendix A: Computing $\phi - \phi_0$ and β

We describe here the calculations for $(\phi - \phi_0)$ and β in more detail. Starting with the azimuthal difference angle, and followed by the reference plane rotation angle β.

The azimuthal angles (ϕ and ϕ_0) can be defined with respect to any plane containing the local z-axis which makes the plane that also contains the observer an obvious choice since this eliminates one of the two angles that need to be calculated, namely ϕ. Thus an expression is needed for ϕ_0 which then automatically also becomes an expression for $\phi - \phi_0$. Using the spherical law of cosine an expression can be found for an intermediate angle we name δ which is used to find ϕ_0 with respect to the plane containing the direction to the observer and local z-axis,

$$\phi_{i,0} = \pi - \delta_i \,, \tag{A.1}$$

$$\delta_i = \arccos\left(\frac{\cos\alpha - \cos\theta_{i,0}\cos\theta_i}{\sin\theta_{i,0}\sin\theta_i}\right), \tag{A.2}$$

where the subscript i stands for the i^{th} spangle.

Care has to be taken, however, in making sure the angle that is found using the above equation is for a rotation that is clockwise when looking in the positive local zenith direction. Whether the found angle needs to be adjusted depends generally on the orientation of the spangle, be it planetary or ring, and the direction of the star-light. The dependency on the location of the star can be understood from Fig. A.1 where α will change during the orbit, eventually moving to the other side of the plane formed by $\hat{u}_i$ and $\hat{u}_{obs}$, the normal vector of the spangle and the normal vector

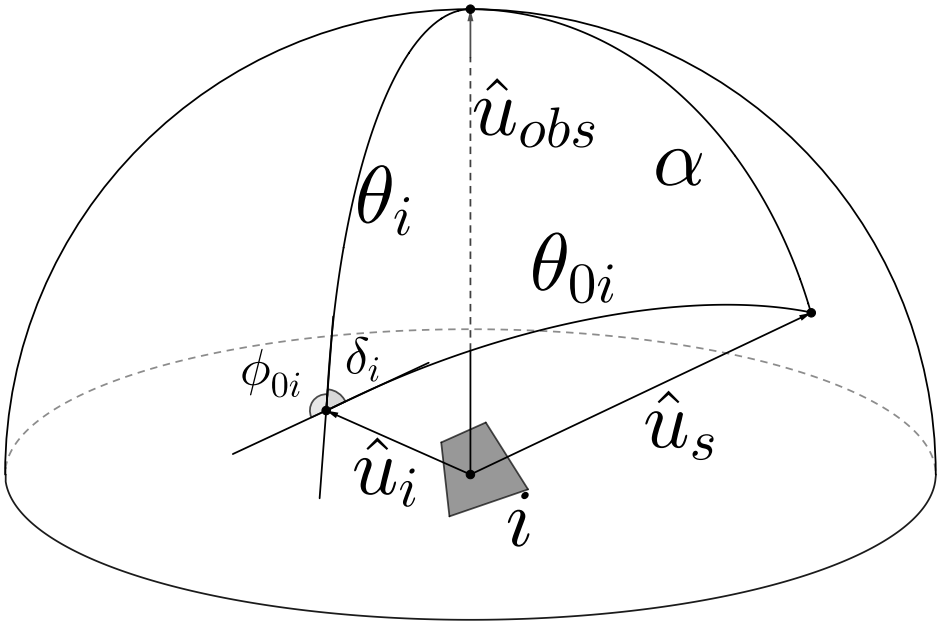

Fig. A.1: The angles and unit vectors associated with each individual spangle i. They are: the phase angle α, direction to observer $\hat{u}_{\rm obs}$, direction to the star $\hat{u}_{\rm s}$, normal vector $\hat{u}_i$, illumination angle $\theta_{i,0}$, viewing angle θ_i, azimuthal angle $\phi_{0,i}$, and intermediate angle δ_i. The rotation angle β_i is not shown here.

pointing to the observer respectively. For planetary spangles, the angles are modified as

$$(\phi_i - \phi_{i,0}) = \phi_{i,0} \,, \tag{A.3}$$

$$(\phi_i - \phi_{i,0}) = -\phi_{i,0} \,, \quad \text{if} \quad y_i^{scat} < 0 \,, \tag{A.4}$$

with y_i^{scat} the y-location of the spangle with respect to the planetary scattering plane. Where the criterion there is to compensate for the flipping of the normal vector for spangles on the "southern" hemisphere. The dependency on the location of the star is already incorporated into the y-location with respect to the planetary scattering plane.

Since all ring spangles have the same normal vector there is no dependency on their location on the ring. There is, however, a dependency on the orientation of the ring since it determines the locations in the orbit where the flip in the rotation direction happens. The locations of these flips are defined as the place where the plane containing the star, the planet, and the observer and the plane containing the normal vector of the ring and the observer are parallel. A 2D projection of the problem is shown in Fig. A.2 with the two vectors in the direction of the star $\hat{u}_{\text{star, (1,2)}}$ representing two moments in the orbit.

Two situations arise, depending on the orientation of the ring. If the normal vector of the ring $\hat{u}_{\text{ring}}$ is pointing in the ^{+}y direction,

$$(\phi_i - \phi_{i,0}) = -\phi_{i,0} \,, \tag{A.5}$$

when the vector pointing to the star $\hat{u}_{\text{star}}$ is on the ^{-}x side of the plane formed by $\hat{u}_{\text{ring}}$ and the observer. If $\hat{u}_{\text{ring}}$ is pointing in the ^{-}y direction,

$$(\phi_i - \phi_{i,0}) = -\phi_{i,0} \,, \tag{A.6}$$

when $\hat{u}_{\text{star}}$ is on the ^{+}x side of the plane formed by that same plane.

The angle between the local meridian plane and the detector plane, β, is also calculated differently for ring spangles compared to planetary spangles. For planetary spangles, the angle is only dependent on their location on the planet. With the detector plane as the reference plane, β is calculated as

$$x_i y_i \geq 0 : \beta_i = \arctan \frac{y_i}{x_i}, \tag{A.7}$$

$$x_i y_i < 0 : \beta_i = \pi + \arctan \frac{y_i}{x_i}, \tag{A.8}$$

where the coordinates (x_i, y_i) are in the observer reference frame. The addition of π is there to make sure the angle that is calculated rotates in the correct direction.

Because all ring spangles have the same normal vector the rotation angle does not depend on the location of the individual spangles. Using the spherical cosine law we can find an equation that

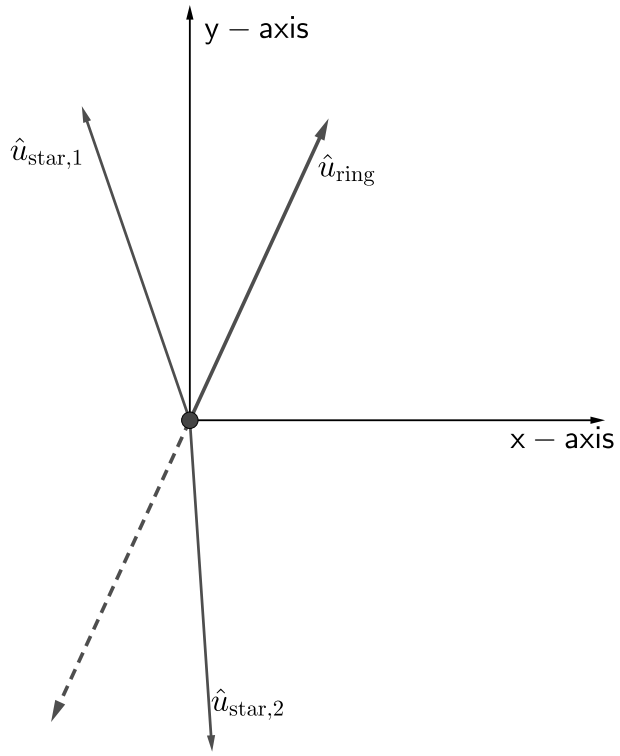

Fig. A.2: Illustration of the condition for changing the calculation of β, described in the text.

instead depends on the orientation of the ring

$$\beta = \arccos\left(\frac{\cos\sigma}{\sin\theta_i}\right), \tag{A.9}$$

$$\beta = \pi - \arccos\left(\frac{\cos\sigma}{\sin\theta_i}\right), \quad \text{if} \quad \hat{u}^{y}_{ring} < 0\,, \tag{A.10}$$

with $\sigma = \arctan2\left(\hat{u}^{z}_{ring}/\hat{u}^{x}_{ring}\right)$ the angle the normal vector makes with the x-axis and $\hat{u}^{z}_{ring}$ the z-component of the normal vector. Again the condition of $\hat{u}^{ring}_{y} < 0$ is added to make sure the rotation direction stays the same.

3
Additional Theory

This part of the thesis provides additional background on the theory already presented in the paper and adds some theory to topics that were used in the paper but for which no further explanation was given. It will start with a very broad description of light followed by a more physical description of it than was given in the paper. In this part, Sect. 3.1.1, some of the benefits of using Stokes parameters are proven and given a bit more background. The next section, Sect. 3.2, gives some more background on the phase matrix or scattering matrix as it was called in the paper. Sections 3.2.1 and 3.2.2 give a short explanation of two scattering mechanics that were used in the paper, Rayleigh scattering, and Mie scattering respectively. Lastly, Sect. 3.3 is about the two main particle distributions used when describing the scattering of light by particles.

3.1. Polarization of light

Light can be described as a wave. This wave can be scattered by molecules and particles. The atmosphere of Earth, for example, is blue due to molecules scattering the incident sunlight and clouds are white because the incident sunlight is scattered by the large cloud particles. Describing these phenomena mathematically is one of the oldest fields in physics. The theory for this section is taken from Hansen and Travis [79] and Hovenier et al. [80] unless stated differently.

The flux of electromagnetic radiation is defined as the rate of energy that flows across a unit area perpendicular to the direction of propagation. Because light is not a scalar wave, such as sound waves, the flux alone is not a full description. The transverse nature of the electromagnetic wave gives rise to polarization, a phenomenon where there is a preferred oscillation direction of the electric and magnetic fields for all waves. In general, each wave is monochromatic and completely elliptically polarized. Geometrically this means that the vector that represents the electrical field, at a fixed point in space, rotates around the vector representing the direction of travel. Two special cases of the ellipse are a straight line and a circle, corresponding to linear and circular polarization respectively.

Light is measured as the net effect of many waves, or photons, and is therefore generally partially polarized. For light that is completely polarized, all waves have identical polarization ellipses. Light coming from a star, when integrated over the stellar disk, is generally not polarized: all the waves have completely uncorrelated polarization ellipses, and measuring the light on any meaningful time scale would show no preferred direction of oscillation[11]. The flux of any arbitrary beam of light generally contains a polarized and unpolarized part

$$F = F_{\text{unpol}} + F_{\text{pol}}. \tag{3.1}$$

3.1.1. Exponential wave functions

Consider a parallel beam of light. In the plane perpendicular to the travel direction, two rectangular axes l and r can be chosen coming from a point O somewhere on the beam. The axes can also be represented as mutually perpendicular unit vectors $\boldsymbol{r}$ and $\boldsymbol{l}$. Assuming the beam travels in the positive z-direction, which is also defined as the direction of the vector product $\boldsymbol{r} \times \boldsymbol{l}$, the components of the electric field are described as

$$E_l(t) = a_l(t)e^{i(\omega t - kz - \epsilon_l(t))}, \tag{3.2}$$

$$E_r(t) = a_r(t)e^{i(\omega t - kz - \epsilon_r(t))}, \tag{3.3}$$

where t is time, $k = \frac{2\pi}{\lambda}$ the wavenumber with λ the wavelength, $a_l(t)$ and $a_r(t)$ are the amplitudes in the respective directions, $\epsilon_l(t)$ and $\epsilon_r(t)$ are the phases of the respective directions and ω is the circular frequency. In Fig. 3.1 an example of a polarization ellipse is shown. The angle χ is the angle between the semi-major axis of the ellipse and the l axis, rotated anti-clockwise when looking in the

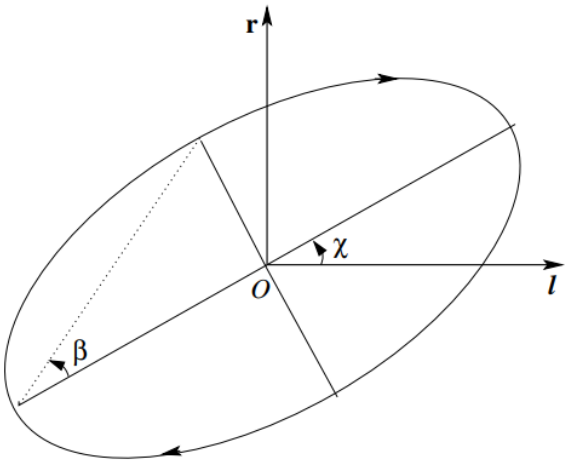

Figure 3.1: The polarization ellipse for the electric vector. The direction of propagation is into the paper. Taken from Hovenier et al. [80].

direction of propagation. The angle β is not the angle between reference planes as it was defined in the paper but rather a measure of the ellipticity. It is defined as

$$\tan 2\beta = \frac{V}{\sqrt{U^2 + Q^2V^2}}. \tag{3.4}$$

For linearly polarized light, as was the topic in the paper, $\beta = 0°$. From now on β will again be the angle between reference planes unless stated otherwise.

Assuming linearly polarized light χ defines the direction of the polarized flux with respect to the reference plane and is defined as

$$\tan 2\chi = \frac{U}{Q}, \tag{3.5}$$

with $0° \leq \chi < 180°$, and with its value chosen such that $\cos 2\chi$ has the same sign as Q.

This is also a good time to mention a different way of defining the degree of polarization that can add a bit more information. When $U = 0$, the light is either polarized perpendicular ($Q < 0,\ \chi = 90°$) or parallel ($Q > 0,\ \chi = 0°$) to the reference plane and the degree of polarization can be defined as

$$P = -\frac{Q}{F}, \tag{3.6}$$

so that $P < 0$ if the polarization is parallel and $P > 0$ when the polarization is perpendicular to the reference plane.

The Stokes parameters, as described in the paper, can also be expressed in terms of the electric field components as

$$F = \left\langle E_l E_l^* + E_r E_r^* \right\rangle = \left\langle a_l(t)^2 + a_r(t)^2 \right\rangle, \tag{3.7}$$
$$Q = \left\langle E_l E_l^* - E_r E_r^* \right\rangle = \left\langle a_l(t)^2 - a_r(t)^2 \right\rangle, \tag{3.8}$$
$$U = \left\langle E_l E_r^* + E_r E_l^* \right\rangle = 2\left\langle a_l(t) a_r(t) \cos\delta(t) \right\rangle, \tag{3.9}$$
$$V = i\left\langle E_l E_r^* - E_r E_l^* \right\rangle = 2\left\langle a_l(t) a_r(t) \sin\delta(t) \right\rangle, \tag{3.10}$$

where $\delta(t) = \epsilon_l(t) - \epsilon_r(t)$, the brackets $\langle\rangle$ mean that the time average is taken and the asterisk represents the complex conjugate. A common factor is omitted from the right-hand sides of Eqs. (3.7–3.10) since Stokes parameters are often only used in a relative sense, comparing them only to other Stokes parameters from the same beam or another beam. The physical definition of the Stokes parameters can be deduced from

$$\Phi(\psi, \epsilon) = \frac{1}{2}\left[F + Q\cos 2\psi + (U\cos\epsilon + V\sin\epsilon)\sin 2\psi\right], \tag{3.11}$$

where $\Phi(\psi, \epsilon)$ is the flux one would measure through a linear polarisation filter with its optical axis making an angle ψ with the $\boldsymbol{l}$ direction and ϵ is the constant retardation of E_r with respect to E_l[79]. Using Eq. 3.11 it can be derived how the different Stokes parameters could be measured using a rotating polarization filter, namely

$$F = \Phi(0°, 0) + \Phi(90°, 0) = F_l + F_r, \tag{3.12}$$

$$Q = \Phi(0°, 0) - \Phi(90°, 0) = F_l - F_r, \tag{3.13}$$

$$U = \Phi(45°, 0) - \Phi(135°, 0), \tag{3.14}$$

$$V = \Phi(45°, \pi/2) - \Phi(135°, \pi/2). \tag{3.15}$$

Equations (3.12–3.15) show that F is the total flux of light received, Q is the excess of flux having linear polarization in the $\boldsymbol{l}$ direction over flux that has linear polarization in the $\boldsymbol{r}$ direction, U is analogous to Q but in the directions $\psi = 45°$ and $\psi = 135°$, and V is the excess of right-handed circular polarization over left-handed circular polarization. Polarization is right-handed if, for an observer looking in the direction of propagation, the electric vector moves in the clockwise direction.

In the case of a monochromatic beam of light a_l, a_r, and δ are independent of time and the time averaging is no longer needed. In this case it follows from Eqs. (3.7–3.10) that

$$F = \sqrt{Q^2 + U^2 + V^2}, \tag{3.16}$$

which corresponds to completely polarized light. In general, however, light is only partially polarized and the equation turns into an inequality

$$F \geq \sqrt{Q^2 + U^2 + V^2}. \tag{3.17}$$

As already mentioned in the paper, the Stokes parameters are often described by the column vector $\boldsymbol{F}$ as

$$\boldsymbol{F} = [F, Q, U, V], \tag{3.18}$$

with again F the total flux, Q and U the linearly polarised fluxes and V the circular polarized flux. Previously, it was stated that light can be split into polarized and unpolarized parts. This important property can be proven using the above expression of the Stokes parameters. From Eq. 3.17 a possible expression for the unpolarized part of the light is found to be

$$\boldsymbol{F}_{unpol} = [F - (Q^2 + U^2 + V^2)^{1/2}, 0, 0, 0] \tag{3.19}$$

while the expression for the completely polarized part of the light is

$$\boldsymbol{F}_{pol} = [(Q^2 + U^2 + V^2)^{1/2}, Q, U, V] \,. \tag{3.20}$$

Bringing these equations together, the equality

$$\boldsymbol{F} = \boldsymbol{F}_{unpol} + \boldsymbol{F}_{pol} \quad , \tag{3.21}$$

is indeed found.

3.2. Scattering

The scattering of light, when described using Stokes vectors, can be expressed in its most basic form as a series of matrix multiplications [54] [80]

$$\boldsymbol{F}'(\lambda, \Theta) = \boldsymbol{L}(\beta)\boldsymbol{P}(\lambda, \Theta)\boldsymbol{L}(-\beta)\boldsymbol{F}(\lambda, \Theta), \tag{3.22}$$

with $\boldsymbol{F}'(\lambda, \Theta)$ the Stokes vector after scattering, $\boldsymbol{L}(-\beta)$ the rotation matrix to rotate from the reference plane to the scattering plane, $\boldsymbol{L}(\beta)$ to rotate back to the reference plane, and $\boldsymbol{P}(\lambda, \Theta)$ the phase matrix (in the paper called ”the scattering matrix”) which is a function of the particle composition, particle shape,

particle size, particle orientation, the wavelength λ and the scattering angle Θ which is 0 for forward scattering. The scattering plane is formed by the propagation direction of the incoming light and the azimuthal direction in which the particle scatters the light. The phase matrix, in its most general form, is a 4 x 4 Mueller matrix

$$\boldsymbol{P}(\lambda,\Theta)=\frac{\sigma_{scat}}{4\pi R^2}\begin{bmatrix}P_{11} & P_{12} & P_{13} & P_{14}\\ P_{21} & P_{22} & P_{23} & P_{24}\\ P_{31} & P_{32} & P_{33} & P_{34}\\ P_{41} & P_{42} & P_{43} & P_{44}\end{bmatrix}, \tag{3.23}$$

where σ_{scat} is the scattering cross-section of the particle, R is the distance to the particle and the elements of the matrix are functions of the (confusingly called) scattering matrix $\boldsymbol{S}(\Theta,\phi)$ with ϕ the azimuthal scattering angle of the particle with respect to the incident radiation.

The scattering matrix describes how the electric field of the incident light changed after the scattering

$$\begin{pmatrix}E_l\\ E_r\end{pmatrix}=\frac{e^{ik(z-R)}}{ikR}\boldsymbol{S}(\Theta,\phi)\begin{pmatrix}E_l^0\\ E_r^0\end{pmatrix} \tag{3.24}$$

with E_l^0 and E_r^0 the electric field components before the scattering and $\boldsymbol{S}(\Theta,\phi)$ a 2x2 matrix defined as

$$\boldsymbol{S}(\Theta,\phi)=\begin{bmatrix}S_2(\Theta,\phi) & S_3(\Theta,\phi)\\ S_4(\Theta,\phi) & S_1(\Theta,\phi)\end{bmatrix}. \tag{3.25}$$

The general form of the phase matrix has 16 unique elements making it computationally expensive to work with. Luckily, multiple special cases based on symmetry arguments have been found to reduce the number of independent parameters. These cases are frequently used because they are more easily solvable and also represent common physical phenomena. The three cases that allow for the number of independent elements of the phase matrix to be reduced are:

1. Perfectly spherical particles.
2. Randomly oriented particles, each with a plane of symmetry.
3. Randomly oriented asymmetric particles, if half the particles are mirror images of the other half.
4. Particles that are small compared to the wavelength.

If particles fall into any of the above, the phase matrix can be reduced to a matrix containing 6 independent parameters

$$\boldsymbol{P}(\lambda,\Theta)=\frac{\sigma_{scat}}{4\pi R^2}\begin{bmatrix}P_{11} & P_{21} & 0 & 0\\ P_{21} & P_{22} & 0 & 0\\ 0 & 0 & P_{33} & P_{43}\\ 0 & 0 & -P_{43} & P_{44}\end{bmatrix}. \tag{3.26}$$

Two well-known cases that fall into the categories described above are Rayleigh scattering and Mie scattering. Both of which will be expanded upon in the next two sections.

3.2.1. Rayleigh scattering

Rayleigh scattering happens when the size of the particle is less than the wavelength of the incident radiation and smaller than the wavelength inside the particle. It mainly happens in atmospheres or gas clouds so it is important when modeling the light reflected by an extrasolar planet with an atmosphere. The scattering matrix for very small particles is given by Hovenier et al. [80] as

$$\boldsymbol{S}(\Theta)=ik^3\alpha\begin{bmatrix}\cos\Theta & 0\\ 0 & 1\end{bmatrix}, \tag{3.27}$$

with α the polarizability of the particle which is assumed to be isotropic. The polarizability of a material is the tendency of said material to form a dipole moment when subjected to an electric field. If the

polarizability is assumed to be isotropic it is defined as the ratio between the induced dipole p and the electric field E that is inducing said dipole

$$\boldsymbol{p} = \alpha \boldsymbol{E}. \tag{3.28}$$

The phase matrix corresponding to the scattering matrix shown in Eq. 3.27 is given by Hovenier et al. [80] as

$$\boldsymbol{P}(\Theta) = \frac{\sigma_{scat}}{4\pi R^2} \begin{bmatrix} 1+\cos^2\Theta & \cos^2\Theta - 1 & 0 & 0 \\ \cos^2\Theta - 1 & 1+\cos^2\Theta & 0 & 0 \\ 0 & 0 & 2\cos\Theta & 0 \\ 0 & 0 & 0 & 2\cos\Theta \end{bmatrix}. \tag{3.29}$$

In general, however, particles do not have truly isotropic polarizability and α becomes a 3x3 tensor describing the ratios for every combination of scattering directions. For anisotropic particles in a random orientation, the phase matrix is given by Hansen and Travis [79] as

$$\boldsymbol{R}(\Theta) = \frac{\sigma_{scat}}{4\pi R^2} \left(\Delta \begin{bmatrix} 1+\cos^2\Theta & \cos^2\Theta - 1 & 0 & 0 \\ \cos^2\Theta - 1 & 1+\cos^2\Theta & 0 & 0 \\ 0 & 0 & 2\cos\Theta & 0 \\ 0 & 0 & 0 & 2\Delta'\cos\Theta \end{bmatrix} + (1-\Delta) \begin{bmatrix} 1 & 0 & 0 & 0 \\ 0 & 0 & 0 & 0 \\ 0 & 0 & 0 & 0 \\ 0 & 0 & 0 & 0 \end{bmatrix} \right). \tag{3.30}$$

where

$$\Delta = \frac{1-\delta}{1+\delta/2}, \tag{3.31}$$

$$\Delta = \frac{1-2\delta}{1-\delta}, \tag{3.32}$$

with δ defined as the depolarization factor which is the ratio of intensities parallel and perpendicular to the plane of scattering, F_l/F_r, for light scattered at $\Theta = 90°$ with unpolarized incident light. Isotropic Rayleigh scatterers have $\delta = 0$ while in general scatterers have $0 \leq \delta \leq 1/2$.

The only thing left to fully describe Rayleigh scattering is the scattering cross-section of the particles which is given by [54][81]

$$\sigma_{scat} = \frac{24\pi^3}{N^2\lambda^4} \left(\frac{n^2-1}{n^2+2} \right)^2 \frac{6+3\delta}{6-7\delta}, \tag{3.33}$$

with N the number of molecules per unit volume and n the real part of the refractive index. Because the refractive index of a gas is often close to one and so $n^2 + n \approx 3$, the above equation is sometimes also written as

$$\sigma_{scat} = \frac{8\pi^3}{3} \frac{(n^2-1)^2}{N^2\lambda^4} \frac{6+3\delta}{6-7\delta}. \tag{3.34}$$

For a detailed derivation of the scattering cross-section for Rayleigh scattering the book by Liou [81] provides a comprehensive explanation.

A good example of Rayleigh scattering is a phenomenon that is observable (almost) every day: the blue sky. Because the molecules in the air are small enough compared to the wavelength of the incident sunlight, they behave as Rayleigh scatterers. Rayleigh scattering is dependent on the wavelength of the incoming radiation as λ^{-4} (see 3.34), meaning that shorter wavelengths, i.e. blue light, get scattered more.

3.2.2. Mie scattering

Mie scattering describes the scattering of light by homogeneous spheres and stems from the solution of Maxwell's equations for spheres, named after Gustav Mie. For these particles, the scattering matrix is given by

$$\boldsymbol{S}(\Theta) = \begin{bmatrix} S_1(\Theta) & 0 \\ 0 & S_2(\Theta) \end{bmatrix}, \tag{3.35}$$

where

$$S_1(\Theta) = \sum_{n=1}^{\infty} \frac{2n+1}{n(n+1)} \left[a_n \pi_n(\cos\Theta) + b_n \tau_n(\cos\Theta)\right], \tag{3.36}$$

$$S_2(\Theta) = \sum_{n=1}^{\infty} \frac{2n+1}{n(n+1)} \left[b_n \pi_n(\cos\Theta) + a_n \tau_n(\cos\Theta)\right], \tag{3.37}$$

and

$$\pi_n(\cos\Theta) = \frac{dP_n(\cos\Theta)}{d\cos\Theta}, \tag{3.38}$$

$$\tau_n(\cos\Theta) = \cos\Theta\ \pi_n(\cos\Theta) - \sin^2\Theta\ \frac{d\pi_n(\cos\Theta)}{d\cos\Theta}, \tag{3.39}$$

with $P_n(\cos\Theta)$ a Legendre polynomial and a_n and b_n coefficients that depend on the complex refractive index $n_c = n_r - in_i$ and the size parameter x of the sphere

$$x = kr = \frac{2\pi r}{\lambda} \tag{3.40}$$

with r the radius of the sphere, k the wavenumber as defined in Eq. 3.2, and λ the wavelength. The relation between the scattering matrix and the elements of the phase matrix, as given by Eq. 3.26 is

$$P_{11} = \frac{2\pi R^2}{\sigma_{scat}}(S_1 S_1^* + S_2 S_2^*), \tag{3.41}$$

$$P_{21} = \frac{2\pi R^2}{\sigma_{scat}}(S_1 S_1^* - S_2 S_2^*), \tag{3.42}$$

$$P_{22} = P_{11}, \tag{3.43}$$

$$P_{33} = \frac{2\pi R^2}{\sigma_{scat}}(S_1 S_2^* + S_2 S_1^*), \tag{3.44}$$

$$P_{43} = i\frac{2\pi R^2}{\sigma_{scat}}(S_1 S_2^* - S_2 S_1^*), \tag{3.45}$$

$$P_{44} = P_{33}. \tag{3.46}$$

Computing a_n and b_n is crucial in determining the phase matrix and thus the scattering behavior of spheres. A full treatment of how to compute these coefficients is beyond this report but is well described in Hovenier et al. [80] and Mishchenko [82]. Numerical methods to calculate the coefficients can be found in Dave [83] and Kattawar and Plass [84].

3.3. Particle size distributions

For particles too large to fall into the Rayleigh-scattering criterion their size becomes an important property. Naturally occurring particles do not all have the same size but instead follow a size distribution $n(r)$. This particle size distribution is used to modify the phase matrix to simulate the phase matrix of a unit volume with particles. When modifying the phase matrix, each element becomes

$$P_{ij}(\Theta) = \int_{r_1}^{r_2} P_{ij}(\Theta, r) n(r) dr\ , \tag{3.47}$$

where $P_{ij}(\Theta)$ now describes the interaction with a unit volume instead of a single particle and it is assumed that the size distribution is normalized.

A standard and often used size distribution is given by Hansen [85]

$$n(r) = Cr^{(1-3v_{eff})/v_{eff}} e^{-r/(r_{eff} v_{eff})}, \tag{3.48}$$

where C is a proportionality constant, r_{eff} is the effective radius of the particles and v_{eff} is the effective variance of the size distribution which are defined as

$$r_{eff} = \frac{\int_{r_1}^{r_2} r\pi r^2 n(r)\, dr}{\int_{r_1}^{r_2} \pi r^2 n(r)\, dr}, \tag{3.49}$$

$$v_{eff} = \frac{1}{r_{eff}^2} \frac{\int_{r_1}^{r_2} (r - r_{eff})^2 \pi r^2 n(r)\, dr}{\int_{r_1}^{r_2} \pi r^2 n(r)\, dr} \tag{3.50}$$

respectively. This distribution is a variation of a gamma distribution and is often used to describe particles in planetary atmospheres [54, 79].

Particles in rings, like those around Saturn, are assumed to have a different size distribution which is best approximated by a power law [2, 86, 87]

$$\frac{dn}{dr} \propto r^{-\mu}. \tag{3.51}$$

This is the outcome of an ideal collisional cascade and is, for example, also observed in the mass distribution of asteroids [88]. The size distribution for a system following a power-law is defined by setting a minimum and maximum particle size and is dependent on the value of the power-law index μ. Rewriting to put the size distribution in the same form as Eq. 3.48 gives

$$n(r) = n_0 \left(\frac{r}{r_0}\right)^{-\mu}, \quad r_{min} \leq r \leq r_{max}, \tag{3.52}$$

with n_0 the number of particles at reference radius r_0.

4

Additional results

In this chapter, some results that were generated but that were not relevant to the paper are presented. They are included because they represent interesting behavior that is worth sharing and further showcase the versatility of the model that was developed. The topics are a bit unconnected so each section will have its own short introduction and discussion and conclusion section. In Sect. 4.1 the planetary atmosphere that was used in the paper and all other computations, unless stated otherwise, is described. To include this in the paper would have been a bit much but some interesting conclusions about the scattering of light can still be drawn from the results. Following that, Sect. 4.2 tries to answer the third research question: *Can a transit fit predict the flux and degree of polarization curves along the rest of the orbit?*. To do this the light curve of the well-known system J1407 is computed based on data gathered from numerous papers. The computed light curve will serve as an upper limit for unpublished data, courtesy of Matthew Kenworthy.

4.1. Different planetary atmospheres

Before any of the computations that were done for the paper on different ring orientations and compositions, a suitable model for the planet had to be chosen. To not complicate the results, a simple atmosphere that consisted of only gas and that was made up of a single layer would suffice. That still left a choice in the optical thickness of the atmosphere and the surface albedo of the planet.

In Fig. 4.1 the flux, polarized flux $\sqrt{Q^2 + U^2}$ and degree of polarization are shown for a planet with an orbital inclination i of $60°$ with different surface albedos and optical thicknesses. As expected, all configurations have their maximum flux at a true anomaly ν of $180°$, when the phase angle is smallest. The difference in reflected flux because of different optical thicknesses is also most apparent at this point. A smaller optical thickness means more light reaches the surface which explains why the flux is smaller for smaller optical thicknesses as long as the surface albedo is not zero. Increasing the surface albedo causes a slight increase in the reflected flux if the optical thickness is small enough. When the atmosphere has an optical depth of 80 the flux curves show almost no dependency on the surface albedo. The absolute difference between a surface albedo of 0.0 and 0.5 is approximately 2×10^{-4}. At this optical depth, the light that reaches the surface, and gets reflected back, is negligible and the atmosphere is almost completely opaque. Increasing the surface albedo to 1.0 causes all the curves to overlap as this effectively makes the optical thickness arbitrarily high.

Perhaps the most interesting result is that the polarized flux curves all overlap, even though there is a difference in total flux. This can be explained by the fact, that beyond a certain optical thickness, increasing the optical thickness only increases the flux from light that has been scattered multiple times. Multiply scattered light is only weakly polarized [7] and the majority of polarized flux comes from singly scattered light which has already reached its maximum contribution at the optical thicknesses considered. Zooming in on the results, which is done in Fig. 4.2, the small increases in polarized flux can be made visible. The values that are shown, are the increase in polarized flux compared to the curve with an optical thickness of 10. The surface albedo does not add any polarized flux so the differences are purely due to the optical thickness differences. While there are differences, they are so small that they are completely irrelevant for any detection. That multiply scattered light is only weakly polarized can also be deduced from the degree of polarization curves, which show a decrease with increasing optical thickness.

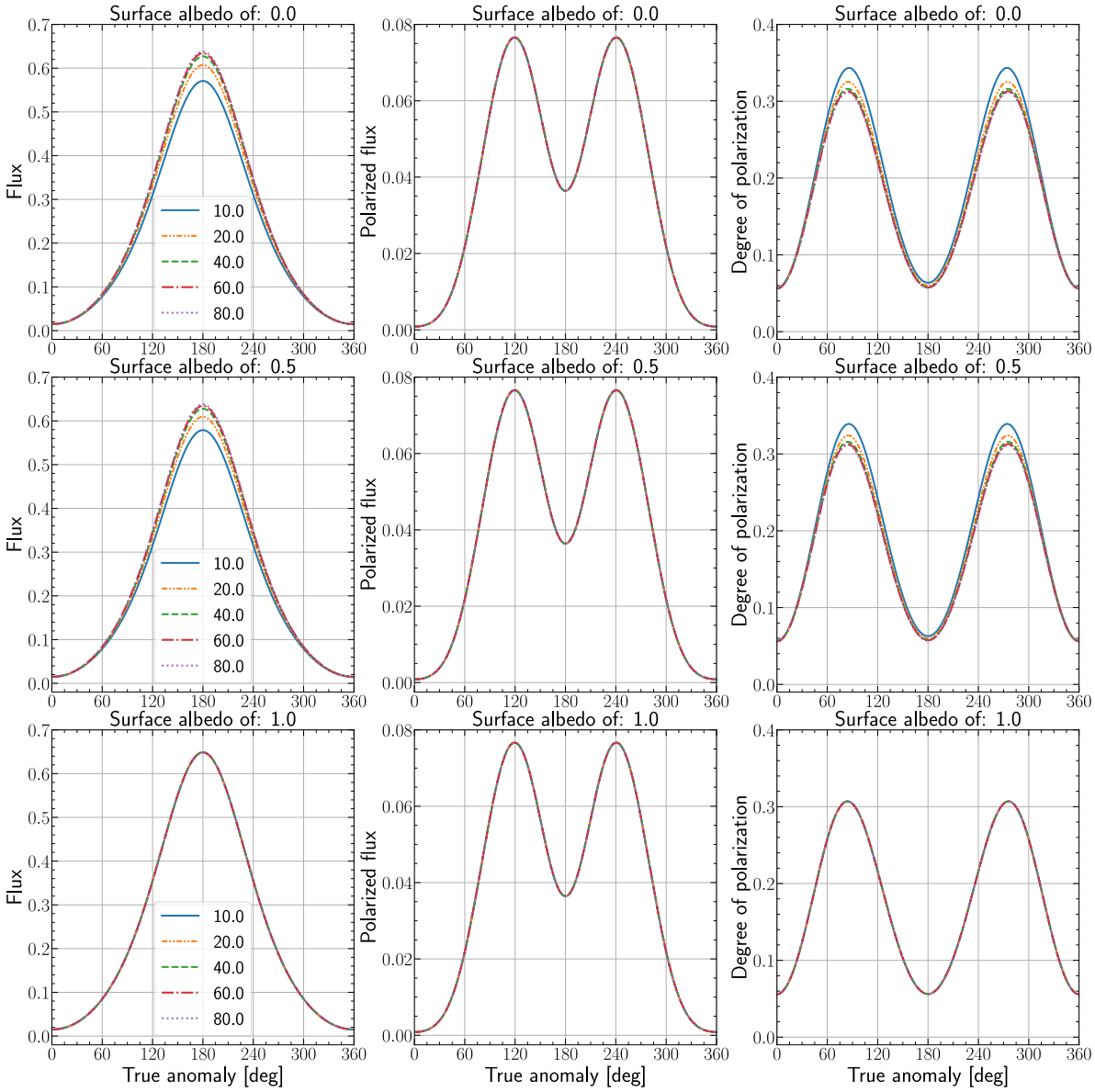

Figure 4.1: The reflected total flux F (left), the polarized flux $\sqrt{Q^2 + U^2}$ (middle), and the degree of polarization P (right) of a planet with an orbital inclination i of $60°$ for different planetary surface albedos, increasing from top to bottom from 0 to 1, and various optical thicknesses of the atmosphere: $b_{atmos} = 10, 20, 40, 50,$ and 80.

4.1.1. Summary and discussion

Based on the results presented here it was decided that the atmosphere of the planet should have a small optical thickness to make it stand out from a completely opaque planet. An optical thickness of 10, paired with a surface albedo of 0.5 was chosen as the planet to be used in the simulations presented in the paper. The surface albedo of 0.5 can represent the presence of a deep cloud layer when averaged over the entire sphere of the planet. The chosen planet can best be described as the least boring option out of multiple boring options. It is clear that without adding any real clouds or other absorbing gasses, like CH_4 the reflection of a planet is pretty featureless. This is fine for demonstrating the effect that rings have on the light curve but for a follow-up study of rings around exoplanets, it might be interesting to add methane or clouds to the planet to increase the realism and make the signal of the planet more wavelength dependent. Some examples of studies demonstrating the effect that clouds or the presence of other absorbing gases in the atmosphere have on the flux and polarization curves are Stam et al. [7], Karalidi et al. [66, 70], Rossi et al. [89].

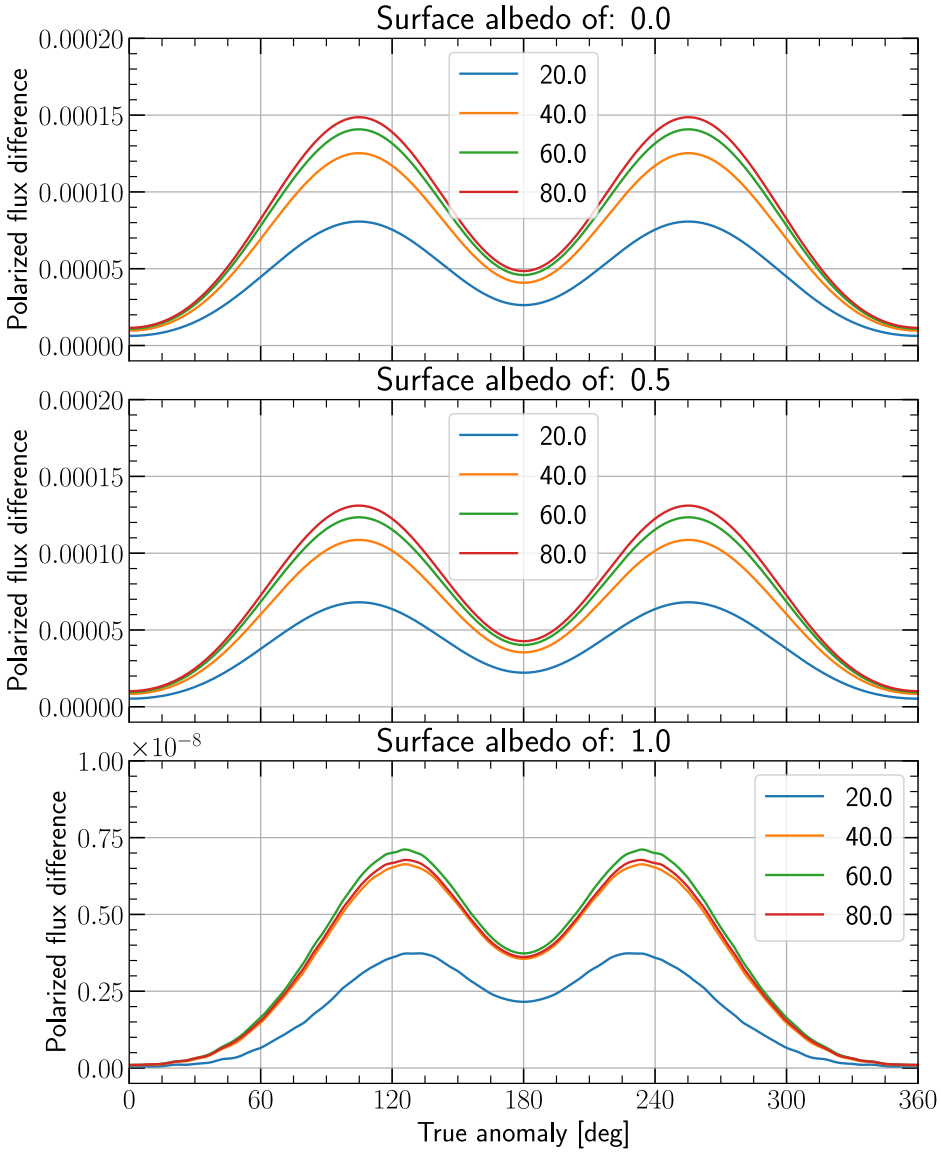

Figure 4.2: The absolute difference in polarized flux compared to a planet with an optical thickness of 10 for different surface albedos. The system has the same parameters as the one shown in Fig. 4.1. Note the scale on the y-axis for a surface albedo of 1.

4.2. Predicting the flux and polarization signal of J1407b

One of the research questions that was posed in the introduction is about modeling the light curve of a ringed-planet candidate based on information that has been gained from a fit of its transit. Perhaps the most (in)famous example of a possible ringed-planet candidate is J1407b, as was also mentioned in the introduction. There has already been a lot of analysis of the transit (see e.g. Kenworthy and Mamajek [35], Mamajek et al. [37]) and the dynamics of the system (see e.g. Rieder and Kenworthy [51], Sutton et al. [90]). Since no new transit has been observed and given the existing amount of research, there is little scientific gain from fitting the transit again using `Pryngles`.

Given the novelty of `Pryngles`, computing the reflected light would still be interesting, although it will not be the first time that the reflected (or transmitted) light of the system will be modeled [53]. The previously published model, however, was focused on creating an upper limit for measurements done using the ALMA radio telescope so computing the reflected light at 633 nm, including the degree of polarization, is new. A distinction between published and unpublished was made because, through contact with Dr. M. Kenworthy, I learned that there has been an observation campaign of J1407 using the SPHERE/ZIMPOL instrument but that the data was never published. As mentioned in the introduction, ZIMPOL is capable of measuring the degree of polarization of light that is reflected by exoplanets, which makes the use of `Pryngles` even more relevant. The observations showed no signal so computing the reflected light would serve as an upper limit to the expected signal and confirm, or disprove, the non-detection. Such an upper-limit study was also performed by van Dam et al. [91] (the unpublished paper) by computing the light reflected by a simple model of the disk. The disk was modeled using MCMax [92] and they varied the grain size of the particles in the disk between 0.1, 1.0, and 10 microns, each for different distances from the star expressed as angular separations of 30 up to 80 milliarcseconds (mas) in steps of 10 mas [91]. The model that was used had some shortcomings, however, which could be improved upon. Some of the shortcomings were: The use of a single grain size instead of a size distribution, not varying the orientation of the ring system with respect to the star, and not varying the optical thickness of the ring. It was also unclear what orientation the ring had that they used; what shape the particles had or what they were made of. Some of these things will, hopefully, be improved in the following analysis.

4.2.1. Parameter Sweep

To better understand the effect that different properties of the ring and orbit have on the reflected light a parameter sweep is done. The parameters that will be varied are the eccentricity of the orbit, the optical thickness of the ring, and the particle type/size. The range of these parameters needs to be realistic and so their values are taken from the numerous papers written about J1407b, they are displayed in Table 4.1. These choices, however, need some explanation before the results of the simulation will be shown as some of the values are quite uncertain.

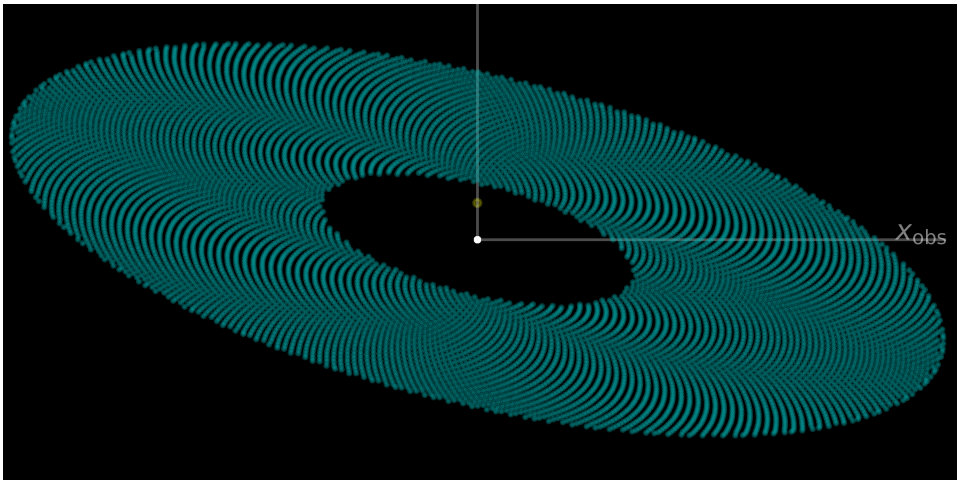

Figure 4.3: The modeled system, shown here with an eccentricity of 0.4 and at a true anomaly of 0°. The yellow dot is the star and the white dot is the planet.

Table 4.1: The model parameters that were used for the parameter sweep. The values were taken from different studies (but not the unpublished study [91]) where necessary. Values that have – as the source are either derived from other values or chosen.

Parameter	Value	Source
M_{J1407}	$1.0\ M_{\odot}$	[51, 90]
d	139 pc	[53]
i	[89.1°, 88.8°, 88.3°, 87.3°,84.8°]	–
M_{J1407b}	$20\ M_{\mathrm{Jupiter}}$	[35, 90]
R_{J1407b}	$1.5\ R_{\mathrm{Jupiter}}$	–
a	5 AU	[52, 93]
e	[0.4,0.5,0.6,0.7,0.8]	[35, 51, 90]
r_{in}	0.2 AU	[35]
r_{out}	0.6 AU	[35]
γ	$65.8°$	[35]
λ_r	$33.43°$	[35]
b	[0.1, 0.6, 1.0, 1.4]	–
ϖ	0.3	–
Particle	Olivine dust ($r_{\mathrm{eff}} = 1\ \mu m$ [94]) & perfect spheres ($r_{\mathrm{eff}} = 5\ \mu m$)	[53]

In this study, it is assumed that the object that caused the transit light curve is on a bound orbit around its star J1407 (so it will be called J1407b) and that the point where it transits is at the orbit's pericenter. The latter is needed to account for the highest observed transit velocity of 32.2 kms^{-1} [52]. As this is meant as an upper limit test the semi-major axis a is initially kept fixed at 5 AU to account for the shortest possible orbital period of approximately 11 years [93]. A smaller semi-major axis means a higher reflected flux. The eccentricity e is varied to show the effect of different separations and also because the eccentricity is a topic of contention, with different papers finding different values [51, 90]. The assumed eccentricity is always quite high though ($e > 0.4$) which makes the pericenter distance quite small (around 1 AU). This, paired with the large size of the ring, makes the assumption of uni-directional light problematic. To fix this, the `Pryngles` code was adjusted such that spangles can have their own illumination angle. The assumption that the star is a point source still remains, however. A more detailed description of the solution and the study surrounding it can be found in Sect. A.1 (where it is described as the "simple" solution). The orbital inclination i was varied because the impact parameter obtained from the fit of the transit, done by Kenworthy and Mamajek [35], was dependent on the transit velocity. As the eccentricity changes with a fixed semi-major axis the distance to the star as well as the speed at the pericenter will also change. Due to the way the transit velocity was measured, based on the rate of change of the flux, there were multiple observed transit velocities. Thus changing the speed does not immediately discredit the model (it was also done in previous articles [51, 90]).

The mass of J1407b is still debated and the value chosen here is a bit of a guess. Luckily, it does not directly influence the data as the orbits are not simulated but it does have an effect on the possible size of the planet. The value for R_{J1407b} is a bit arbitrary but lies in the range of possible sizes for a small brown-dwarf [95] or a gas giant and is also close to the values of $1.3R_{Jupiter}$ and $1.46R_{Jupiter}$ that have been used before by Kenworthy et al. [53] and Mamajek et al. [37] respectively. The ring size and orientation are based on the fit of the transit made by Kenworthy and Mamajek [35]. The optical thickness of the ring is based on the values found for different parts of the ring in that same fit. A ring with a homogenous optical thickness is used for simplicity and again to represent an upper limit. Considering the age of the system, estimated to be around 21 Myr [93], and the potentially close approach of around 1 AU, pure icy particles are unlikely. Instead, a mixture of ice and refractory material is approximated by giving the particles an albedo ϖ of 0.3. Lastly, the particles are chosen to demonstrate the difference in particle size, as well as the difference between irregular particles and perfect spheres. This latter is also done as a demonstration of the problems with using perfect spheres

as was mentioned already in the paper (see Sect. 2). It should be noted that due to the sharp forward scattering peak that these larger spherical particles have, the interpolation method had to be changed to a bilinear interpolator instead of the bicubic spline interpolator that was used for the results presented in the paper (see Sect. 2) to avoid interpolation artifacts such as overshoots. Tests, not shown here, have proven that the bilinear interpolator does not introduce significant errors but in the future, a more well-rounded interpolation algorithm should be found/used. To better understand the supposed size of J1407b and show the orientation of the ring, Fig. 4.3 shows the system at a true anomaly of $0°$. On visual inspection, it appears to be the same as the one that was displayed in Kenworthy and Mamajek [35].

4.2.2. Results of the parameter sweep

The flux, polarized flux, and degree of polarization curves generated in the parameter sweep using olivine dust particles are shown in Fig. 4.4 and those using spherical particles in Fig. 4.5. Contrary to the results shown in the paper (see Sect. 2), the presented fluxes are given in terms of the difference in magnitude Δm compared to the stellar magnitude. This is a logarithmic scale defined as

$$\Delta m = -2.5 \log_{10} \left(\frac{F_{\mathrm{J1407b}}}{F_{\mathrm{star}}} \right) \tag{4.1}$$

where lower values correspond to higher fluxes. These units were chosen because they were also used in the unpublished article which made comparisons easier. Since the point is to say something about the upper limit of detectability the discussion of the results will only be brief and will only focus on some of the key features.

The most striking features of the flux, polarized flux, and degree of polarization curves are probably the sharp peaks that occur at around 125° and $305°$ in all three. These are the ring-plane crossings, where the ring is lit edge-on, and they show just how little light the planet reflects in comparison to the giant ring. The light reflected by the ring is only lightly polarized, something that is evident from the sharp peaks in the degree of polarization plots that are caused by the planet-only signal. Unexpectedly, varying the orbital eccentricity (from top to bottom) appears to move the location of the ring-plane crossings a tiny bit. What is happening is that the orbital inclination changes due to the eccentricity which in turn moves the ring-plane crossings. Changing the eccentricity scales the reflected and transmitted flux because of the changes in the distance to the star. There is also a large difference in the amount of reflected light going from an optical thickness of 0.1 to >0.6 which initially looks wrong but can be explained by looking at Fig. 4.6. In this figure, the reflected flux is shown as a function of the optical thickness for different illumination angles. Looking at the flux curve, there is a large decrease for $b = 0.1$ compared to the other optical thicknesses, regardless of the illumination angle, which explains the behavior observed in Fig. 4.4 and Fig. 4.5.

On a side note, the graphs shown in Fig. 4.6 also show some interesting behavior that is worth explaining, but slightly off-topic. The behavior is only visible when the degree of polarization is defined using Eq. 3.6. Each curve in the degree of polarization graph in Fig. 4.6 starts with either $Q > 0$ or $Q < 0$ depending on the scattering angle. This is again made visible in Fig. 4.7 that shows the angle of the polarization χ and Q itself. At what scattering angle the sign of Q changes is a direct result of the single scattering behavior of the particles, as shown in Fig. 3 in the paper. Single scattering is not the only source of polarized light though and as the optical thickness increases, multiple scattering of light begins to also add some polarized light. This light is polarized less strongly and is polarized perpendicular to the scattering plane. Knowing this, the sign change of P that is observed for $\theta_0 = 30°$ is easily explained as the polarized flux due to multiple scattering overpowering the single scattering polarized flux that is parallel polarized. The same thing happens for $\theta_0 = 10°$ and $\theta_0 = 20°$ but the effect is less extreme, as can be seen in the polarized flux plot of Fig. 4.6 and in the Q plot of Fig. 4.7.

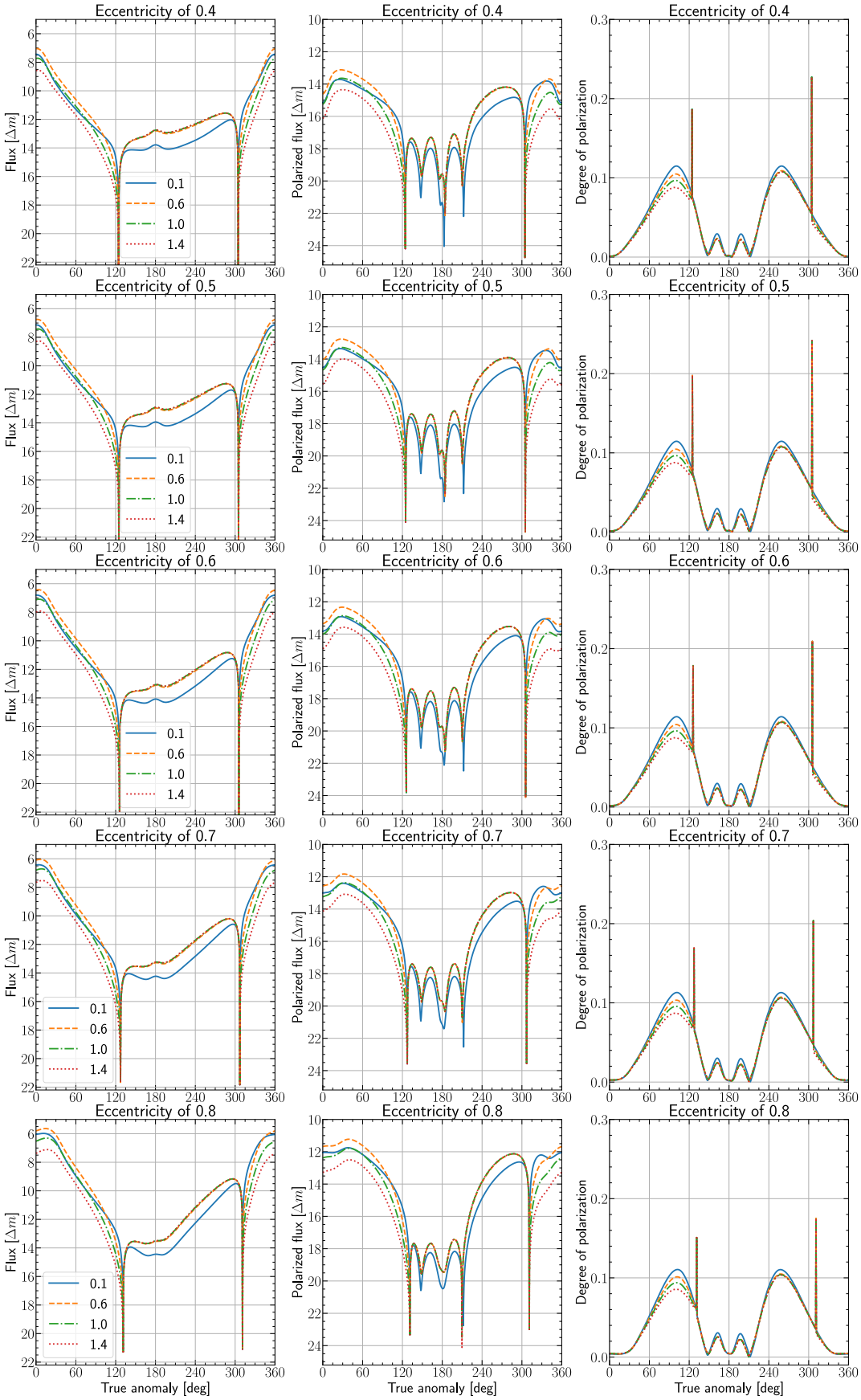

Figure 4.4: The reflected total flux F (left), the polarized flux $\sqrt{Q^2 + U^2}$ (middle), and the degree of polarization P (right) of the circumplanetary disk around J1407b for different ring optical thicknesses and orbital eccentricities. Modeled at a wavelength of 633 nm. The disk is made up of the same olivine dusty particles as in the article 2, with an albedo of 0.3.

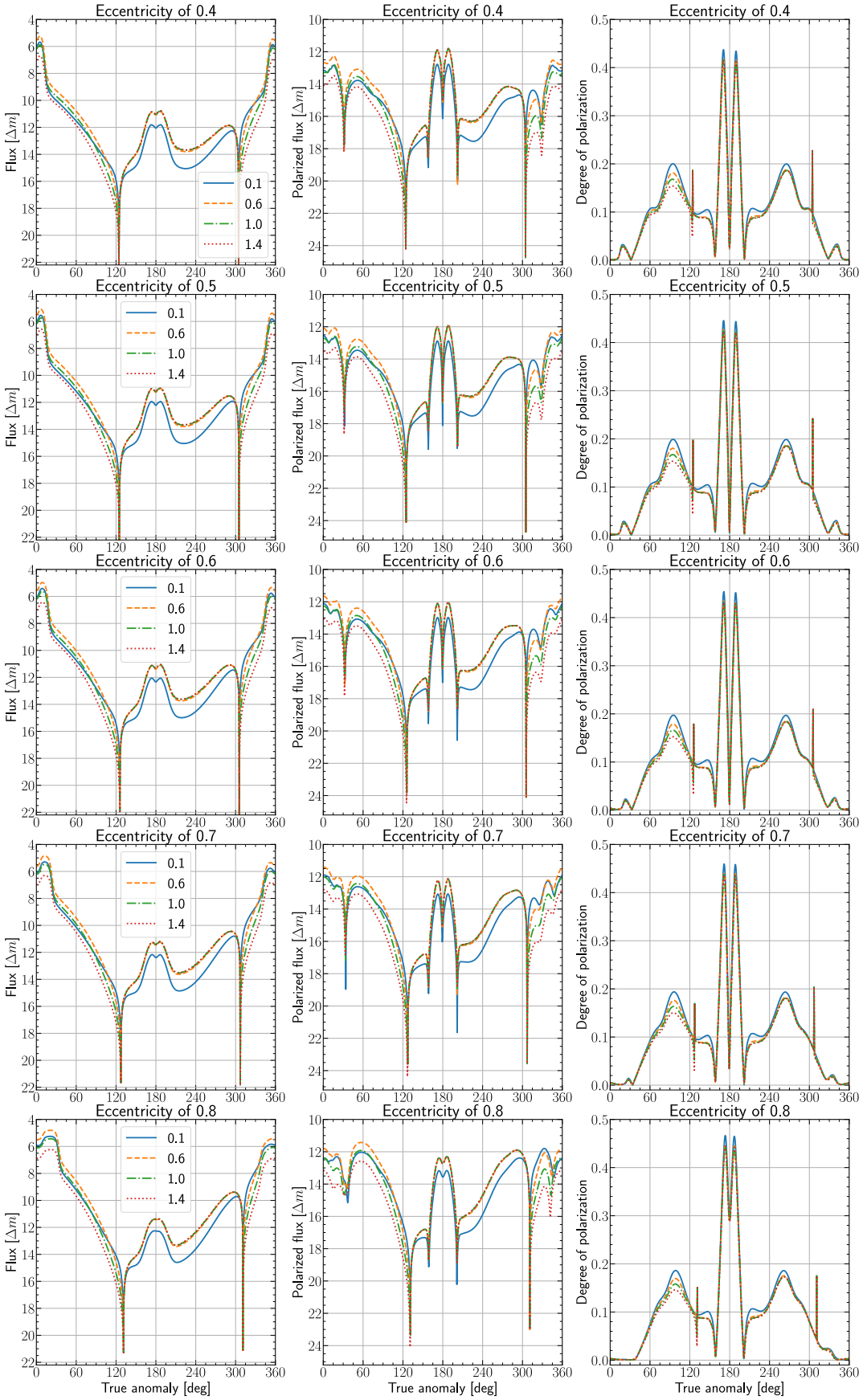

Figure 4.5: Similar to Fig. 4.4 but with a disk that contains spherical particles with a refractive index of 1.6, a radius of 5 μm, with the ring modeled at a wavelength of 1000 nm, and the planet at 633 nm. The difference in wavelength between the ring and the planet is small enough, and the flux of the planet is insignificant enough that this should not be a problem.

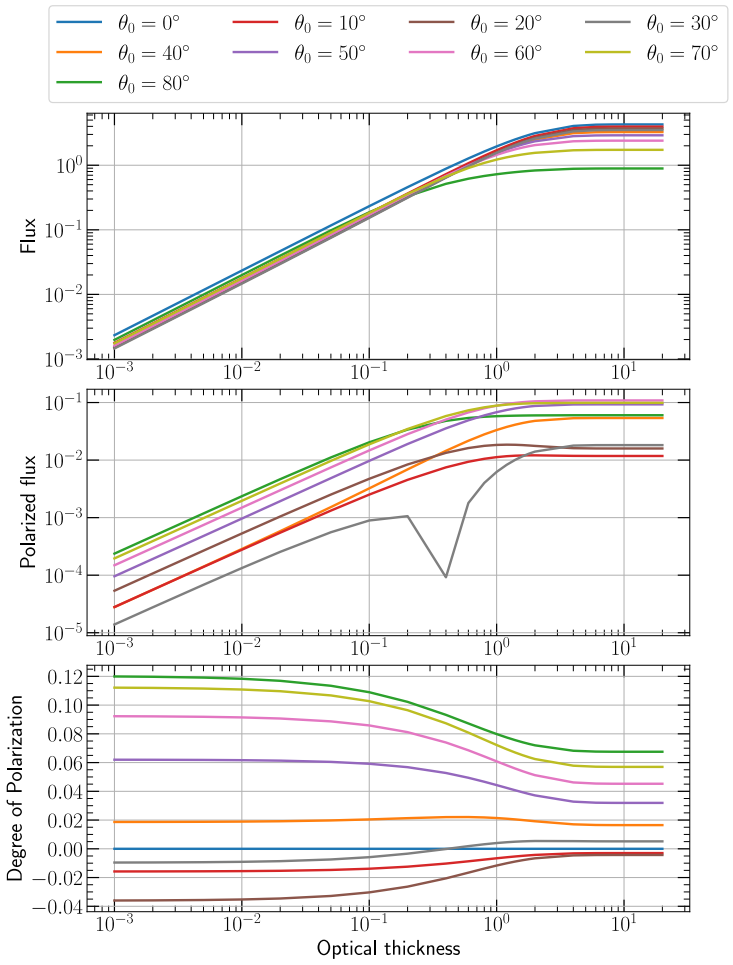

Figure 4.6: The diffusely reflected flux, polarized flux, and degree of polarization as a function of the optical thickness for various illumination angles θ_0. The viewing angle is constant and set to $0°$.

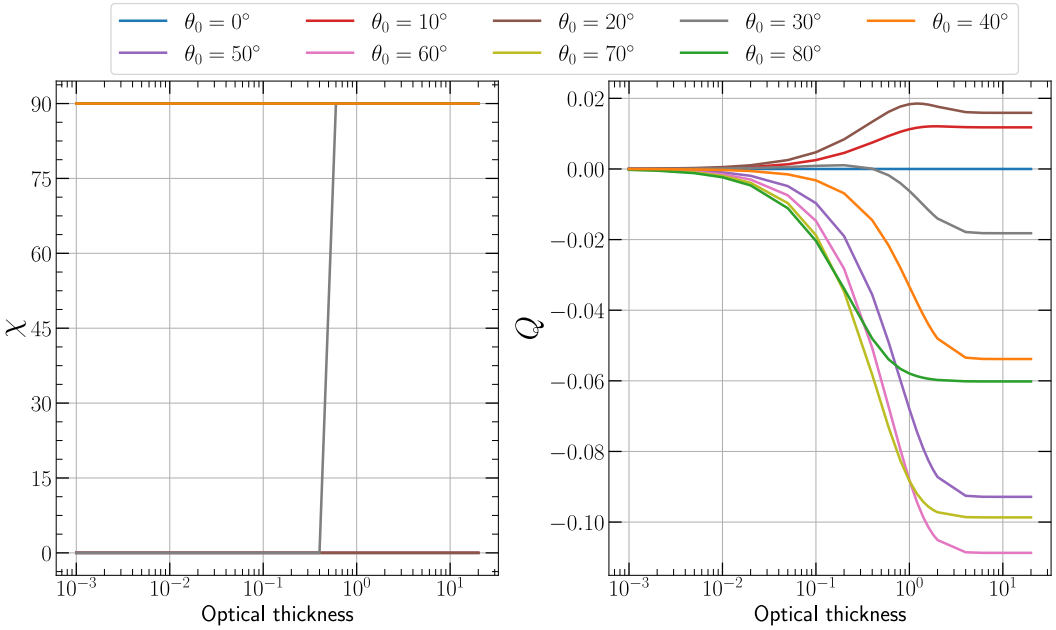

Figure 4.7: The graph on the left shows the scattering angle χ and the graph on the right is the linearly polarized flux Q, both as a function of the optical thickness and for various illumination angles θ_0 similarly to Fig. 4.6.

Coming back to Fig. 4.4 and Fig. 4.5 it is interesting to look at the differences between using irregular particles and perfect spheres (Mie-scattering) as the latter is often used when modeling reflected light. There are some known artifacts when using Mie-scattering, however, like rainbow and glory effects that cause high degrees of polarization. The rainbow effect is also clearly visible in the graphs as the large spikes around a true anomaly of $180°$. Another clear effect of using Mie-scattering is the lower back-scattering flux compared to the olivine particles. Besides the peak, at around a true anomaly of $180°$, the back-scattered light using Mie-scattering is consistently lower than when irregular particles are used. This is in part also due to a larger particle size which lowers the back-scattering but increases the forward-scattering peak. Particles that are found in the rings in the solar system are not perfectly spherical and there is no indication that this is not a general property of ring particles. Using the Mie-scattering results to set an upper limit on the degree of polarization is therefore not very realistic. Mie-scattering can, however, be accurate in predicting the forward scattering peak, as that is mostly a function of particle size [96, 97]. So the results for the initial and final part of the orbit could be used to set an upper limit on the particle size.

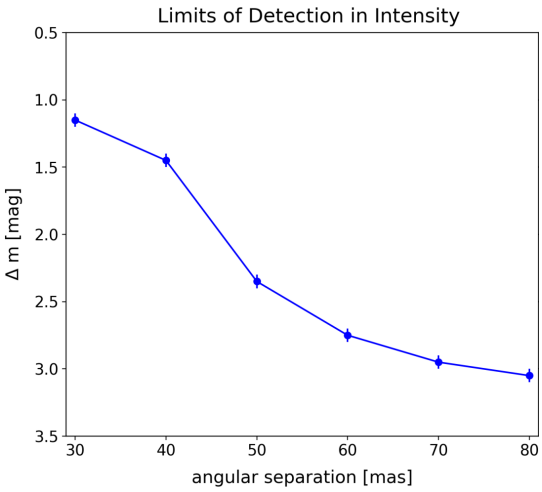

Figure 4.8: Adapted from Fig. 6 from van Dam et al. [91]. Their calculated detection limit in Δm for the intensity is given as a function of angular separation in milliarcseconds mas.

The highest fluxes occur when the rings are transmitting light, which was expected given the orbit geometry and the results from the paper. When the flux is highest, however, the planet and ring are also at a point in the orbit where the angular separation is the smallest. This means it won't be easy to directly observe the planet at that point. In both Fig. 4.4 and Fig. 4.5, the forward scattering peak reaches a Δm of around 6, which equals a reflected flux to stellar flux ratio of about 0.4%. While an increase like that should be possible to detect, no notion of such an increase in the observations could be found in any published papers. The star is also quite young so an increase in flux could have been attributed to stellar activity given that only a single transit has been observed. The computed transmitted light thus does not yet constrain any of the parameters.

To set an upper limit for the reflected flux it is perhaps more important to do this at the point in the orbit where the angular separation is maximum. There are two points in the orbit where this occurs but because the light curve is not symmetrical the flux is different at each point. The two points of maximum angular separation lie between a true anomaly of $110°$ and $150°$ and between $210°$ and $250°$, depending on the eccentricity. For example, when the eccentricity is 0.4 the maximum occurs at a true anomaly of $110°$ and $250°$. The upper limit, as a function of the angular separation, was set by van Dam et al. [91] and is shown in Fig. 4.8. At an angular separation of 30 mas, the detection limit, expressed in Δm, is roughly 1.2. Considering that the maximum angular separation in Fig. 4.4 and Fig. 4.5 lies between 22 and 33 mas (depending on the eccentricity) and that the reflected flux has a Δm of around 12 at that point (regardless of the eccentricity), it can be concluded that purely the reflected flux would be well below the detection limit. The detection limit becomes better with a larger angular separation but the reflected flux would also decrease with distance so this is still not good enough to detect the reflected light. It is good to keep in mind that the system that was simulated was an almost best-case scenario in terms of the reflected flux because of the lowest possible semi-major axis of 5 AU [93] and small particle size (in the case of the olivine particles). The latter statement can be drawn from the results shown in Fig. 4.9. If J1407b were to emit thermal radiation it could be brighter, regardless of the distance to its star, which was also assumed by van Dam et al. [91] but in terms of reflected flux it seems correct that they did not detect anything.

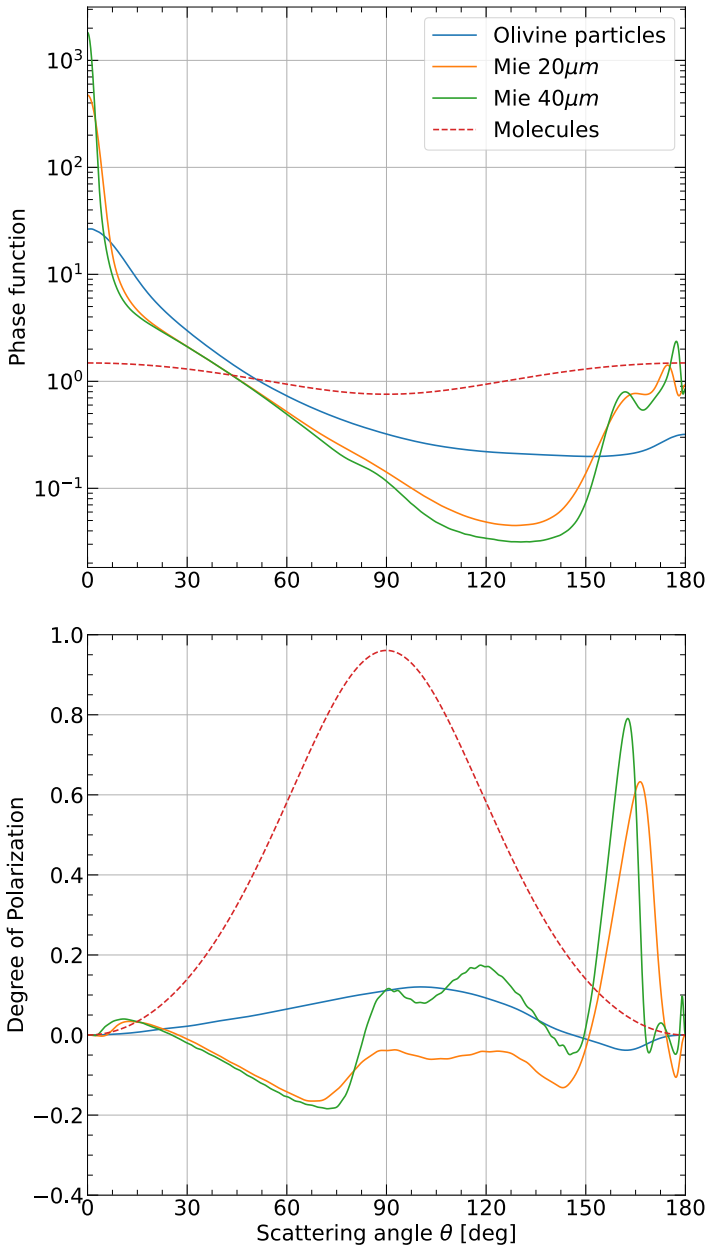

Figure 4.9: The flux (top) and degree of polarization (bottom) of incident unpolarized light that has been singly scattered by the gas molecules, the irregularly shaped ring particles [94, 98], and perfect spheres with radii of 20μm and 40μm as functions of the single scattering angle. Similar to the single scattering figure in the paper (see, Sect. 2). This figure is copied over from App. A for clarity.

Table 4.2: The model parameters that were used for the distance dependency study. Any value not mentioned here is the same as in Table 4.1.

Parameter	Value
i	$89.0°$
e	0
ν	$270°$
a	$3 - 20$ AU
b	1.0
ϖ	0.3
Particle	Olivine dust ($r_{eff} = 1\ \mu m$ [94])

4.2.3. Varying the distance

Even though it is clear that the expected reflected flux is well below the detection limit, the degree of polarization was also measured. In the unpublished paper by van Dam et al. [91] they also reported on the detection limit of the degree of polarization which can be seen in Fig. 4.10. They assumed that the flux of J1407b would mostly be due to thermal emissions, a reasonable assumption considering the young age of the system and the suspected mass of J1407b. Any polarized flux would then come only from the reflected starlight because thermal emissions have low polarization [7]. The magnitude difference in the title of each plot alludes to the flux of J1407b which is dominated by the thermal emissions. In order to compare any results better to the calculated detection limit, another computation will be done to show the reflected flux, polarized flux, and degree of polarization as a function of the angular separation. To do this the ring orientation is assumed to be known as both the original paper reporting on J1407b [37] as well as the detailed fit show a similar orientation [35]. Since only the distance to the star is important, the computations are done using a circular orbit, with an orbital inclination of $89°$, and the data has been obtained at a true anomaly of $270°$. The ring has an optical thickness of 1.0 and is assumed to be comprised of the more realistic olivine particles. A list of the used model parameters is shown in Table 4.2.

The results of these extra computations are shown in Fig.4.11 and again confirm that the flux of the system is well below the detection limit. The degree of the polarization curve cannot be compared directly with the detection limit as shown in Fig. 4.10 because Fig. 4.11 only shows the reflected light. This light has a quite high 10% degree of polarization but would not be observable due to the low flux. Before a proper comparison with the detection limit is made, the unexpected changes in the degree of polarization will be explained. Since the orbit is circular, and the degree of polarization is a relative measure, it should remain constant when the distance to the star is increased (or decreased). This is not the case here because of the large size of the ring and the therefore non-unidirectional illumination angles. Even though the increase in the degree of polarization is small, only around 0.1%, using unidirectional illumination angles would have introduced a significant overestimation considering the detection limit for $\Delta m = 3$ mag and $\Delta m = 4$ mag is accurate on the order of 0.1%. As expected, when the planet and ring move away from the star this effect diminishes, and beyond 100 mas the assumption of uni-directional incident light would be accurate enough.

To properly compare the computed degree of polarization with the calculated detection limits, the computed polarized flux has been used to calculate the degree of polarization in the case that there is thermal emission. Assuming that the thermal emission is unpolarized the reflected light would be the only source of polarization. Since the reflected flux is rather small the degree of polarization can be approximated as

$$P = \frac{\sqrt{Q_{reflected}^2 + U_{reflected}^2}}{F_{thermal}} \tag{4.2}$$

with $F_{thermal}$ the thermal radiation that is assumed to be 3, 4, 5, or 6 mag. This degree of polarization is shown in Fig. 4.12.

Comparing these results to Fig. 4.10 it is clear that again the simulated values are below the de-

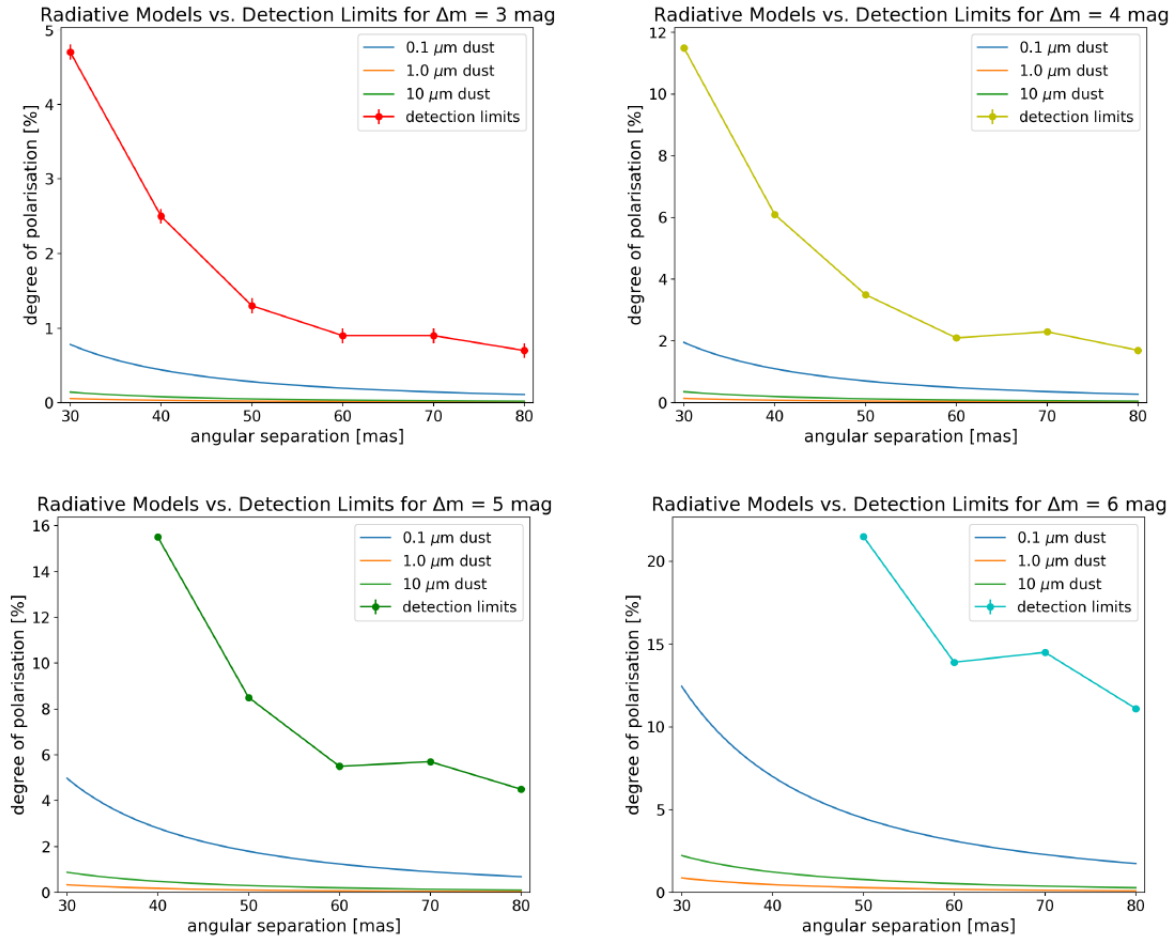

Figure 4.10: Results from van Dam et al. [91]. Their degree of polarization assumes a planet that predominantly emits thermal radiation and that reflects little light. The degree of polarization, and the respective detection limits, are shown as a function of angular separation in milliarcseconds (mas) for different planetary brightnesses.

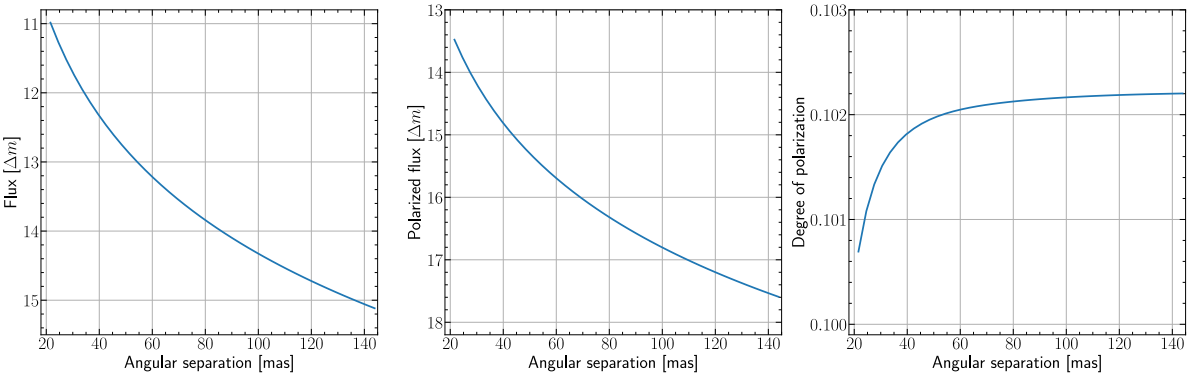

Figure 4.11: The reflected flux, polarized flux, and degree of polarization as a function of the angular separation in mas.

tection limit. The upper limit simulations that were done by van Dam et al. [91] come to the same conclusion. What is interesting though is that when comparing the results from Fig. 4.12 to the 1 μm lines in Fig. 4.10 the newly obtained values appear to be much lower. In the unpublished paper by van Dam et al. [91] they mention that for $\Delta m = 6$ mag at 40 mas the degree of polarization is 0.5% which is significantly higher than the 0.03% obtained here. Our lower values are probably caused by some of the differences in the model. Since the orientation of the ring is not mentioned by van Dam et al. [91] the reason for the differences is difficult to determine here and will have to wait for a follow-up study.

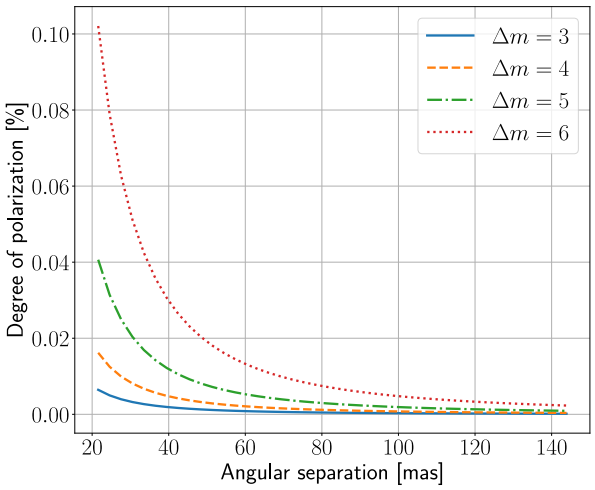

Figure 4.12: The degree of polarization as a function of the angular separation in milliarcseconds assuming the flux is dominated by thermal emission of the planet.

4.2.4. Summary and discussion

This has been a brief look at J1407b and a wide part of the parameter space was explored. Some missing differences in this study are the lack of different ring orientations, ring sizes, and the fact that homogeneous rings were used. These were omitted to keep the study small and clear but it's possible that some important insights have been missed.

What gives some validity to the presented results is that both the parameter sweep and distance dependency study show that, according to the simulations, the predicted flux lies well below the detection limit. Which is the same conclusion as van Dam et al. [91]. The modeling of the full orbit has given some extra insights such as that it is reasonable that no forward scattering peak was found, given the used telescopes and the young age of the star. Something that a priori might be expected of such a large ring. The model that is presented here is most likely more accurate in terms of scattering behavior than the one presented in the paper. This gives the nondetection more validity and should pave the way to more observations, especially because van Dam et al. [91] reported that the observation conditions were very poor, resulting in much higher detection limits. The theoretical contrast limit is 10^{-5} [99] which corresponds to a Δm of 12.5 which would be enough to constrain the possible distance of J1407b to the star significantly, or of course detect it.

It should also briefly be noted that Stolker et al. [54] showed that the assumption that thermal radiation is unpolarized might not be completely true. Both the results for the degree of polarization presented here as well as in van Dam et al. [91] might thus be either on the low or high side, depending on the orientation of the polarization of the thermally emitted radiation.

In a follow-up study, and/or following more observations, the parameter sweep should be expanded to include different ring orientations and non-homogenous rings. Especially the latter is interesting to further investigate for two reasons. One is that if the asymmetric and variable transit light curve that was observed before, is indeed confirmed with new observations, it is likely caused by a ring. This ring is then expected to have radial optical thickness variations based on its transit light curve and a new simulation should reflect that. Second is the novelty of such a study as the reflected light and polarization signal of non-homogenous rings have never been modeled. Such non-homogeneities might have a big impact on the degree of polarization depending on the orientation of the ring. Going back to Fig. 4.6, imagine a ring illuminated at $30°$, the polarized flux from the optically thick regions might cancel the polarization of the optically thin regions which could result in distinct dips in the polarization signal that would be hard to explain otherwise.

5
Recommendations

The following is a list of recommendations for new research and improvements to `Pryngles`:

- Add methane or clouds to the model of the planet to increase the realism and make the signal of the planet more wavelength dependent as done by Stam et al. [7], Karalidi et al. [70]. The addition of methane could make the planet fainter in some wavelengths leading to a possible underestimation of the size of the ring. Observing at multiple wavelengths could then in turn allow for more accurate ring size estimates without a transit. Any clouds in the planetary atmosphere could have the opposite effect, boosting the reflected flux as well as decreasing the degree of polarization (only in some orientations), leading to a possible overestimation of the ring size. It should be noted that the percentage of methane in the atmosphere and/or the percentage of cloud coverage of an exoplanet is unknown so it will still be difficult to estimate the ring radius. Characterizing the effect of these three properties: methane, clouds, and a ring and how they interact with each other would be a good follow-up study.
- Implement the correct illumination angles for when the planet is close to the star. As mentioned in Sect. A.1.2, this could potentially give a significant increase in accuracy, especially when computing the transit of a close-in planet. Given the bias of the transit method for detecting close-in giant planets, such a correction would be very relevant.
- Implement the use of a more well-rounded interpolation algorithm, such as a weighted bicubic spline interpolator [100, 101]. This is especially important to be able to simulate particles that have a higher size parameter x, and thus a larger forward scattering peak. The bicubic spline interpolator that is currently being used, as mentioned in Sect. 2, produces overshoots in the Fourier-coefficients when x becomes too large.
- Include the possibility to use different irregular particles into the `Pryngles` package, such as some of the particles found in the Amsterdam-Granada database [102]. As was shown in Sect. 4.2 and Fig. A.3 the size and shape of a particle can have a big influence on its scattering behavior. It is therefore important for future fitting of reflected light observations to be able to vary the particle size without having to use less realistic Mie-scatterers.

Bibliography

[1] Morbidelli, A., Lunine, J. I., O'Brien, D. P., Raymond, S. N., and Walsh, K. J., "Building terrestrial planets," *Annual Review of Earth and Planetary Sciences*, Vol. 40, 2012, pp. 251–275.

[2] Lissauer, J. J., and Pater, I., *Fundamental Planetary Science (updated edition)*, Cambridge University Press, 2019.

[3] Wolszczan, A., and Frail, D. A., "A planetary system around the millisecond pulsar PSR1257+ 12," *Nature*, Vol. 355, No. 6356, 1992, pp. 145–147.

[4] Mayor, M., and Queloz, D., "A Jupiter-mass companion to a solar-type star," *Nature*, Vol. 378, No. 6555, 1995, pp. 355–359.

[5] Beuzit, J.-L., Feldt, M., Dohlen, K., Mouillet, D., Puget, P., Wildi, F., Abe, L., Antichi, J., Baruffolo, A., Baudoz, P., et al., "SPHERE: a planet finder instrument for the VLT," *Ground-based and airborne instrumentation for astronomy II*, Vol. 7014, International Society for Optics and Photonics, 2008, p. 701418.

[6] Macintosh, B., Graham, J., Palmer, D., Doyon, R., Gavel, D., Larkin, J., Oppenheimer, B., Saddlemyer, L., Wallace, J. K., Bauman, B., et al., "The Gemini planet imager," *Advances in Adaptive Optics II*, Vol. 6272, International Society for Optics and Photonics, 2006, p. 62720L.

[7] Stam, D., Hovenier, J., and Waters, L., "Using polarimetry to detect and characterize Jupiter-like extrasolar planets," *Astronomy & Astrophysics*, Vol. 428, No. 2, 2004, pp. 663–672.

[8] Marois, C., Macintosh, B., Barman, T., Zuckerman, B., Song, I., Patience, J., Lafrenière, D., and Doyon, R., "Direct imaging of multiple planets orbiting the star HR 8799," *science*, Vol. 322, No. 5906, 2008, pp. 1348–1352.

[9] Macintosh, B., Graham, J., Barman, T., De Rosa, R., Konopacky, Q., Marley, M., Marois, C., Nielsen, E., Pueyo, L., Rajan, A., et al., "Discovery and spectroscopy of the young jovian planet 51 Eri b with the Gemini Planet Imager," *Science*, Vol. 350, No. 6256, 2015, pp. 64–67.

[10] Wagner, K., Apai, D., Kasper, M., Kratter, K., McClure, M., Robberto, M., and Beuzit, J.-L., "Direct imaging discovery of a Jovian exoplanet within a triple-star system," *Science*, Vol. 353, No. 6300, 2016, pp. 673–678.

[11] Kemp, J. C., Henson, G., Steiner, C., and Powell, E., "The optical polarization of the Sun measured at a sensitivity of parts in ten million," *Nature*, Vol. 326, No. 6110, 1987, pp. 270–273.

[12] Jensen-Clem, R., Hinz, P., Von Kooten, M., Fitzgerald, M. P., Sallum, S., Mazin, B., Chun, M., Max, C., Millar-Blanchaer, M., Guyon, O., et al., "The Planetary Systems Imager adaptive optics system: an initial optical design and performance analysis tool for the PSI-Red AO system," *Techniques and Instrumentation for Detection of Exoplanets X*, Vol. 11823, International Society for Optics and Photonics, 2021, p. 1182309.

[13] Charnoz, S., Canup, R., Crida, A., and Dones, L., "The origin of planetary ring systems," *arXiv preprint arXiv:1703.09741*, 2017.

[14] Barnes, J. W., and Fortney, J. J., "Transit detectability of ring systems around extrasolar giant planets," *The Astrophysical Journal*, Vol. 616, No. 2, 2004, p. 1193.

[15] Dyudina, U. A., Sackett, P. D., Bayliss, D. D., Seager, S., Porco, C. C., Throop, H. B., and Dones, L., "Phase light curves for extrasolar Jupiters and Saturns," *The Astrophysical Journal*, Vol. 618, No. 2, 2005, p. 973.

[16] Batygin, K., and Morbidelli, A., "Formation of giant planet satellites," *The Astrophysical Journal*, Vol. 894, No. 2, 2020, p. 143.

[17] Dubinski, J., "A recent origin for Saturn's rings from the collisional disruption of an icy moon," *Icarus*, Vol. 321, 2019, pp. 291–306.

[18] Canup, R. M., "Origin of Saturn's rings and inner moons by mass removal from a lost Titan-sized satellite," *Nature*, Vol. 468, No. 7326, 2010, pp. 943–946.

[19] Crida, A., Charnoz, S., Hsu, H.-W., and Dones, L., "Are Saturn's rings actually young?" *Nature Astronomy*, Vol. 3, No. 11, 2019, pp. 967–970.

[20] Cuzzi, J. N., Burns, J. A., Charnoz, S., Clark, R. N., Colwell, J. E., Dones, L., Esposito, L. W., Filacchione, G., French, R. G., Hedman, M. M., Kempf, S., Marouf, E. A., Murray, C. D., Nicholson, P. D., Porco, C. C., Schmidt, J., Showalter, M. R., Spilker, L. J., Spitale, J. N., Srama, R., Sremčević, M., Tiscareno, M. S., and Weiss, J., "An Evolving View of Saturn's Dynamic Rings," *Science*, Vol. 327, No. 5972, 2010, pp. 1470–1475. doi: 10.1126/science.1179118.

[21] Matson, D. L., Castillo-Rogez, J. C., Schubert, G., Sotin, C., and McKinnon, W. B., "The Thermal Evolution and Internal Structure of Saturn's Mid-Sized Icy Satellites," *Saturn from Cassini-Huygens*, edited by M. K. Dougherty, L. W. Esposito, and S. M. Krimigis, 2009, p. 577. doi: 10.1007/978-1-4020-9217-6$_1$8.

[22] Colwell, J., "The disruption of planetary satellites and the creation of planetary rings," *Planetary and Space Science*, Vol. 42, No. 12, 1994, pp. 1139–1149.

[23] Schlichting, H. E., and Chang, P., "Warm Saturns: On the Nature of Rings around Extrasolar Planets That Reside inside the Ice Line," , Vol. 734, No. 2, 2011, 117. doi: 10.1088/0004-637X/734/2/117.

[24] Tremaine, S., Touma, J., and Namouni, F., "Satellite Dynamics on the Laplace Surface," , Vol. 137, No. 3, 2009, pp. 3706–3717. doi: 10.1088/0004-6256/137/3/3706.

[25] Pollack, J. B., Hubickyj, O., Bodenheimer, P., Lissauer, J. J., Podolak, M., and Greenzweig, Y., "Formation of the giant planets by concurrent accretion of solids and gas," *icarus*, Vol. 124, No. 1, 1996, pp. 62–85.

[26] Winn, J. N., and Fabrycky, D. C., "The occurrence and architecture of exoplanetary systems," *Annual Review of Astronomy and Astrophysics*, Vol. 53, 2015, pp. 409–447.

[27] Lunine, J. I., and Stevenson, D. J., "Formation of the galilean satellites in a gaseous nebula," , Vol. 52, No. 1, 1982, pp. 14–39. doi: 10.1016/0019-1035(82)90166-X.

[28] Canup, R. M., and Ward, W. R., "Formation of the Galilean Satellites: Conditions of Accretion," , Vol. 124, No. 6, 2002, pp. 3404–3423. doi: 10.1086/344684.

[29] Canup, R. M., and Ward, W. R., "A common mass scaling for satellite systems of gaseous planets," , Vol. 441, No. 7095, 2006, pp. 834–839. doi: 10.1038/nature04860.

[30] Miguel, Y., and Ida, S., "A semi-analytical model for exploring Galilean satellites formation from a massive disk," , Vol. 266, 2016, pp. 1–14. doi: 10.1016/j.icarus.2015.10.030.

[31] Teague, R., Bae, J., and Bergin, E. A., "Meridional flows in the disk around a young star," , Vol. 574, No. 7778, 2019, pp. 378–381. doi: 10.1038/s41586-019-1642-0.

[32] Cilibrasi, M., Szulágyi, J., Mayer, L., Drążkowska, J., Miguel, Y., and Inderbitzi, P., "Satellites form fast & late: a population synthesis for the Galilean moons," , Vol. 480, No. 4, 2018, pp. 4355–4368. doi: 10.1093/mnras/sty2163.

[33] Crida, A., and Charnoz, S., "Formation of regular satellites from ancient massive rings in the solar system," *Science*, Vol. 338, No. 6111, 2012, pp. 1196–1199.

[34] Crida, A., and Charnoz, S., "Complex satellite systems: a general model of formation from rings," *Proceedings of the International Astronomical Union*, Vol. 9, No. S310, 2014, pp. 182–189.

[35] Kenworthy, M. A., and Mamajek, E. E., "Modeling giant extrasolar ring systems in eclipse and

the case of J1407b: sculpting by exomoons?" *The Astrophysical Journal*, Vol. 800, No. 2, 2015, p. 126.

[36] Keppler, M., Benisty, M., Müller, A., Henning, T., Van Boekel, R., Cantalloube, F., Ginski, C., Van Holstein, R., Maire, A.-L., Pohl, A., et al., "Discovery of a planetary-mass companion within the gap of the transition disk around PDS 70," *Astronomy & Astrophysics*, Vol. 617, 2018, p. A44.

[37] Mamajek, E. E., Quillen, A. C., Pecaut, M. J., Moolekamp, F., Scott, E. L., Kenworthy, M. A., Cameron, A. C., and Parley, N. R., "Planetary construction zones in occultation: discovery of an extrasolar ring system transiting a young Sun-like star and future prospects for detecting eclipses by circumsecondary and circumplanetary disks," *The Astronomical Journal*, Vol. 143, No. 3, 2012, p. 72.

[38] Mamajek, E. E., "Initial Conditions of Planet Formation: Lifetimes of Primordial Disks," *Exoplanets and Disks: Their Formation and Diversity*, American Institute of Physics Conference Series, Vol. 1158, edited by T. Usuda, M. Tamura, and M. Ishii, 2009, pp. 3–10. doi: 10.1063/1.3215910.

[39] Drążkowska, J., and Szulágyi, J., "Dust Evolution and Satellitesimal Formation in Circumplanetary Disks," , Vol. 866, No. 2, 2018, 142. doi: 10.3847/1538-4357/aae0fd.

[40] Heising, M. Z., Marcy, G. W., and Schlichting, H. E., "A Search for Ringed Exoplanets Using Kepler Photometry," , Vol. 814, No. 1, 2015, 81. doi: 10.1088/0004-637X/814/1/81.

[41] Aizawa, M., Uehara, S., Masuda, K., Kawahara, H., and Suto, Y., "Toward Detection of Exoplanetary Rings via Transit Photometry: Methodology and a Possible Candidate," , Vol. 153, No. 4, 2017, 193. doi: 10.3847/1538-3881/aa6336.

[42] Aizawa, M., Masuda, K., Kawahara, H., and Suto, Y., "Systematic Search for Rings around Kepler Planet Candidates: Constraints on Ring Size and Occurrence Rate," , Vol. 155, No. 5, 2018, 206. doi: 10.3847/1538-3881/aab9a1.

[43] Roddier, F., and Roddier, C., "Stellar Coronograph with Phase Mask," , Vol. 109, 1997, pp. 815–820. doi: 10.1086/133949.

[44] Fusco, T., Rousset, G., Sauvage, J. F., Petit, C., Beuzit, J. L., Dohlen, K., Mouillet, D., Charton, J., Nicolle, M., Kasper, M., Baudoz, P., and Puget, P., "High-order adaptive optics requirements for direct detection of extrasolar planets: Application to the SPHERE instrument," *Optics Express*, Vol. 14, No. 17, 2006, p. 7515. doi: 10.1364/OE.14.007515.

[45] Marois, C., Lafrenière, D., Doyon, R., Macintosh, B., and Nadeau, D., "Angular Differential Imaging: A Powerful High-Contrast Imaging Technique," , Vol. 641, No. 1, 2006, pp. 556–564. doi: 10.1086/500401.

[46] Kuhn, J. R., Potter, D., and Parise, B., "Imaging Polarimetric Observations of a New Circumstellar Disk System," , Vol. 553, No. 2, 2001, pp. L189–L191. doi: 10.1086/320686.

[47] Rappaport, S., Zhou, G., Vanderburg, A., Mann, A., Kristiansen, M. H., Oláh, K., Jacobs, T. L., Newton, E., Omohundro, M. R., LaCourse, D., Schwengeler, H. M., Terentev, I. A., Latham, D. W., Bieryla, A., Soares-Furtado, M., Bouma, L. G., Ireland, M. J., and Irwin, J., "Deep long asymmetric occultation in EPIC 204376071," , Vol. 485, No. 2, 2019, pp. 2681–2693. doi: 10.1093/mnras/stz537.

[48] van Dam, D. M., Kenworthy, M. A., David, T. J., Mamajek, E. E., Hillenbrand, L. A., Cody, A. M., Howard, A. W., Isaacson, H., Ciardi, D. R., Rebull, L. M., Stauffer, J. R., Patel, R., Cameron + WASP Collaborators, A. C., Rodriguez, J. E., Pojmański, G., Gonzales, E. J., Schlieder, J. E., Hambsch, F.-J., Dufoer, S., Vanmunster, T., Dubois, F., Vanaverbeke, S., Logie, L., and Rau, S., "An Asymmetric Eclipse Seen toward the Pre-main-sequence Binary System V928 Tau," , Vol. 160, No. 6, 2020, 285. doi: 10.3847/1538-3881/abc259.

[49] Pollacco, D. L., Skillen, I., Collier Cameron, A., Christian, D. J., Hellier, C., Irwin, J., Lister, T. A., Street, R. A., West, R. G., Anderson, D. R., Clarkson, W. I., Deeg, H., Enoch, B., Evans, A.,

Fitzsimmons, A., Haswell, C. A., Hodgkin, S., Horne, K., Kane, S. R., Keenan, F. P., Maxted, P. F. L., Norton, A. J., Osborne, J., Parley, N. R., Ryans, R. S. I., Smalley, B., Wheatley, P. J., and Wilson, D. M., "The WASP Project and the SuperWASP Cameras," , Vol. 118, No. 848, 2006, pp. 1407–1418. doi: 10.1086/508556.

[50] Butters, O. W., West, R. G., Anderson, D. R., Collier Cameron, A., Clarkson, W. I., Enoch, B., Haswell, C. A., Hellier, C., Horne, K., Joshi, Y., Kane, S. R., Lister, T. A., Maxted, P. F. L., Parley, N., Pollacco, D., Smalley, B., Street, R. A., Todd, I., Wheatley, P. J., and Wilson, D. M., "The first WASP public data release," , Vol. 520, 2010, L10. doi: 10.1051/0004-6361/201015655.

[51] Rieder, S., and Kenworthy, M. A., "Constraints on the size and dynamics of the J1407b ring system," *Astronomy & Astrophysics*, Vol. 596, 2016, p. A9.

[52] Kenworthy, M. A., Lacour, S., Kraus, A., Triaud, A. H. M. J., Mamajek, E. E., Scott, E. L., Ségransan, D., Ireland, M., Hambsch, F. J., Reichart, D. E., Haislip, J. B., LaCluyze, A. P., Moore, J. P., and Frank, N. R., "Mass and period limits on the ringed companion transiting the young star J1407," , Vol. 446, No. 1, 2015, pp. 411–427. doi: 10.1093/mnras/stu2067.

[53] Kenworthy, M. A., Klaassen, P. D., Min, M., van der Marel, N., Bohn, A. J., Kama, M., Triaud, A., Hales, A., Monkiewicz, J., Scott, E., and Mamajek, E. E., "ALMA and NACO observations towards the young exoring transit system J1407 (V1400 Cen)," , Vol. 633, 2020, A115. doi: 10.1051/0004-6361/201936141.

[54] Stolker, T., Min, M., Stam, D. M., Mollière, P., Dominik, C., and Waters, L., "Polarized scattered light from self-luminous exoplanets-three-dimensional scattering radiative transfer with artes," *Astronomy & Astrophysics*, Vol. 607, 2017, p. A42.

[55] Isella, A., Benisty, M., Teague, R., Bae, J., Keppler, M., Facchini, S., and Pérez, L., "Detection of continuum submillimeter emission associated with candidate protoplanets," *The Astrophysical Journal Letters*, Vol. 879, No. 2, 2019, p. L25.

[56] Benisty, M., Bae, J., Facchini, S., Keppler, M., Teague, R., Isella, A., Kurtovic, N. T., Pérez, L. M., Sierra, A., Andrews, S. M., Carpenter, J., Czekala, I., Dominik, C., Henning, T., Menard, F., Pinilla, P., and Zurlo, A., "A Circumplanetary Disk around PDS70c," , Vol. 916, No. 1, 2021, L2. doi: 10.3847/2041-8213/ac0f83.

[57] Piro, A. L., and Vissapragada, S., "Exploring Whether Super-puffs can be Explained as Ringed Exoplanets," , Vol. 159, No. 4, 2020, 131. doi: 10.3847/1538-3881/ab7192.

[58] Lopez, E. D., and Fortney, J. J., "Re-inflated Warm Jupiters around Red Giants," , Vol. 818, No. 1, 2016, 4. doi: 10.3847/0004-637X/818/1/4.

[59] Santerne, A., Malavolta, L., Kosiarek, M. R., Dai, F., Dressing, C. D., Dumusque, X., Hara, N. C., Lopez, T. A., Mortier, A., Vanderburg, A., Adibekyan, V., Armstrong, D. J., Barrado, D., Barros, S. C. C., Bayliss, D., Berardo, D., Boisse, I., Bonomo, A. S., Bouchy, F., Brown, D. J. A., Buchhave, L. A., Butler, R. P., Collier Cameron, A., Cosentino, R., Crane, J. D., Crossfield, I. J. M., Damasso, M., Deleuil, M. R., Delgado Mena, E., Demangeon, O., Díaz, R. F., Donati, J. F., Figueira, P., Fulton, B. J., Ghedina, A., Harutyunyan, A., Hébrard, G., Hirsch, L. A., Hojjatpanah, S., Howard, A. W., Isaacson, H., Latham, D. W., Lillo-Box, J., López-Morales, M., Lovis, C., Martinez Fiorenzano, A. F., Molinari, E., Mousis, O., Moutou, C., Nava, C., Nielsen, L. D., Osborn, H. P., Petigura, E. A., Phillips, D. F., Pollacco, D. L., Poretti, E., Rice, K., Santos, N. C., Ségransan, D., Shectman, S. A., Sinukoff, E., Sousa, S. G., Sozzetti, A., Teske, J. K., Udry, S., Vigan, A., Wang, S. X., Watson, C. A., Weiss, L. M., Wheatley, P. J., and Winn, J. N., "An extremely low-density and temperate giant exoplanet," *arXiv e-prints*, 2019, arXiv:1911.07355.

[60] Akinsanmi, B., Santos, N. C., Faria, J. P., Oshagh, M., Barros, S. C. C., Santerne, A., and Charnoz, S., "Can planetary rings explain the extremely low density of HIP 41378 f?" , Vol. 635, 2020, L8. doi: 10.1051/0004-6361/202037618.

[61] Alam, M. K., Kirk, J., Dressing, C. D., López-Morales, M., Ohno, K., Gao, P., Akinsanmi, B., Santerne, A., Grouffal, S., Adibekyan, V., Barros, S. C. C., Buchhave, L. A., Crossfield, I. J. M., Dai, F., Deleuil, M., Giacalone, S., Lillo-Box, J., Marley, M., Mayo, A. W., Mortier, A., Santos, N. C., Sousa, S. G., Turtelboom, E. V., Wheatley, P. J., and Vanderburg, A. M., "The First Near-infrared Transmission Spectrum of HIP 41378 f, A Low-mass Temperate Jovian World in a Multiplanet System," , Vol. 927, No. 1, 2022, L5. doi: 10.3847/2041-8213/ac559d.

[62] Hansen, J. E., and Hovenier, J., "Interpretation of the polarization of Venus," *Journal of Atmospheric Sciences*, Vol. 31, No. 4, 1974, pp. 1137–1160.

[63] Seager, S., Whitney, B., and Sasselov, D., "Photometric light curves and polarization of close-in extrasolar giant planets," *The Astrophysical Journal*, Vol. 540, No. 1, 2000, p. 504.

[64] Stam, D., "Spectropolarimetric signatures of Earth-like extrasolar planets," *Astronomy & Astrophysics*, Vol. 482, No. 3, 2008, pp. 989–1007.

[65] Zugger, M. E., Kasting, J. F., Williams, D. M., Kane, T. J., and Philbrick, C. R., "Light scattering from exoplanet oceans and atmospheres," *The Astrophysical Journal*, Vol. 723, No. 2, 2010, p. 1168.

[66] Karalidi, T., Stam, D., and Hovenier, J., "Looking for the rainbow on exoplanets covered by liquid and icy water clouds," *Astronomy & Astrophysics*, Vol. 548, 2012, p. A90.

[67] Berdyugina, S. V., Kuhn, J. R., Harrington, D. M., Šantl-Temkiv, T., and Messersmith, E. J., "Remote sensing of life: polarimetric signatures of photosynthetic pigments as sensitive biomarkers," *International Journal of Astrobiology*, Vol. 15, No. 1, 2016, pp. 45–56.

[68] Buenzli, E., and Schmid, H. M., "A grid of polarization models for Rayleigh scattering planetary atmospheres," *Astronomy & Astrophysics*, Vol. 504, No. 1, 2009, pp. 259–276.

[69] Madhusudhan, N., and Burrows, A., "Analytic models for albedos, phase curves, and polarization of reflected light from exoplanets," *The Astrophysical Journal*, Vol. 747, No. 1, 2012, p. 25.

[70] Karalidi, T., Stam, D., and Guirado, D., "Flux and polarization signals of spatially inhomogeneous gaseous exoplanets," *Astronomy & Astrophysics*, Vol. 555, 2013, p. A127.

[71] West, R. A., Dumont, P., Hu, R., Natraj, V., Breckinridge, J., and Chen, P., "Spectropolarimetry as a Means to Address Cloud Composition and Habitability for a Cloudy Exoplanetary Atmosphere in the Habitable Zone," , Vol. 940, No. 2, 2022, 183. doi: 10.3847/1538-4357/ac9b42.

[72] Kostogryz, N., Yakobchuk, T., and Berdyugina, S., "Polarization in exoplanetary systems caused by transits, grazing transits, and starspots," *The Astrophysical Journal*, Vol. 806, No. 1, 2015, p. 97.

[73] Sengupta, S., "Polarimetric detection of exoplanets transiting T and L brown dwarfs," *The Astronomical Journal*, Vol. 152, No. 4, 2016, p. 98.

[74] Arnold, L., and Schneider, J., "The detectability of extrasolar planet surroundings-I. Reflected-light photometry of unresolved rings," *Astronomy & Astrophysics*, Vol. 420, No. 3, 2004, pp. 1153–1162.

[75] Sucerquia, M., Alvarado-Montes, J. A., Zuluaga, J. I., Montesinos, M., and Bayo, A., "Scattered light may reveal the existence of ringed exoplanets," , Vol. 496, No. 1, 2020, pp. L85–L90. doi: 10.1093/mnrasl/slaa080.

[76] Zuluaga, J. I., Sucerquia, M., and Alvarado-Montes, J. A., "The bright side of the light curve: A general photometric model of non-transiting exorings," *Astronomy and Computing*, Vol. 40, 2022, 100623. doi: 10.1016/j.ascom.2022.100623.

[77] Ohno, K., and Fortney, J. J., "A Framework for Characterizing Transmission Spectra of Exoplanets with Circumplanetary Rings," , Vol. 930, No. 1, 2022, 50. doi: 10.3847/1538-4357/ac6029.

[78] Lietzow, M., and Wolf, S., "Scattered polarized radiation of extrasolar circumplanetary rings," *arXiv e-prints*, 2023, arXiv:2302.06508. doi: 10.48550/arXiv.2302.06508.

[79] Hansen, J. E., and Travis, L. D., "Light scattering in planetary atmospheres," *Space science reviews*, Vol. 16, No. 4, 1974, pp. 527–610.

[80] Hovenier, J. W., Van der Mee, C. V., and Domke, H., *Transfer of polarized light in planetary atmospheres: basic concepts and practical methods*, Vol. 318, Springer Science & Business Media, 2004.

[81] Liou, K. N., *Introduction to Atmospheric Radiation (2nd Edition)*, Elsevier, 2002. URL https://app.knovel.com/hotlink/toc/id:kpIARE0015/introduction-atmospheric/introduction-atmospheric.

[82] Mishchenko, M., "Light scattering by randomly oriented axially symmetric particles," *JOSA A*, Vol. 8, No. 6, 1991, pp. 871–882.

[83] Dave, J., "Scattering of visible light by large water spheres," *Applied Optics*, Vol. 8, No. 1, 1969, pp. 155–164.

[84] Kattawar, G. W., and Plass, G. N., "Electromagnetic scattering from absorbing spheres," *Applied Optics*, Vol. 6, No. 8, 1967, pp. 1377–1382.

[85] Hansen, J. E., "Multiple scattering of polarized light in planetary atmospheres part II. Sunlight reflected by terrestrial water clouds," *Journal of the Atmospheric Sciences*, Vol. 28, No. 8, 1971, pp. 1400–1426.

[86] Cuzzi, J., Clark, R., Filacchione, G., French, R., Johnson, R., Marouf, E., and Spilker, L., "Ring Particle Composition and Size Distribution," *Saturn from Cassini-Huygens*, edited by M. K. Dougherty, L. W. Esposito, and S. M. Krimigis, 2009, p. 459. doi: 10.1007/978-1-4020-9217-6_15.

[87] Ye, S. Y., Gurnett, D. A., and Kurth, W. S., "In-situ measurements of Saturn's dusty rings based on dust impact signals detected by Cassini RPWS," , Vol. 279, 2016, pp. 51–61. doi: 10.1016/j.icarus.2016.05.006.

[88] Dohnanyi, J. S., "Collisional Model of Asteroids and Their Debris," , Vol. 74, 1969, pp. 2531–2554. doi: 10.1029/JB074i010p02531.

[89] Rossi, L., Berzosa-Molina, J., and Stam, D. M., "PYMIEDAP: a Python-Fortran tool for computing fluxes and polarization signals of (exo)planets," , Vol. 616, 2018, A147. doi: 10.1051/0004-6361/201832859.

[90] Sutton, P. J., Albery, B., and Muff, J., "A Self-Gravitating Exoring Around J1407b and Implications for In-Situ Exomoon Formation," *Frontiers in Astronomy and Space Sciences*, Vol. 9, 2022, 819933. doi: 10.3389/fspas.2022.819933.

[91] van Dam, D. M., Ginski, C., Kenworthy, M. A., Min, M., and Cai, M. X., "The Search for an Extrasolar Ring System in Polarised Light with ZIMPOL," *Submitted to MNRAS in 2019 and reviewed but not yet re-submitted as of 2023*, ????

[92] Min, M., Dullemond, C., Dominik, C., de Koter, A., and Hovenier, J., "Radiative transfer in very optically thick circumstellar disks," *Astronomy & Astrophysics*, Vol. 497, No. 1, 2009, pp. 155–166.

[93] Mentel, R. T., Kenworthy, M. A., Cameron, D. A., Scott, E. L., Mellon, S. N., Hudec, R., Birkby, J. L., Mamajek, E. E., Schrimpf, A., Reichart, D. E., Haislip, J. B., Kouprianov, V. V., Hambsch, F. J., Tan, T. G., Hills, K., Grindlay, J. E., Rodriguez, J. E., Lund, M. B., and Kuhn, R. B., "Constraining the period of the ringed secondary companion to the young star J1407 with photographic plates," , Vol. 619, 2018, A157. doi: 10.1051/0004-6361/201834004.

[94] Munoz, O., Volten, H., De Haan, J., Vassen, W., and Hovenier, J., "Experimental determination of scattering matrices of olivine and Allende meteorite particles," *Astronomy and Astrophysics*,

Vol. 360, 2000, pp. 777–788.

[95] Sorahana, S., Yamamura, I., and Murakami, H., "On the Radii of Brown Dwarfs Measured with AKARI Near-infrared Spectroscopy," , Vol. 767, No. 1, 2013, 77. doi: 10.1088/0004-637X/767/1/77.

[96] Mishchenko, M. I., Travis, L. D., Kahn, R. A., and West, R. A., "Modeling phase functions for dust-like tropospheric aerosols using a shape mixture of randomly oriented polydisperse spheroids," , Vol. 102, 1997, pp. 13543–13553. doi: 10.1029/97JD01124.

[97] Nousiainen, T., Zubko, E., Lindqvist, H., Kahnert, M., and Tyynelä, J., "Comparison of scattering by different nonspherical, wavelength-scale particles," *Journal of Quantitative Spectroscopy and Radiative Transfer*, Vol. 113, No. 18, 2012, pp. 2391–2405.

[98] Moreno, F., Vilaplana, R., Munoz, O., Molina, A., and Guirado, D., "The scattering matrix for size distributions of irregular particles: An application to an olivine sample," *Journal of Quantitative Spectroscopy and Radiative Transfer*, Vol. 100, No. 1-3, 2006, pp. 277–287.

[99] Thalmann, C., Schmid, H. M., Boccaletti, A., Mouillet, D., Dohlen, K., Roelfsema, R., Carbillet, M., Gisler, D., Beuzit, J.-L., Feldt, M., Gratton, R., Joos, F., Keller, C. U., Kragt, I., Jan, Pragt, J. H., Puget, P., Rigal, F., Snik, F., Waters, R., and Wildi, F., "SPHERE ZIMPOL: overview and performance simulation," *Ground-based and Airborne Instrumentation for Astronomy II*, Society of Photo-Optical Instrumentation Engineers (SPIE) Conference Series, Vol. 7014, edited by I. S. McLean and M. M. Casali, 2008, p. 70143F. doi: 10.1117/12.789158.

[100] Duan, Q., Djidjeli, K., Price, W., and Twizell, E., "Weighted rational cubic spline interpolation and its application," *Journal of Computational and Applied Mathematics*, Vol. 117, No. 2, 2000, pp. 121–135. doi: https://doi.org/10.1016/S0377-0427(99)00336-2, URL https://www.sciencedirect.com/science/article/pii/S0377042799003362.

[101] wan Kim, T., and Kvasov, B., "A shape-preserving approximation by weighted cubic splines," *Journal of Computational and Applied Mathematics*, Vol. 236, No. 17, 2012, pp. 4383–4397. doi: https://doi.org/10.1016/j.cam.2012.04.001, URL https://www.sciencedirect.com/science/article/pii/S0377042712001616.

[102] Muñoz, O., Moreno, F., Guirado, D., Dabrowska, D. D., Volten, H., and Hovenier, J. W., "The Amsterdam-Granada Light Scattering Database," , Vol. 113, No. 7, 2012, pp. 565–574. doi: 10.1016/j.jqsrt.2012.01.014.

[103] Reissl, S., Wolf, S., and Brauer, R., "Radiative transfer with POLARIS. I. Analysis of magnetic fields through synthetic dust continuum polarization measurements," , Vol. 593, 2016, A87. doi: 10.1051/0004-6361/201424930.

[104] Plavchan, P., Barclay, T., Gagné, J., Gao, P., Cale, B., Matzko, W., Dragomir, D., Quinn, S., Feliz, D., Stassun, K., Crossfield, I. J. M., Berardo, D. A., Latham, D. W., Tieu, B., Anglada-Escudé, G., Ricker, G., Vanderspek, R., Seager, S., Winn, J. N., Jenkins, J. M., Rinehart, S., Krishnamurthy, A., Dynes, S., Doty, J., Adams, F., Afanasev, D. A., Beichman, C., Bottom, M., Bowler, B. P., Brinkworth, C., Brown, C. J., Cancino, A., Ciardi, D. R., Clampin, M., Clark, J. T., Collins, K., Davison, C., Foreman-Mackey, D., Furlan, E., Gaidos, E. J., Geneser, C., Giddens, F., Gilbert, E., Hall, R., Hellier, C., Henry, T., Horner, J., Howard, A. W., Huang, C., Huber, J., Kane, S. R., Kenworthy, M., Kielkopf, J., Kipping, D., Klenke, C., Kruse, E., Latouf, N., Lowrance, P., Mennesson, B., Mengel, M., Mills, S. M., Morton, T., Narita, N., Newton, E., Nishimoto, A., Okumura, J., Palle, E., Pepper, J., Quintana, E. V., Roberge, A., Roccatagliata, V., Schlieder, J. E., Tanner, A., Teske, J., Tinney, C. G., Vanderburg, A., von Braun, K., Walp, B., Wang, J., Wang, S. X., Weigand, D., White, R., Wittenmyer, R. A., Wright, D. J., Youngblood, A., Zhang, H., and Zilberman, P., "A planet within the debris disk around the pre-main-sequence star AU Microscopii," , Vol. 582, No. 7813, 2020, pp. 497–500. doi: 10.1038/s41586-020-2400-z.

[105] Deming, D., Knutson, H., Kammer, J., Fulton, B. J., Ingalls, J., Carey, S., Burrows, A., Fortney,

J. J., Todorov, K., Agol, E., Cowan, N., Desert, J.-M., Fraine, J., Langton, J., Morley, C., and Showman, A. P., “Spitzer Secondary Eclipses of the Dense, Modestly-irradiated, Giant Exoplanet HAT-P-20b Using Pixel-level Decorrelation,” , Vol. 805, No. 2, 2015, 132. doi: 10.1088/0004-637X/805/2/132.

[106] Mamajek, E. E., and Bell, C. P. M., “On the age of the β Pictoris moving group,” , Vol. 445, No. 3, 2014, pp. 2169–2180. doi: 10.1093/mnras/stu1894.

[107] Strubbe, L. E., and Chiang, E. I., “Dust Dynamics, Surface Brightness Profiles, and Thermal Spectra of Debris Disks: The Case of AU Microscopii,” , Vol. 648, No. 1, 2006, pp. 652–665. doi: 10.1086/505736.

A
Appendix

The study in Sect. A has been moved to the appendix because of too many open questions regarding the results of the fit. Sect. A.1 shows the fit of a transit that had some interesting features, that were possibly caused by the presence of a ring. The system posed some interesting technical problems that needed to be fixed before a proper transit fit could be made. These problems and the result of the fit are discussed below but a follow-up study should be performed to answer these questions and further validate the results.

A.1. Fitting a transit

One of the advantages of `Pryngles` is that it can also simulate the transit instead of only the reflected light. Other methods of simulating the reflected light that exist like the Monte-Carlo codes: MCMax [92], POLARIS [103], and ARTES [54], are unable to effectively simulate a transit. Fitting a transit and then simulating the reflected light along the orbit is also an interesting project that has not yet been done by using a single code for both tasks and that includes the polarization of light. An interesting candidate for this project was found to be the planet AU Microscopii b since it has already been fitted by a different group and has some interesting features in its transit [104]. Since the planet has already been fitted using a different code, this study could also be used to further verify `Pryngles`. The features appeared to originate from a ring, which added another reason to look at this system. After contact with the lead author of the paper, Peter Plavchan, he graciously sent over the data. The relevant observations were made using the 4.5 μm band on the Spitzer telescope [105].

Some background of the system is given in the paper by Plavchan et al. [104] which will be paraphrased here for clarity. AU Microscopii (AU Mic) is a young star system, roughly 22 Myr old [106], that is the second closest pre-main-sequence star, at a distance of only 9.79 parsecs. It has an edge-on debris disk extending from about 35 to 210 astronomical units (AU) from the star [107]. The transit fit that was already done was not based on the data shown in Fig. A.1 but on two transits observed using TESS and one using the Spitzer telescope. The fit finds that the planet, AU Mic b, has an orbital period of 8.46 days, an orbital distance of 0.07 AU, and a radius of 0.4 Jupiter radii at 3σ confidence. The mass of the planet is less than 0.18 Jupiter masses and is deduced from radial velocity measurements that were also performed. The young age of the star makes the detection of transits harder because of spots, plage, flares, and other manifestations of magnetic 'activity' on the star.

The fit of the transit that is presented here is mainly for demonstration purposes. Due to time constraints, it was not possible to perform an analysis of all the possibilities or to properly evaluate the significance of the obtained results. Still, the results and conclusions of the study are interesting enough to show as some general properties of transits are extracted. First, the detrended data will be shown and discussed in Sect. A.1.1. To try and fit the transit somewhat properly, parts of the `Pryngles` code had to be changed. What needed to be changed and the reason behind those changes will be explained in Sect. A.1.2. After that, the fit parameters and method will be given in Sect. A.1.3, followed by the results, a discussion of said results, and the conclusion in Sect. A.1.4.

A.1.1. The transit data

Of the three transits observed with the Spitzer telescope the third is used for the fit in this study as the detrended data shows some unusual behavior. Detrending the data attempts to eliminate the stellar activity that is present in the data. The detrended data is shown in Fig. A.1 and the peak at ingress as well as the sloped egress are features that could perhaps be due to a ring. In the detrended data from the transits observed by the TESS telescope, these features are not visible. This is then also a good time to mention that it is possible that the detrending of the Spitzer data was not completely successful in removing the effects of the stellar activity and that this causes these features to appear.

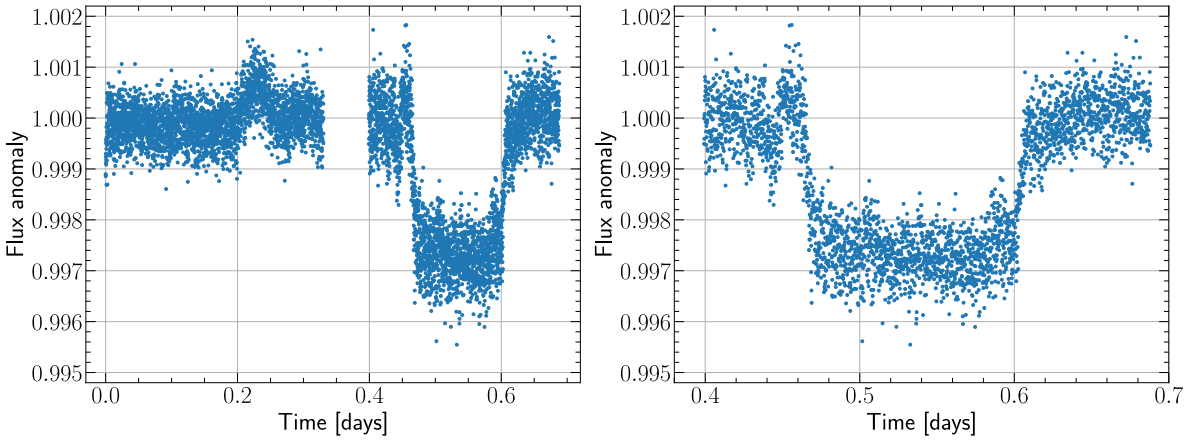

Figure A.1: The image on the left shows all the detrended data of the third transit that was observed with the Spitzer telescope. The right image contains the same data but zoomed in on the part that was used for the fit. The ingress happens around 0.45 days and the egress at 0.6 days.

A.1.2. Changes to the `Pryngles` code

The changes in the `Pryngles` code that had to be made had to do with the geometry of this particular system and not transits in general. At 0.07 AU, AU Mic b orbits very close to the star, for reference: Mercury has a semi-major axis of 0.387 AU [2]. It is also quite large, and the combination of those two properties makes the assumption of uni-directional illumination problematic. This decreases the accuracy of the computed forward scattering peak caused by a potential ring. To try and fix this problem two solutions, a simple and a more complicated one, were considered. The simple solution still assumes that the star is a point source but no longer assumes parallel incoming light so every spangle has its own, and different, illumination angle. The more complicated solution also assumes that the star has a size, describing the star as a flat plate that has been discretized into segments that each emit light. This solution would require a major rework of the code and also constitutes a significant increase in computation time. Both solutions were tested using the parameters for AU Mic b as mentioned above but assuming a circular orbit. In this system, the radius of the planet has an angular size of $0.16°$ when seen from the star. For the test, a ring was added with an outer radius of 2.25 planetary radii. This roughly doubled the angular size of the planet ring system to $0.35°$. The difference in the reflected flux is calculated for a single spangle at the outermost edge of the ring. Some other necessary model parameters are the radius of the star: AU Mic has a radius of $0.75 R_{\odot}$ [104] and the particles that are used: both the olivine particles [94, 98] as well as perfect spheres with a radius of 20 μm will be tested. The scattering of light by the perfect spheres is modeled at a wavelength of 4.5 μm like the Spitzer telescope, the scattering of light by the olivine particles is again modeled at 633 nm.

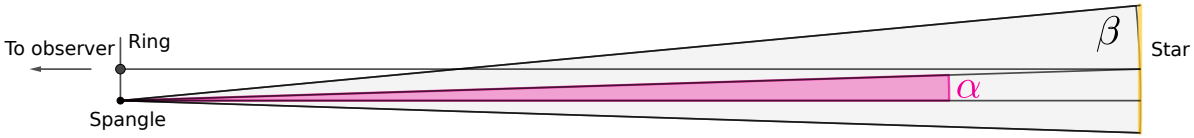

Figure A.2: A, not to scale, representation of the problem and the two possible solutions.

Figure A.2 is a representation of the two solutions, the distances and angles are not to scale. In the simple solution, the α angle is used as the illumination angle instead of the $0°$ if parallel light beams were assumed. The more complex solution uses the range of angles β that originate from 1000 uniformly but randomly distributed points on the star disk (the line shown in the image is a 2D representation of the disk). The differences in transmitted flux will be given as percentages of the flux obtained when assuming parallel light beams and are shown in Table A.1. Both the simple and complex solutions show a decrease in flux, which is to be expected because assuming parallel incoming light overestimates the reflected light at high phase angles. For example, if the planet is perfectly in between the star and observer, a phase angle of $180°$, assuming parallel incoming light gives a scattering angle of $0°$ over

the entire ring. Looking at Fig. A.2 it becomes clear that this should not be the case. In fact, no ring spangle can even have a scattering angle of $0°$ because the planet is located at the center.

Table A.1: Relative changes in the flux when using the simple or complex solution to the parallel light problem.

Method	Percentage	Percentage decrease
Simple (olivine)	99.934%	0.061%
Complex (olivine)	97.912%	2.088%
Simple (spherical)	98.966%	1.034%
Complex (spherical)	73.873%	26.127%

The difference in flux also changes quite drastically when different particle types are used. It does not alter the relative behavior of the two solutions but changes the impact of the error that is introduced when parallel incoming light is assumed. This is easily explained by looking at Fig. A.3 which shows the single scattering behavior of the olivine particles, perfect spheres with a radii of 20 μm and 40 μm, and molecules as reference. The larger particles have a higher forward scattering peak which makes them more sensitive to small changes in the scattering angle in that region. Both solutions change the illumination angle which in the test case is equivalent to the scattering angle because the viewing angle is $0°$. This also means that when modeling a transit it is extra important to check the validity of the assumption of parallel incoming light.

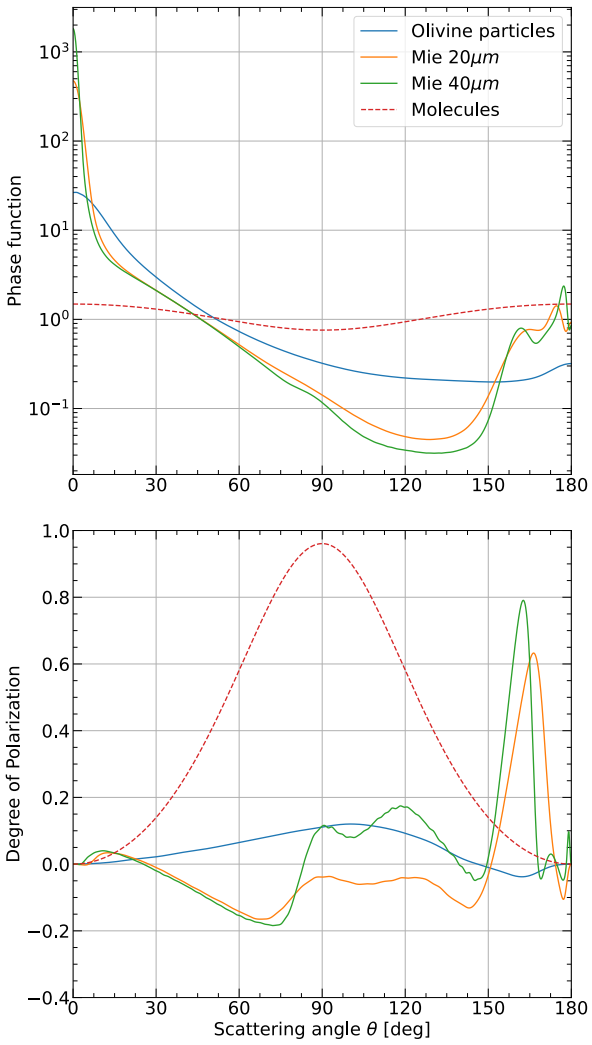

Figure A.3: The flux (top) and degree of polarization (bottom) of incident unpolarized light that has been singly scattered by the gas molecules, the irregularly shaped ring particles [94, 98], and perfect spheres with radii of 20μm and 40μm as functions of the single scattering angle. Similar to the single scattering figure in the paper.

What is a bit unexpected is that the difference between the two solutions is this large. It might be a problem with the implementation of the more complex solution since the limb-darkening effect is not taken into account. This should, however, have been compensated by the fact that all methods use the same amount of samples so the incoming intensity should be the same. To verify if these decreases are in fact because the solution is improved a good test is to increase the semi-major axis and check if the results of the three methods converge. Setting the semi-major axis to 1 AU and using spherical particles decreases the differences to 0.005% and 0.170% for the simple and complex solutions respectively. This suggests that both solutions will in fact increase the accuracy but the more complex solution is significantly better at it. Unfortunately, the more complex solution would take too much time to implement at this stage in the thesis, it is therefore left as a firm recommendation for a follow-up study.

Another test was performed to check the differences (only with the simple solution) during an actual transit. Using a similar orbit as in the previous test, not exactly the same but it is the difference that is important, with the same size ring placed almost face-on with an inclination of $10°$ and $\lambda_r = 0$. The ring

has an optical thickness of 2 and is made up of perfect spheres that have a single scattering albedo of 0.3 and a refractive index of 1.5. Figure A.4 shows both the total flux of the reflected light in parts per million (ppm) as well as the difference that using the simple solution causes. At a true anomaly of 0° the percentage difference is 2.24% so a slight increase over the numbers given in Table A.1. This is to be expected because the errors compound, scaling with the radial distance a spangle has to the center of the planet.

All in all, the improvement of the simple solution is not drastic but is measurable and as it is still an improvement it will be used for the remainder of this study. Knowing that a better solution exists and that it would likely give a lower forward scattering peak, the results that will be presented should be considered as an upper limit.

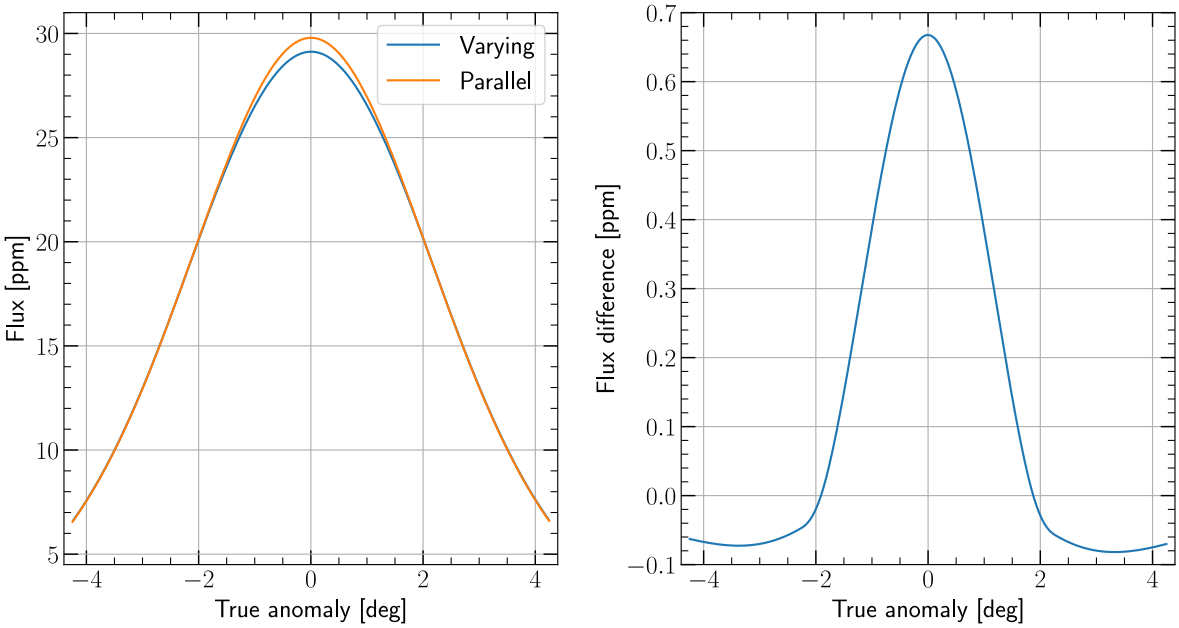

Figure A.4: The forward scattering during a transit modeled for a system similar to AU Mic with a ring that has a 10° inclination. The left image shows both the total flux when using parallel incoming light and with the simple solution, labeled as Varying. The right image is the difference between them. Between roughly $\nu = -2.5^\circ$ and $\nu = 2.5^\circ$ the planet and ring move in front of the star.

A.1.3. Fit parameters

With the changes to the code explained, the fitting method and parameters can be described. As mentioned in the introduction to this study, the fitting method will be kept simple because of time constraints. To fit the model to the data, 12 parameters that describe the system were given as input to the `differential_evolution` optimizer that is part of the `SciPy` python package. The settings of the optimizer that were used to find the results that are presented in Sect. A.1.4 are given in Table A.2. A detailed explanation of each setting can be found in the documentation of the function[a]. To assess the fitness of each combination of parameters the root-mean-square error (RMSE) the resulting model has with the data was used. The 12 parameters that were used are shown in Table A.3. Any parameter that is not associated with the ring has its interval range defined as the 68% credibility interval from the fit done by Plavchan et al. [104]. The radius of the star was not included in the fit because it was determined via a different, independent, method [104]. The particles

Table A.2: Values for the different settings of the optimizer that were used. Any setting that is not mentioned in the list above uses its default value.

Setting	Value
Popsize	56
Updating	deferred
Mutation	(0.1,1.5)
Recombination	0.4
Workers	14
Seed	4
Integrality	active

[a] https://docs.scipy.org/doc/scipy/reference/generated/scipy.optimize.differential_evolution.html#scipy.optimize.differential_evolution

are perfectly spherical particles and are modeled using Mie-scattering, no irregular particles that had measurements of their scattering properties done at 4.5 μm could be found. This is not a big problem, however, because the forward scattering behavior is dominated by the size of the particle. Figure A.3 sort of confirms as the shape of the curve is quite similar up until a scattering angle of $80°$. For that reason, the olivine particles were also included even though the measurements were performed at 633 nm. At 633 nm they have a size parameter of approximately 10 which translates to a r_{eff} of 7.1 μm at a wavelength of 4.5 μm. For every optical thickness, a different Fourier-coefficient file needs to be generated so they are handled as discrete steps by the optimizer, the same applies to the particle radius. The transit is assumed to happen at the apocenter of the orbit because preliminary testing showed problems with reaching the transit duration otherwise. This might be a false assumption, however, so a follow-up study should check if changing this affects the results significantly. Lastly, the transit is modeled at 200 points which are then linearly interpolated to generate the root-mean-square error.

Table A.3: The range of values for the 12 parameters that were used to fit the transit. Where applicable the range is the 68% credibility interval from the fit done by Plavchan et al. [104].

Parameter	Value range
Impact parameter b	[0.05, 0.3]
Ring inclination γ	[1°, 89°]
Ring inclination longitude λ_r	[−89°, 89°]
Planet radius R_p	[0.357, 0.393] $R_{Jupiter}$
Semi-major axis a	[0.06, 0.073] AU
Eccentricity e	[0.01, 0.27]
Inner ring radius r_{in}	[1.2, 2] R_p
Outer ring radius r_{out}	[2.01, 4] R_p
Linear limb-darkening coef. c_1	[0.05, 0.39]
Quadratic limb-darkening coef. c_2	[0.0, 0.42]
Optical thickness τ	[0.0, 0.002, 0.01, 0.05, 0.1, 0.2, 0.6, 1.0, 1.2, 1.6, 2.0, 4.0, 8.0]
Particle radius r_{eff}	[7.1 μm, 20 μm, 40 μm]

A.1.4. Fit results, summary and discussion

The fitting took roughly 12 hours to complete and the optimizer went through 14,109 different configurations to end up with a set of parameters that had a RMSE of 0.0004976. The fitting parameters of the best fit as well as the mean value of the best 10 fits are displayed in Table A.4. These values show that, while the fit prefers a system with a ring, it is optically very thin.
All the top configurations have the lowest possible optical thickness without going to zero, which was possible in the parameter space. It seems that the ring is only there to increase the transit duration and slightly smooth the ingress and egress. This conclusion is based on a couple of observations of the standard deviation of some of the average parameters. The parameters with low variation are the radius of the planet, the semi-major axis, the eccentricity, the size of the ring, the limb-darkening coefficients, and the optical thickness. Most of these relate to the orbit of the planet which therefore seems to have converged. It is interesting to note that due to the close proximity to the star, the impact parameter b has only a limited effect on the duration of the orbit and therefore has a larger variation.

The other thing that seems to have converged is the presence of a ring which is evident from the optical thickness and the stable size of the ring. As long as the ring does not have a highly inclined orientation, the transit depth and duration of a ring are mostly defined by the size of the ring. This leaves the orientation of the ring partially unconstrained, as long as γ and λ_r do not become too large the timing of the transit is not affected much. Lastly, with the low optical thickness the make-up of the ring becomes completely unconstrained since the forward scattering will not produce any significant flux.

The transit curves of the top ten fits are displayed in Fig. A.5, it shows that all the 10 curves fit the

Table A.4: Parameters of the best fitting solution and the average of the 10 best fitting solutions together with their standard deviation.

Parameter	Value best fit	Average over 10 best
b	0.084	0.09 ± 0.01
γ	14.25°	$25° \pm 21°$
λ_r	13.47°	$14° \pm 14°$
R_p	0.367 $R_{Jupiter}$	0.3667 ± 0.0006 $R_{Jupiter}$
a	0.071 AU	0.0714 ± 0.0002 AU
e	0.255	0.258 ± 0.005
r_{in}	1.87 R_p	1.82 ± 0.07 R_p
r_{out}	2.48 R_p	2.49 ± 0.08 R_p
c_1	0.11	0.114 ± 0.004
c_2	0.23	0.23 ± 0.01
τ	0.002	0.002 ± 0.0
r_{eff}	40 μm	All three occur

data quite well and, again, that the influence of the ring is very small. In the middle plot, the transit depth caused by the ring alone is displayed for each solution. The depth is a function of the ring size, orientation, and optical thickness. Since the optical thickness and size is roughly constant, these lines show the effect that the orientation of the ring has. The light that is blocked by the ring during the transit is roughly a factor of 100 smaller than that of the planet.

In the right plot, the forward scattering flux due to the different ring configurations is shown. There are relatively large differences between the solutions due to the different particle sizes and ring orientations. Because the flux is so small, however, these variations do not influence the quality of the fit and the particle size is unconstrained. The lines on the bottom are from rings that contain the olivine particles which have a smaller radius and, therefore, scatter less light in the forward direction. The forward scattering flux of the ring is roughly a factor of 50 smaller than the transit depth of the ring and so both effects are way too small to be reliably detected given the stellar activity. This is also confirmed by the error in the observation data that is presented in Fig A.6.

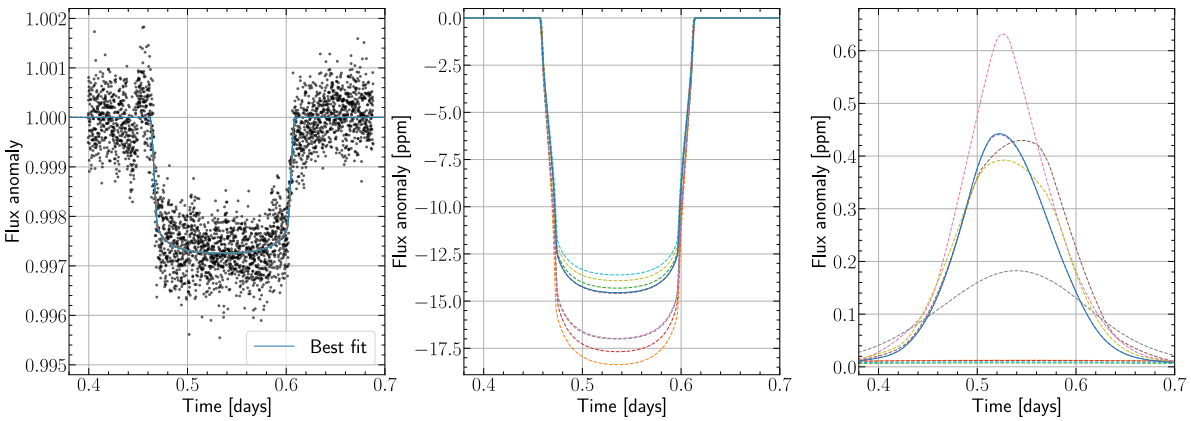

Figure A.5: This figure shows the 10 best-fitting curves to the data, the best fit has been plotted with a solid line. The left image shows the generated transit curves plotted on top of the data. In the middle image, the transit depth of the ring is shown, note the switch to ppm in the y-axis scale. The right image shows the forward scattering flux of the ring, again in ppm, the lines on the bottom are from rings that contain the olivine particles.

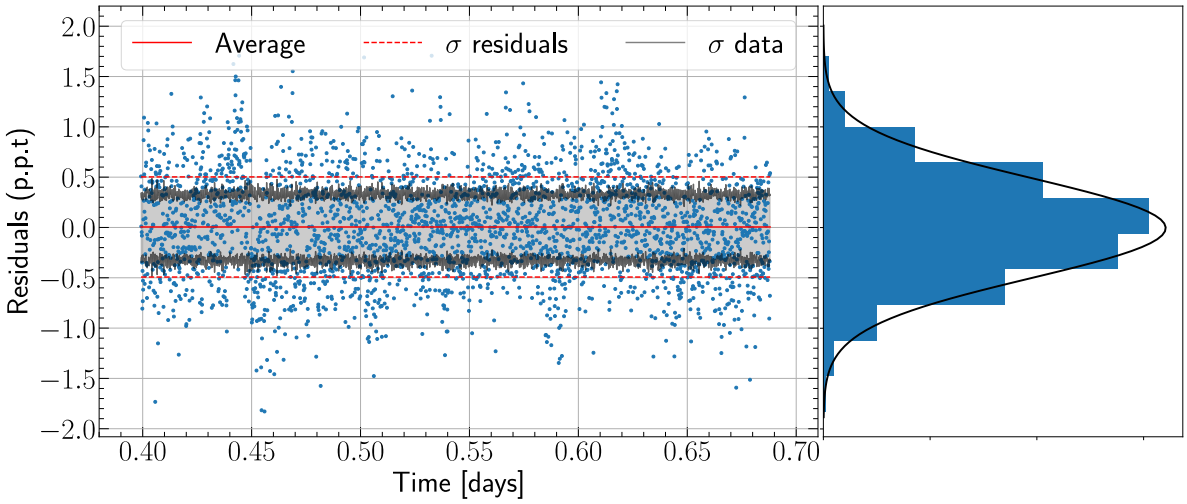

Figure A.6: The residuals (blue dots) of the transit fit, the average value of the residuals (red solid line), the standard deviation of the residuals (red dashed lines), and the standard error of the detrended data points (black line and area) with values in parts per thousand (p.p.t). The distribution of the residuals is displayed in the histogram on the right together with a fitted normal distribution.

Since the 10 transit curves are so similar, only the residuals of the best fit will be shown in Fig. A.6. The features in the data such as the peak at the ingress of the transit as well as a slight downward slope at the end of, and just after, the transit are clearly visible in the residuals. The model is thus unable to generate these features and that results in a worse fit. The average value of the residuals is $5 \times 10^{-6} \pm 5 \times 10^{-4}$ so there is no large-scale systematic error but the standard deviation is indeed higher than the error of the data points, which are the black lines in Fig. A.6.

The conclusion that was previously drawn about how the ring is only there to increase the transit duration and slightly smooth the ingress and egress also has some problems. If the first part of that conclusion were the case the semi-major axis or eccentricity could also increase but both parameters seem to be fixed for the 10 best solutions. Given the nature of the genetic optimizer, it is possible that a local minimum was found in which the orbital elements stay constant but the ring size is optimized. The second part of the conclusion also has some problems because of the large difference in transit depth between the planet and the ring. At ingress or egress, only half of the ring is in front of the star, a depth of roughly 7.5 ppm, which is much smaller than the error on the data points or residuals.

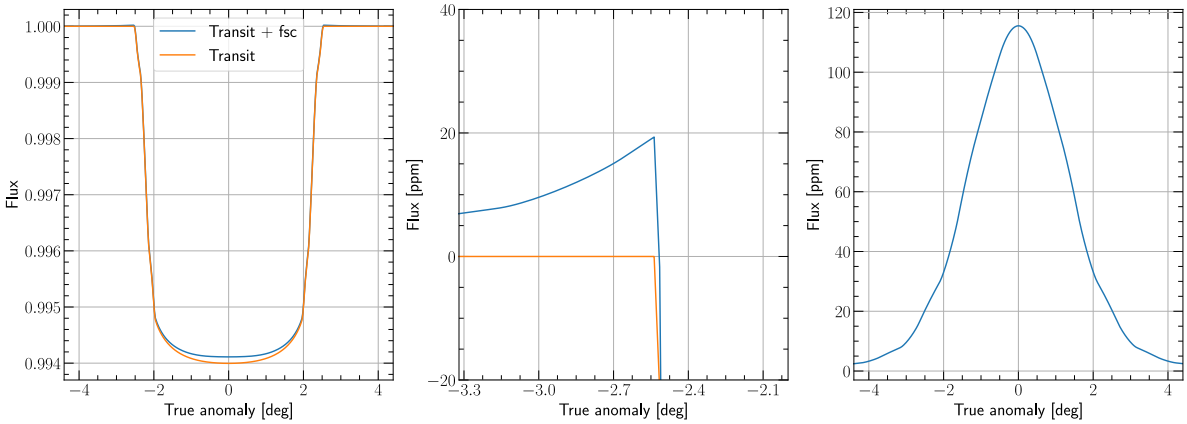

Figure A.7: Transit and forward scattering curves of a best-case scenario in terms of the largest forward scattering peak. The left two figures show the transit with and without forward scattering and a close-up of the ingress. The right figure only shows the forward scattering peak. Orbital parameters are based on the best fit.

Another problem is with the model itself. As has already been mentioned, the ”simple” solution has poor performance compared to the ”complex” solution, in solving the parallel incoming light problem. Tests showed that the ”complex” solution decreased the flux by up to 26% compared to the 1% of the ”simple” solution. Whether this outcome is correct and the decrease constitutes an improvement is still

a bit unclear and would need to be investigated further. Considering the low forward scattering fluxes obtained in the fit, a 26% decrease would not affect the results at all. If implementing the ”complex” solution affects the forward scattering flux in the same way as the ”simple” method does, Fig. A.4 suggests that the peak would get smeared out even more. This could then perhaps explain the egress part of the light curve but not the ingress peak. That initial peak is already hard to explain as a result of forward scattering because of the sharp drop beforehand, no similar peak at egress, and the apparent increase of flux of around 5×10^{-4}. To illustrate the latter a ring with an optical thickness of 0.6, that has a face-on orientation, and is populated with 40 μm particles is simulated. This is a best-case scenario for the forward scattering peak and the results are shown in Fig. A.7. The transit depth is significantly deeper due to the large and optically thicker ring, but the forward scattering peak at ingress and egress is only 20 ppm. After the peak at ingress, the drop-off is also slow and gradual, unlike the observation data. The forward scattering peak has become quite significant which even makes the transit light curve shallower. It thus seems that the peak at the ingress cannot be caused by a ring, and while there are definitely some problems with the model, none seem big enough to disprove this.

A final problem that will be brought up has to do with the fitting method. Not performing a second fit for a planet without a ring has probably been a mistake. The existence of a ring affects almost all other parameters which can make it hard for the optimizer to explore the whole parameter space. It also makes it hard to compare whether a ring improves the fit quality or not. There has also not been any rigorous local optimization besides the one that the `differential_evolution` function performs at the end. The addition of a test fit to see the likely range of parameters could also have helped with the convergence. Especially the range of values for the optical thickness of the ring could have been greatly reduced.

Besides the problems that are mentioned above, the fact that the fit, as it is done here, is unable to generate a light curve with these features could just be because there is no ring. It is very plausible that the weird features in the data are due to stellar activity that has not been filtered out correctly by the detrending. To be sure about this though a follow-up study should explore the ”complex” solution in more detail and do a more thorough fit of the data, including a ring-less planet fit. Another point of improvement could be to look at the detrending again.